

UNIVERSIDAD
NACIONAL
DE COLOMBIA

A STUDY OF PHOTOSPHERIC VECTOR MAGNETIC FIELD CHANGES DURING SOLAR FLARES

Juan Sebastián Castellanos Durán

Universidad Nacional de Colombia
Observatorio Astronómico Nacional
Facultad de Ciencias
Bogotá, Colombia
2016

A STUDY OF PHOTOSPHERIC VECTOR MAGNETIC FIELD CHANGES DURING SOLAR FLARES

Juan Sebastián Castellanos Durán

Tesis o trabajo de grado presentado como requisito parcial para optar al título de:
Magister en Ciencias Astronomía

Directores:

Ph.D. Lucia Kleint

Fachhochschule Nordwestschweiz, Suiza

Prof. Benjamín Calvo-Mozo

Observatorio Astronómico Nacional, Colombia

Línea de Investigación:

Astrofísica Solar

Grupo de Investigación:

Group of Solar Astrophysics (GoSA)

Universidad Nacional de Colombia
Observatorio Astronómico Nacional

Facultad de Ciencias

Bogotá, Colombia

2016

Thesis committee

Referees

Dr. Andrés Asensio Ramos
Instituto de Astrofísica de Canarias
Universidad de La Laguna
La Laguna, Tenerife, Spain

Dr. Mark C. M. Cheung
Lockheed Martin Solar & Astrophysics Laboratory
Palo Alto, California, USA

Chair of thesis defense session

Dr. Santiago Vargas Domínguez
Observatorio Astronómico Nacional
Universidad Nacional de Colombia
Bogotá, Colombia

The defense took place on October 12, 2016, at the
Universidad de Cartagena, Cartagena, Colombia.

A mi madre y padre

Acknowledgments

I would like to acknowledge many people and institutions that contributed to this thesis. First of all, I would like to express my sincere gratitude to my advisors Dr. Lucia Kleint and Prof. Benjamín Calvo-Mozo. They continuously supported me in all aspects. Their guidance, patience, and motivation kept me on track. I learned unimaginable physical phenomena from their immense knowledge, and thanks to their advice, I have made a huge step in my scientific career. The seed they planted will stay with me my whole life.

This work was funded by the grant *Jóvenes Investigadores 2014*, convocatoria 645 - COLCIENCIAS, Colombia. Fundación para la Promoción de la Investigación y la Tecnología – Banco de la República and Dirección Nacional de Investigación y Extensión – Universidad Nacional de Colombia funded the travel grants to participate in an international meeting in Granda, Spain 2015. The University of Applied Sciences and Arts Northwestern Switzerland hosted me for a collaborative visit that was very beneficial to the thesis.

I would like to thank some of those that were important during this project. In particular, my sincere thanks goes to: Islena Bonilla, Prof. Säm Krucker, Prof. André Csillaghy, Prof. Santiago Vargas, Dr. Andrés Asensio, Dr. Mark Cheung, Dr. Marina Battaglia, Matej Kuhar, Prof. Juan Manuel Tejeiro, Lisa Grassato, Marilena Naoum, Diana García, Nataly Mateus, Diana Rendon, Marianne Egloff, Julian Alvarado, Eliana Amazo, Alejandra Ramirez, Alejandro Cardenas, and all guys of the Group of Solar Astrophysics (GoSA). Also, I thank Alvaro Castellanos that helped me with part of the English corrections of the manuscript.

Last but not the least, I would like to thank my family, especially my mother and father. They supported me in all senses. When I had problems, they did not let me fall. They encouraged me when I needed it, and they helped me in all possible ways.

Abstract

Large amounts of energy are released when magnetic field lines reconnect in the corona during solar flares. Observations have found both transient and irreversible changes in the photospheric magnetic fields during flares, but their origins and mechanisms are yet unclear. To investigate the properties of magnetic field changes during flares, e.g. their size, area, and timing, we performed a statistical analysis of 75 solar flares. We analyzed the line-of-sight (LOS) and vector magnetic field measurements obtained by the Solar Dynamics Observatory. We derived the locations of permanent magnetic field changes of these flares that were selected based on a wide energy range from small to extreme flares (18 X-class, 37 M-class, 19 C-class and 1 B-class flares), and a wide range of heliographic longitudes (disk center to limb). We identified kernels of permanent magnetic field changes in 80% of the flares. 36 events showed more positive changes, while during 23 flares more negative irreversible variations were observed. We found two decreasing exponential relations for: (i) the observed step-size values, (ii) the number of the permanent changes found with respect to the distance measured from the polarity inversion line (PIL). An enhancement in white-light (WL) emission was observed in 74% of the events. The WL emission and the permanent changes do not have a one-to-one spatial relationship, but they are near each other and often overlap. The energy emitted during each event in the soft X-ray band correlates with the total photospheric area where permanent changes are located following a power-law.

We also studied the evolution of the three components of the magnetic field in the same places where permanent changes in the LOS component were found, as well as a region of few arcsecs width measured from the PIL. We concluded that the flares that show irreversible changes in azimuth and inclination do not vary with the location of the flare, although the correlation with the field strength decreases for flares that were located near the limb. Permanent changes in the field strength, and inclination are found more often than changes in azimuth with $\sim 19\%$ difference. The strength field irreversibly increased near the PIL in 29 flares. We observed that the field becomes tilted after 20 flares. This agrees with the implosion model (Hudson 2000) that predicts the field becoming more horizontal after the flare. However, during 13 flares, the radial field showed positive and larger changes than the horizontal field. This implies another scenario when the flare-loop is untwisted after flares (Kleint 2016).

Keywords: The Sun, Solar flares, Photospheric Magnetic fields.

Resumen

Grandes cantidades de energía se liberan cuando se vuelven las líneas de campo magnético se re-conectan en la corona durante fulguraciones solares. Observaciones se han encontrado cambios transitorios e irreversibles en los campos magnéticos fotosféricos durante fulguraciones, pero sus orígenes y mecanismos son desconocidos. Investigamos las propiedades de los cambios de campo magnético durante 75 fulguraciones, por ejemplo, su tamaño, área y tiempo. Analizamos la componente en la línea de la visual (LOS) y mediciones de campo magnético vectoriales obtenidas por el Solar Dynamics Observatory. Las fulguraciones fueron seleccionados sobre la base de una amplia gama de energía desde fulguraciones pequeñas hasta extremas (18 clase X, 19 clase M, 37 clase C y 1 clase B), y una amplia gama de longitudes heliográficas (desde el centro del disco al limbo). Se identificaron núcleos de cambios en el campo magnético permanente en el 80% de los fulguraciones. 36 eventos mostraron más cambios positivos, mientras que durante 23 fulguraciones se observaron más cambios negativos. Se encontraron dos relaciones exponenciales decrecientes para: (i) los tamaños de los cambios observados, (ii) el número de los cambios permanentes que se encuentran con respecto a la distancia medida desde la línea de inversión de polaridad (PIL). Se observó un aumento en la emisión de luz blanca (WL) en el 74% de los eventos. La emisión WL y los cambios permanentes no tienen una relación espacial de uno a uno, pero están cerca unos de otros, y a menudo se superponen. La energía emitida durante cada evento en la banda de rayos X blandos se correlaciona con el área total de fotosférica donde se encuentran los cambios permanentes siguiendo una ley de potencias.

También se estudió la evolución de las tres componentes del campo magnético en los mismos lugares donde se encontraron cambios permanentes en el componente de LOS, así como en una región de unos pocos segundos de arco de ancho medido desde la PIL. Las fulguraciones que muestran cambios irreversibles en azimut e inclinación no varían con la ubicación de la llamarada, aunque la correlación con la intensidad del campo disminuye en fulguraciones que se encontraban cerca al limbo. Los cambios permanentes en la intensidad de campo, y la inclinación se encuentran con más frecuencia que los cambios en azimut con $\sim 19\%$ de diferencia. La intensidad de campo aumenta de forma irreversible cerca de la PIL en 29 fulguraciones. Observamos que el campo se inclinó después de 20 fulguraciones. Esto está de acuerdo con el modelo de implosión (Hudson 2000) que predice que el campo es cada vez más horizontal después de la llamarada. Sin embargo, durante 13 fulguraciones, el campo radial mostró cambios positivos y mayores que el campo horizontal. Esto implica otro escenario cuando los bucles de la fulguraciones pierden su torsión después de la fulguración Kleint (2016).

Palabras clave: El Sol, Fulguraciones solares, campos magnéticos fotosféricos.

Contents

Acknowledgments	VII
Abstract	VIII
Resumen	IX
Figures	XI
Tables	XIII
Abbreviation	XIV
1 The Sun	1
2 Solar Flares	7
2.1 Irreversible Changes of the Magnetic Field During Flares	11
3 Magnetic Fields on the Sun: Theory and Techniques	17
3.1 Polarization of Electromagnetic Waves	17
3.2 Stokes Parameters	20
3.3 Zeeman Effect	22
3.4 Deriving the Solar Magnetic Field	23
3.4.1 Full Magnetic Field Vector: Inversion Techniques	23
3.4.2 Line-of-Sight Component	25
3.5 Lorentz Force	26
4 Data, Sample, and Methodology	27
4.1 The Solar Dynamics Observatory	27
4.2 Flare Sample	29
4.3 Methodology: <i>Pipeline</i>	33
4.3.1 The Data	33
4.3.2 Time Range	34
4.3.3 Coordinates: Field of View	35
4.3.4 Alignment	36
4.3.5 Fitting Procedure	37
4.3.6 Limits of Fitting Parameters	38
4.3.7 Size of the Step	38
4.3.8 Conditions	40

5 Permanent Changes in the Line-of-Sight Component of the Magnetic Field	45
5.1 Evolution of the Active Region	46
5.2 Morphology of the Changes	48
5.3 Location of the Permanent Changes	51
5.4 Relation between the PIL and Permanent Changes	57
5.5 White-Light Emission and Permanent Changes	59
5.6 Lorentz force in the LOS Component	61
5.7 Statistics of Permanent Magnetic Field Changes	62
6 Vector Magnetic Field Analysis	69
6.1 Vector Magnetic Field Quantities	69
6.2 Co-spatiality between ΔB_{LOS} and Vector Magnetic field changes	72
6.3 Vector Magnetic Field Changes along the PIL [*]	81
7 Summary, Conclusions and Outlook	87
7.1 Outlook	90
Bibliography	93

Figures

1.1 Solar structure	1
1.2 Solar photosphere	2
1.3 Solar granulation	2
1.4 The magnetic field in sunspots	2
1.5 High-resolution H α image of the chromosphere	3
1.6 Full disk H α image of the chromosphere	3
1.7 Spicules	3
1.8 IRIS full-disk mosaic image in the Mg II k line	4
1.9 Transition region during an X-flare observed by IRIS	4
1.10 Corona composite image	5
1.11 Coronal mass ejection	5
1.12 Solar corona during an eclipse	5
2.1 Solar flares	7
2.2 The big picture of solar flares	8
2.3 Thermal and non-thermal emission during flares observed by RHESSI	9
2.4 GOES light curve	11
2.5 Permanent change of the LOS magnetic field during a flare	12
2.6 Vector magnetic field changes during an X-class flare	14
3.1 Observational Stokes parameters of a small sunspot	21

4.1	The Solar Dynamics Observatory	27
4.2	The six HMI tuning-position profiles in the Fe I solar line	28
4.3	Flare locations above solar disk	29
4.4	Pipeline flow diagram	33
4.5	The magnetic field and continuum emission of the active region AR 11305	34
4.6	Determining the observing time range	36
4.7	Coordinates: choosing a suitable FoV	37
4.8	Geometrical approach to solve the degeneracy between parameters b and n	38
4.9	Degeneracy of the stepwise function	39
4.10	Extreme cases when changes in the Fe I absorption line are observed	41
4.11	Three extreme cases to measure the amplitude change	42
5.1	Abrupt and permanent changes in the LOS component	45
5.2	Evolution of AR 11890 before, during, and after the X1.1 flare	47
5.3	Morphologic classification of permanent changes	48
5.4	Morphologic classification of permanent changes II	49
5.5	Kernel of ΔB_{LOS} during an M1.4 flare	52
5.6	ΔB_{LOS} for the entire sample overplotted on intensity images	53
5.7	ΔB_{LOS} for the entire sample over the magnetogram	54
5.8	The entire sample of kernels of ΔB_{LOS} overplotted on intensity images	55
5.9	The entire sample of kernels of ΔB_{LOS} over magnetogram	56
5.10	PIL and permanent changes	57
5.11	Permanent changes and the distance from the PIL	59
5.12	White-light emission and magnetic field changes	60
5.13	The change of the Lorentz force in the LOS	61
5.14	GOES times and their relation with the permanent changes	62
5.15	Total signed permanent flux change per flare regarding the GOES class	63
5.16	Total flux change in the LOS magnetic field	64
5.17	Area where the magnetic field changed as a function of the GOES class	64
5.18	Number of ΔB_{LOS} as function of the rate of ΔB_{LOS} in units of G minute ⁻¹	65
5.19	Distribution of the changes during C-, M- and X-class flares	66
5.20	Exponential parameters for the entire sample	67
5.21	Exponential distribution of the LOS magnetic field changes	68
6.1	An active region observed by HMI	70
6.2	Comparison between vector and LOS data	71
6.3	Permanent changes of the vector magnetic field	73
6.4	Vector changes where permanent variations in the LOS component were found	74
6.5	Permanent changes of the vector magnetic field and Lorentz force	76
6.6	Permanent vector changes associated with ΔB_{LOS} per flare	77
6.7	Location of permanent vector changes associated with ΔB_{LOS}	78
6.8	Permanent changes associated with ΔB_{LOS} as function of GOES class	79
6.9	Permanent vector changes without ΔB_{LOS}	80
6.10	Location of the area along the PIL [®] in three active regions	82
6.11	Temporal evolution of the vector components around the PIL [®] during an X1.1 flare	84
6.12	Temporal evolution of the vector components around the PIL [®] during an M9.3 flare	85
6.13	Temporal evolution of the vector components around the PIL [®] during an M2.2 flare	86

Tables

2.1	GOES classification	10
4.1	Flare sample description	30
4.1	Flare sample description (continued)	31
4.1	Flare sample description (continued)	32
4.2	Starting values and limits of fitting parameters for the fit procedure	38
4.3	Pipeline conditions	43
6.1	Percentage of the ΔB_{LOS} that showed irreversible vector changes	75
6.2	Sign of vector changes along the PIL [®]	83

Abbreviation

Abbreviation	Expression
ΔB_{LOS}	Permanent changes of the line-of-sight magnetic field
ψ	Azimuth of the magnetic field
γ	Inclination of the magnetic field
\vec{B}	Photospheric magnetic fields
$ \vec{B} $	Strength of the magnetic field
AIA	The Atmospheric Imaging Assembly
CMEs	Coronal Mass Ejections
EVE	The Extreme Ultraviolet Variability Experiment
EUV	Extreme Ultra Violet
FoV	Field of View
FWHM	Full Width at Half Maximum
GOES	The Geostationary Operational Environmental Satellites
GONG	The Global Oscillation Network Group
HMI	The Helioseismic and Magnetic Imager
HXR	Hard X-rays
IRIS	The Interface Region Imaging Spectrograph
LCP	Left Circular Polarization
LOS	Line-of-Sight
LTE	Local Thermodynamic Equilibrium
RCP	Right Circular Polarization
RHESSI	The Reuven Ramaty High Energy Solar Spectroscopic Imager
SDO	The Solar Dynamic Observatory
SHARP	The Spaceweather HMI Active Region Patch
SSWIDL	SolarSoftWare IDL
SXR	Soft X-rays
VFISV	The Very Fast Inversion of the Stokes Vector for the Helioseismic and Magnetic Imager
WL	White-Light
WLFs	White-Light Flares

Chapter 1

The Sun

The Sun and its strong relation with life on Earth has interested cultures around the world for centuries. It has been studied from different perspectives such as its structure, the dynamics of magnetic fields, the Sun-as-star and from the stellar point of view to changeable events in the solar atmosphere and the interaction with the solar system and space weather. The Sun regularly shows very energetic, eruptive and transient events that are known as solar flares and that are still unpredictable. Due to the significant amount of energy and different physical processes involved, these explosions can perturb all layers in the solar atmosphere and the interplanetary space.

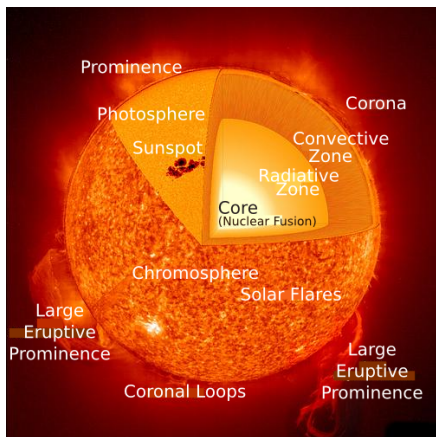


Figure 1.1: Composite image of the solar structure from the core to the corona. The inner layers are core, radiative zone, and convection zone. The solar atmosphere is illustrated by the photosphere, the chromosphere, and the corona. Transient events include solar flares, sunspots, prominences and coronal loops. Image from scitechlab.

The Sun has an effective surface temperature around ~ 5800 K, and it is in hydrodynamic equilibrium. The solar spectrum ranges from high energy γ -rays to radio emission. In the 19th century, the German physicist Joseph von Fraunhofer passed sunlight through a slit and observed some prominent dark lines in the solar spectrum. Forty-five years later astronomers found that these lines are produced in the solar atmosphere, and nowadays they are called the Fraunhofer lines. These absorption lines correspond to different electronic transitions of various elements, for example from Hydrogen, or the Sodium doublet.

The solar interior is divided into layers according to the physical processes that dominate those plasma volumes. The innermost zone is called *the core*. There, the entire energy of the Sun is created when the fusion of four protons produces Helium, energy, and some byproducts mainly through the $p-p$ chain. *The radiative and convection zones* are the layers where the energy from the core is primarily transported by the processes that give these layers their names. The energy travels through these zones until it reaches the solar *surface*.

The photosphere is the visible *surface* of the Sun. The bottom of the photosphere is defined as the layer where the optical depth τ_{5000} at 5000 Å is equal to one, and it extends for few hundred kilometers. The most prominent features observed in the photosphere are sunspots produced by the interaction between the magnetic fields and plasma. The magnetic field lines in this layer are frozen to the plasma, and reach the photosphere from the solar interior (e.g. Ayres et al. 2009, Cheung & Isobe 2014, and references therein). Figure 1.2 shows a full-disk image of the solar photosphere in the continuum near the 6173 Å Fe I line. The image was taken by the SDO satellite on October 24, 2014, when the biggest sunspot in 25 years was transiting the solar disk.

Small ($1''$) cells are ubiquitous on the solar surface and are called *solar granulation* (see figure 1.3). They arise from the solar interior and heat transport by convection. The observed area of granules ranges from a thousand kilometers to one megameter (e.g. Rieutord & Rincon 2010).

Sunspots are darker and cooler magnetic structures on the solar surface. They appear where an intense concentration of magnetic fields from the solar interior cross the photosphere due to magnetic buoyancy. Sunspots are darker because the magnetic field lines inhibit the convection, decreasing the temperature inside those plasma volumes. Sunspots are often characterized by a penumbra and an umbra. Smaller pores may be distinguished from sunspots due to the absence of a penumbra (e.g. Solanki 2003). The magnetic flux and area of sunspots strongly influence their lifetime, which ranges from hours to months (e.g. van Driel-Gesztelyi & Green 2015). The typical values of the field strength in the umbra range between 2000–3000 G, and the field decreases its strength in the penumbra to 700–1000 G (Solanki 2003). The magnetic field lines in sunspots are more vertical in the umbra compared to those located in the penumbra, which are tilted with respect to the surface. Figure 1.4 illustrates a continuum image of the active region AR 10953 and its magnetic structure.

Sunspots may form from several dipoles emerging from the solar interior at different latitudes, creating complex magnetic structures. The Sun has an 11-year cycle, during which the number and the location of sunspots, as well as the number of explosive events changes. The maximum latitudes of sunspots are ± 40 degrees at the beginning of the cycle. In the course of the ~ 11 years, sunspots appear at lower latitudes, finishing the cycle with sunspots developing near the equator, a phenomenon known as the *butterfly diagram* (e.g. Hathaway 2015).

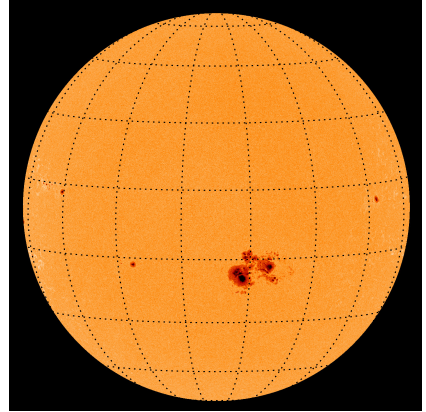


Figure 1.2: Full disk solar photosphere. The Image was taken in the continuum near the 6173 Å Fe I line by the Solar Dynamics Observatory on October 24, 2014.

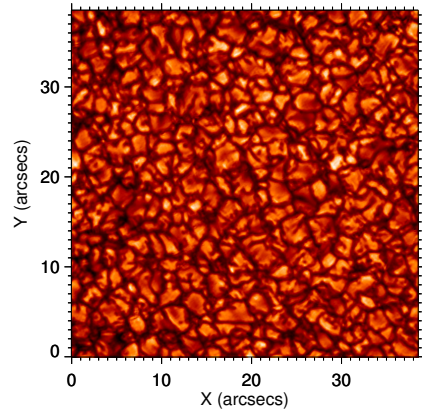


Figure 1.3: Solar granulation taken by IMaX spectropolarimeter onboard the Sunrise balloon in June 9, 2009.

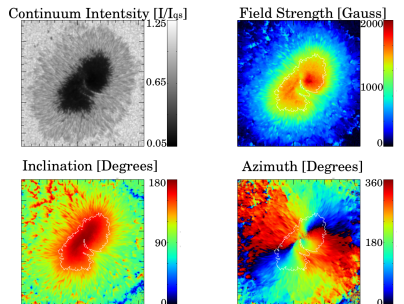


Figure 1.4: The magnetic field vector in the sunspot AR 10923, November 14, 2006. The upper panels show the continuum intensity near 6300 Å (left) and the field strength (right). The lower panels display the inclination on the line-of-sight from the observer's point-of-view (left), and the azimuth in the plane parallel to the surface (right). The field of view of the image is $100'' \times 100''$. Figure adapted from Borrero & Ichimoto (2011).

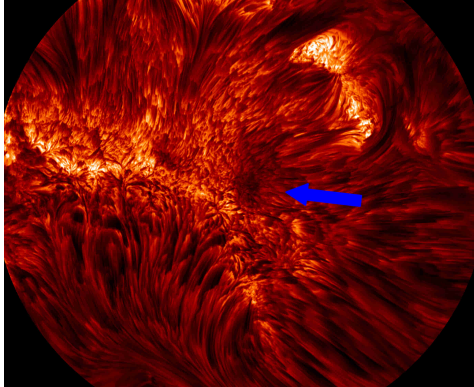


Figure 1.5: H α image of the solar chromosphere with high-resolution of 0.04''. Image was taken on May 22, 2013, by the New Solar Telescope at Big Bear Solar Observatory.

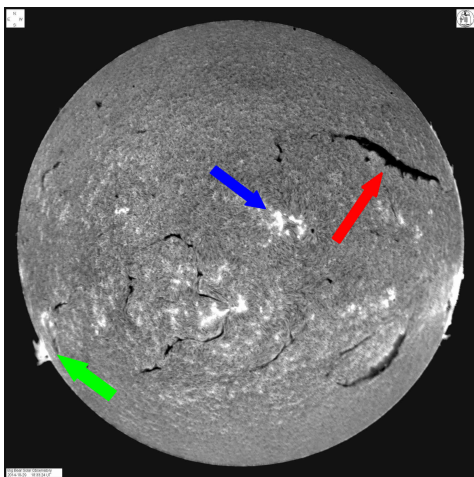


Figure 1.6: Full disk H α image was taken at the Big Bear Solar Observatory during October 29, 2014.

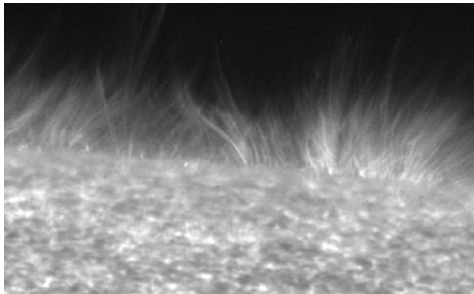


Figure 1.7: Spicules above the solar limb observed by the Hinode satellite in the Ca II H line. The image covers an area of $\sim 15 \times 40$ Mm. Image adapted from Judge & Carlsson (2010).

The chromosphere is the layer above the photosphere. This dynamic zone is out of local thermodynamic and radiative equilibrium (e.g. Linsky & Avrett 1970). Different lines are formed at chromospheric altitudes, such as H α with wavelength 6563 Å and the calcium H and K lines at 3968 Å and 3933 Å, respectively.

The chromosphere is an inhomogeneous and variable layer, which changes on different time scales from few seconds to hours or even days (e.g. Hall 2008, Vernazza et al. 1981). Hall (2008) defines the chromosphere as the zone where

“(a) we observe emission in excess of that expected in radiative equilibrium and (b) where cooling occurs mainly by radiation in strong resonance lines (rather than in the continuum as is mostly the case in the photosphere) of abundant species such as Mg II and Ca II”.

Figure 1.5 is a high-resolution image of the chromosphere, where fibril structures are close to an emerging sunspot (marked by blue arrow). Dark fibrils are regions of cold gas volumes compared to their surroundings (e.g. Solanki et al. 1994).

Filaments or *prominences* are chromospheric and coronal structures that are evidence of the presence of magnetic fields. Filaments are observed on-disk and prominences off-limb, but both are the same phenomenon. Some of them have lengths similar to the solar radius. Prominences are dark at the coronal level, and observations suggest that prominences consist of volumes of dense, cold chromospheric plasma located at coronal heights, and in some cases, they may erupt (e.g. Parenti 2014). Bright regions observed in the chromosphere and near sunspots are called *plages*. They are small areas of hot plasma compared to their surroundings due to the presence of magnetic fields (e.g. van Driel-Gesztelyi & Green 2015). Figure 1.6 shows a H α full disk image of the solar chromosphere, where black structures over the solar disk (e.g. red arrow) and white features above the limb (e.g. green arrow) are filaments and prominences, respectively. The bright regions on the disk are plages (e.g. blue arrow).

Spicules are chromospheric features observed above the solar limb (see figure 1.7). These jetlike structures in the solar atmosphere move preferentially upward and their lifetime ranges from a few seconds to minutes (e.g. Tian et al. 2014, de Pontieu et al. 2007).

The transition region is a complex interface region between the solar surface and the corona. It has a thickness of a few hundred kilometers. In this region, huge temperature gradients exist ranging from $\sim 10^3$ K (in the chromosphere) to $\sim 10^6$ K (in the corona), while the density decreases by two orders of magnitude in the same narrow layer. The temperature of the transition region varies from twenty thousand to eighty thousand Kelvin (e.g. Mariska 1992). Figure 1.8 shows a full-disk mosaic image of the transition region in the Mg II k line. The combined images were taken by the Interface Region Imaging Spectrograph (IRIS, De Pontieu et al. 2014), which is currently the newest solar spacecraft and was designed to study the transition region.

Jets are structures with a hair-like morphology, and they appear as bright spots with temperatures around $\sim 10^5$ Kelvin. The mean lifetime of jets ranges from 20 to 80 seconds and they have lengths of three hundred kilometers or greater (e.g. Tian et al. 2014).

The transition region plays a significant role in our understanding of the solar atmosphere. Measurements of the corona suggest temperatures of a few million Kelvin, but it is still unclear which mechanism transports enough energy to heat the corona (see e.g. Testa et al. 2014, De Pontieu et al. 2014, Hudson 2011, and references therein). One of the candidates to explain the so-called *coronal heating problem* are small explosions that release the energy stored in the magnetic field. These eruptions may occur when random motions of the magnetic lines make the field lines reconnect between each other (e.g. Hudson 2011). These explosions, that occur all the time on the Sun, are called nanoflares, which are far less energetic than those flares studied in this work (see chapter 2). According to McIntosh et al. (2011) traveling ions and magnetic field waves (Alfvén waves) may also carry enough energy to heat the corona. Figure 1.9 illustrates an IRIS slit-jaw image of the transition region during an X-class flare on March 29, 2014 (Kleint et al. 2015, 2016).

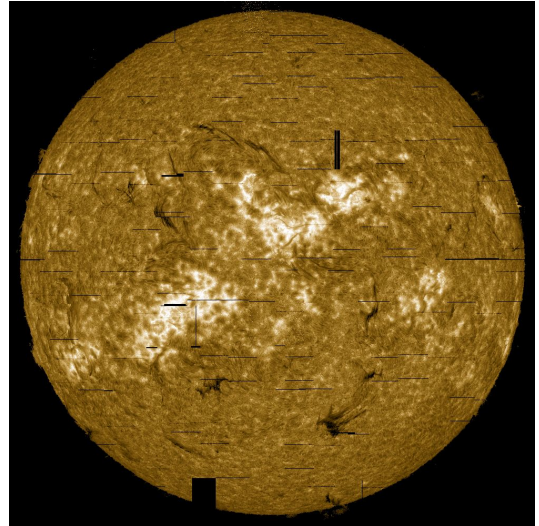


Figure 1.8: IRIS full-disk mosaic image of Mg II k line on May 12, 2014. The IRIS mosaics are a combination of a series of raster taken at different locations of the solar surface to cover the full disk. Image from iris.lmsal.com/mosaic.html.

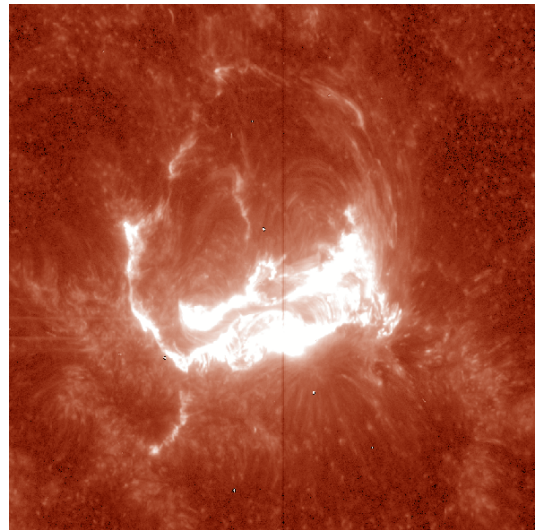


Figure 1.9: IRIS slit-jaw image of the transition region during the X-flare on 2014 March 29 (Kleint et al. 2015, Kleint et al. 2016). The image was taken by the IRIS satellite.

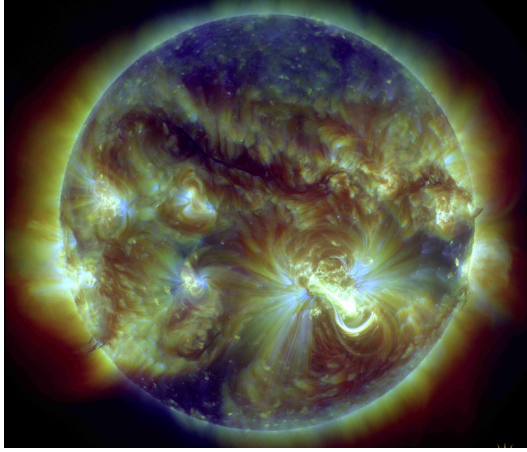


Figure 1.10: Composite image of the three SDO/AIA channels at 171 Å (blue), 193 Å (green), and 211 Å (red). The image was taken on October 24, 2014. Image by the Lockheed Martin Solar and Astrophysics Laboratory (LMSAL).

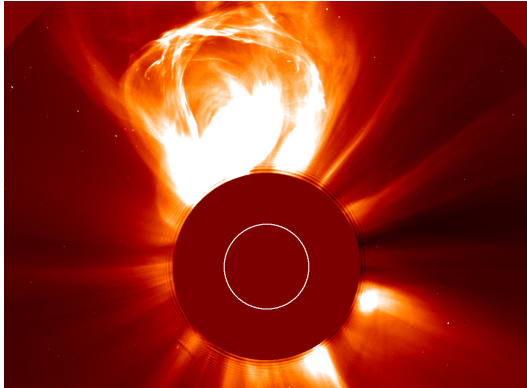


Figure 1.11: Coronal mass ejection recorded by the SOHO satellite. Image from apod.nasa.gov.

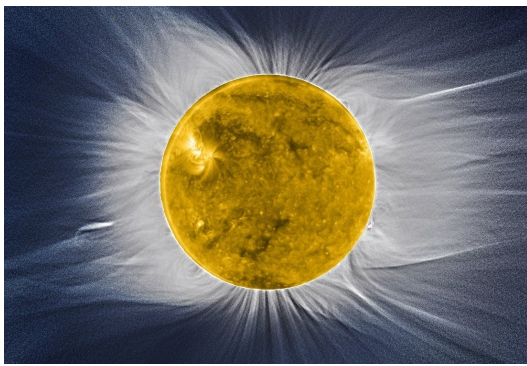


Figure 1.12: Composite image of the solar corona. The yellow-scaled image is a full-disk image taken by the ESA instrument Proba-2 SWAP imager using a filter centered at 174 Å. Simultaneously, the scattered continuum emission from the solar corona (white-scaled image) was captured on the solar eclipse observed from Atoll Hao, in French Polynesia on July 11, 2010. Image is reproduced from Poletto (2015).

The corona is the outer region of the solar atmosphere, where highly ionized lines of heavy elements are observed, and where electron temperatures of millions of Kelvin are measured (e.g. Hall 2008). The corona emits mainly in extreme ultraviolet (EUV), thermal and hard X-rays (HXR). Coronal loops are structures of plasma trapped along the magnetic field lines. These phenomena occur when coronal plasma is frozen to magnetic lines because the magnetic pressure is greater than the thermal pressure. The bulk energy emitted during flares is released in the corona. Solar flares start when coronal field lines reconnect and release energy stored in the magnetic field. Figure 1.10 shows a composite image of the corona during the solar flare on October 24, 2014. The image is made by three EUV coronal channels that respond to different temperatures of the plasma. The blue channel corresponds to the Fe IX emission at 171 Å with a temperature around 0.6 MK. The red channel (211 Å) is related to the transitions of Fe XIV with temperatures ranging $\sim 10^5 - 10^7$ K and the green channel (193 Å) corresponds to Fe XII with a temperature around 2.0 MK.

Other explosive events are observed in the corona and are known as Coronal Mass Ejections (CMEs). CMEs consist of large amounts of coronal plasma that is ejected from the Sun and travels in the interplanetary space. In some cases, a CME reaches the Earth and interacts with the atmosphere, exciting elements in the atmosphere and producing e.g. *aurora borealis*. Figure 1.11 shows a CME observed by the coronagraph onboard the satellite SOHO. Coronagraphs block the solar disk to be able to see the faint light coming from the corona.

During solar eclipses, the northern and southern polar zones have been found to be darker than the equatorial zones (e.g. Aschwanden 2005). Also, some regions on the disk are observed to be less bright than the average on EUV images. These regions are called *coronal holes*, and they are regions where opened lines of the magnetic field are located. Particles are escaping into the interplanetary medium along these opened lines. Coronal holes are regions with temperatures lower than the rest of the corona. Figure 1.12 shows a composite image of the corona taken during a solar eclipse. The white-light structures are the magnetic field lines originating from the solar interior and going into space.

Magnetic fields play a major role in solar dynamics, because many processes are related to them and to their changes. Magnetic fields in the Sun were first observed by Hale (1908) and they are thought to be produced by dynamo processes occurring in the solar interior. They become buoyant due to the magnetic pressure that causes the plasma to expand. Magnetic field lines reach the photosphere, where they interact with the medium creating magnetic structures such as sunspots and coronal loops. The main observational technique to study solar magnetic fields consists of measurements of the polarization states of the sunlight (spectropolarimetry) from spaceborne and ground-based observatories.

There are many open or only partially solved questions in solar physics related to magnetic fields. They range from the interior towards solar atmosphere and the relation with the interplanetary space and the heliosphere. Many of these questions are out of the scope of this work but include the following crucial issues:

Where is the magnetic field produced in the solar interior?

How are magnetic fields transported from the interior to the solar atmosphere?

What is the structure of the magnetic field throughout the solar atmosphere?

What are the dynamics of plasma during the formation of a sunspot?

What are the dynamics and topology of magnetic fields in the chromosphere and transition region?

How is the energy that heats the corona transported and what is the main physical process?

How does the magnetic reconnection work in detail during flares?

How are electrons and ions accelerated during flares?

How can we forecast flares?

What is the interaction between CMEs and the magnetosphere and Earth's atmosphere?

In this thesis, we study the relation between the photospheric magnetic fields and solar flares. We aim to examine how magnetic fields change during flares, and what the implications of these changes are. The first ideas relating the production of flares and magnetic fields originate in the 1930s, but only during the 1960s and 1970s the so-called standard model of solar flares (see §2) was developed. In the 1970s and 1980s, astronomers started to notice some trends in their observations suggesting that changes in photospheric magnetic fields are related to flares. But it was not until the 1990s that the measurements were stable enough and fast enough to start the research on the relation between flares and photospheric magnetic fields. Yet there still remain partially unsolved questions like the following:

Do the magnetic fields become weaker or stronger after flares?

How do the photospheric magnetic fields change their topology due to the eruption process?

Are the permanent changes of magnetic fields related to the emitted energy by the flare?

To answer these questions, we carry out a statistical analysis of solar flares taking advantage of seeing free, 24-hour coverage, high spatial and temporal resolution observations from the Solar Dynamics Observatory.

In chapter 2, solar flares are introduced. In chapter 3, we present the theory behind our study and how we measured the solar magnetic fields. Our methodology, data, sample, and instruments are described in chapter 4. Our results and analysis of this observational work are presented in chapters 5 and 6, and we summarize our conclusions and future implications of our research in chapter 7.

Chapter 2

Solar Flares

Solar *flares* are highly energetic events occurring in the solar atmosphere. They were first observed by Carrington (1859) and Hodgson (1859), and since then, these events have been studied intensively (see review by Benz 2008). It is agreed that magnetic reconnection is the process responsible for achieving the energy necessary to accelerate particles; once accelerated, particles precipitate into the lower solar atmosphere, heating and moving plasma along the way (see review by Hudson 2011). Solar flares perturb the whole solar atmosphere from the photosphere to the interplanetary medium. As an example, figure 2.1 illustrates what the corona looks like during a flare.

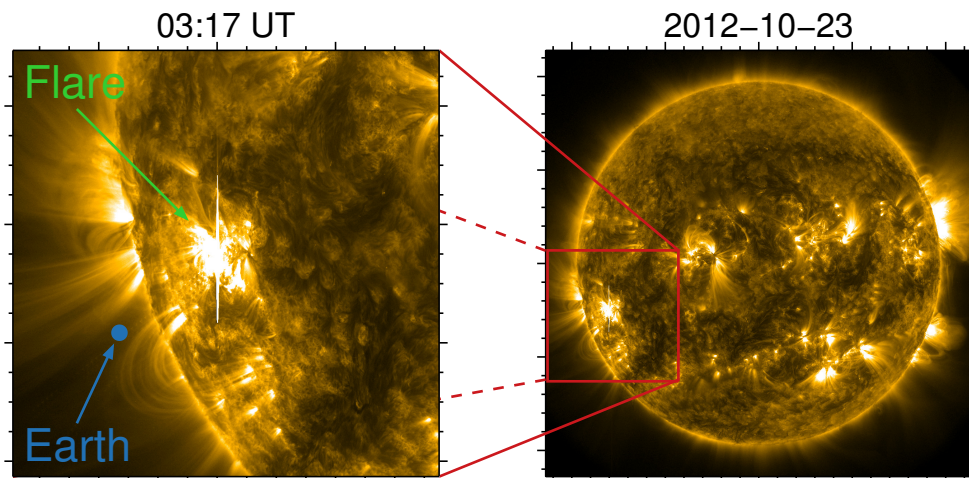


Figure 2.1: The right panel shows a full disk image of the erupting corona observed by the AIA 171 Å channel on October 23 2012 at 03:17 UT. The left panel shows a zoom in of the south-east while a solar flare is occurring (green arrow). The rough size of the Earth is drawn by the blue circle.

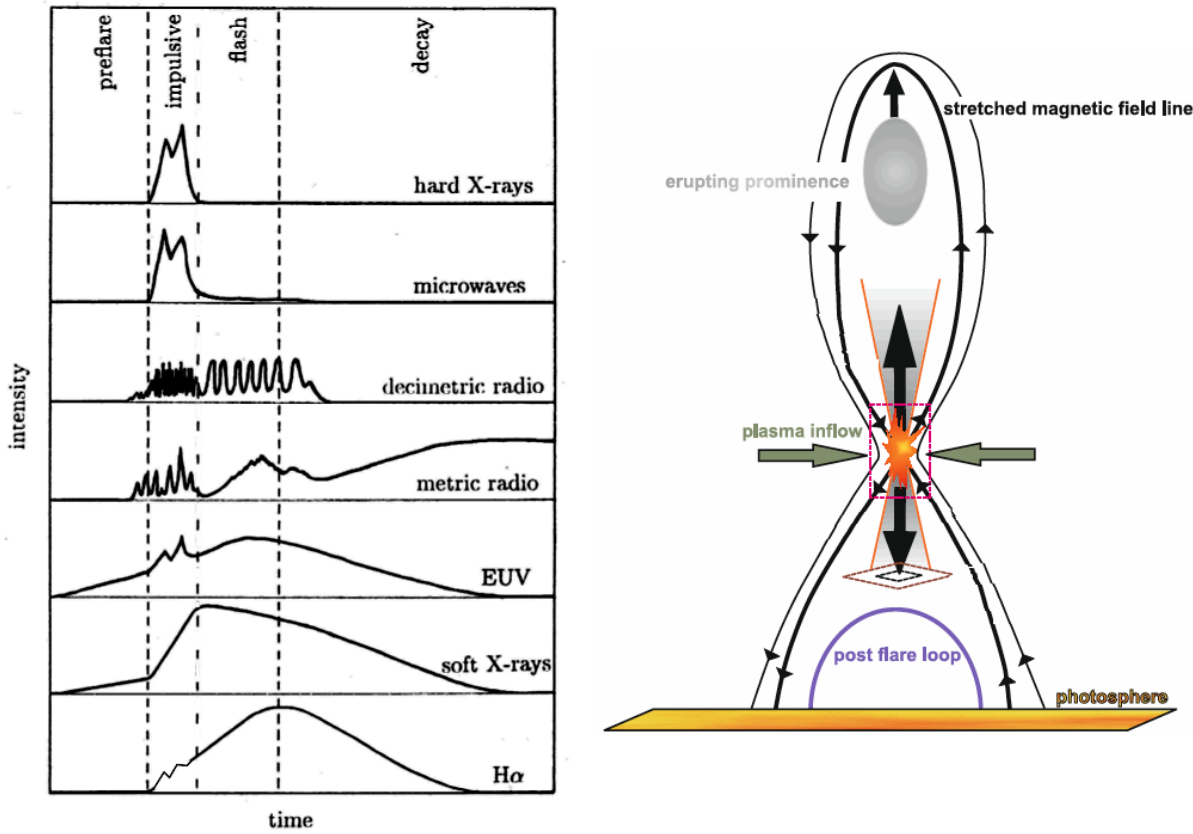


Figure 2.2: *Left* - Sketch of the emissions in different wavelength bands during flares. Image was taken from Benz (2008). *Right* - A schematic drawing of the standard model of solar flares. Image modified from the one presented in Mann et al. (2009).

The flare process is a sequence of phases, as indicated in the left panel of figure 2.2. Flares begin when magnetic loops interact and reconnect. The initial phase during which the magnetic field releases flare energy through reconnection is known as the *pre-flare phase*. The next stage of the flare process is the *impulsive phase*, where the particles are accelerated and the majority of the energy is released. HXR footpoint sources at the chromosphere and microwave-millimeter wave radiation are observed (Hudson 2011). During the *flash phase*, the intensity of H α and its line width rapidly increase (Benz 2008). Finally, during the *decay phase* we observe meter wave radio bursts and interplanetary particle events due to ejections and shock waves and the coronal plasma returns slowly to its stable state of minimum energy.

The standard picture of flares describes the physical processes in the solar atmosphere (see figure 2.2, right panel). After magnetic field lines reconnect in the corona, particles are accelerated in the reconnection zone. The accelerated particles follow the magnetic lines towards the surface and outwards into space. Particles traveling from the upper corona to the interplanetary medium emit in radio wavelengths. When particles arrive in the chromosphere, they are stopped by a thick target and heat this layer, a process known as *chromospheric evaporation*. The particles stopped by Coulomb collision emit in HXR due to bremsstrahlung free-free process. In some extremely energetic events, γ -rays are observed and they are produced by nuclear transitions.

The standard model of solar flares is called the CSHKP model after the scientists that developed it (Carmichael 1964, Sturrock 1966, Hirayama 1974, Kopp & Pneuman 1976). This model takes magnetic reconnection as the principal mechanism to release energy. Typical values of the energy release during flares are $\sim 10^{32}$ erg and they occur in a volume of $\sim 10^{30}$ cm 3 (Hudson 2011), thus the resulting energy density is $\mathcal{U}_{flare} \sim 100$ erg cm $^{-3}$. Energy densities from possible contributions of different types sources are: kinetic ($\mathcal{U}_{kinetic} = m_p n v^2 / 2 \sim 10^{-3}$ erg cm $^{-3}$), thermal ($\mathcal{U}_{thermal} = n k_B T \sim 10^{-1}$ erg cm $^{-3}$), gravitational ($\mathcal{U}_{gravitation} = m_p n g \sim 4 \times 10^{-1}$ erg cm $^{-3}$) and magnetic ($\mathcal{U}_{magnetic} = B^2 / 8\pi \sim 400$ erg cm $^{-3}$). The coronal magnetic field is able to store enough energy to produce flares. The soft X-ray (SXR) images of the solar corona are an evidence that solar flares are processes occurring in the corona. The plasma beta is defined as

$$\beta = \frac{\text{Thermal pressure}}{\text{Magnetic pressure}} = \frac{2\xi n_e k_B T_e}{B^2 / 8\pi}, \quad (2.1)$$

where ξ is an ionization parameter, n_e is the electron density, T_e is the electron temperature, k_B is the Boltzmann constant, and B is the magnetic field. When beta is low, the plasma is in the magnetically confined regime, i.e. the plasma follows the magnetic field lines. In most parts of the corona $\beta < 1$ (Aschwanden 2005) indicating that coronal structures such as loops can clearly be defined by the magnetic field, which suggests a correlation between flares that occurred in the coronal loops and the magnetic field.

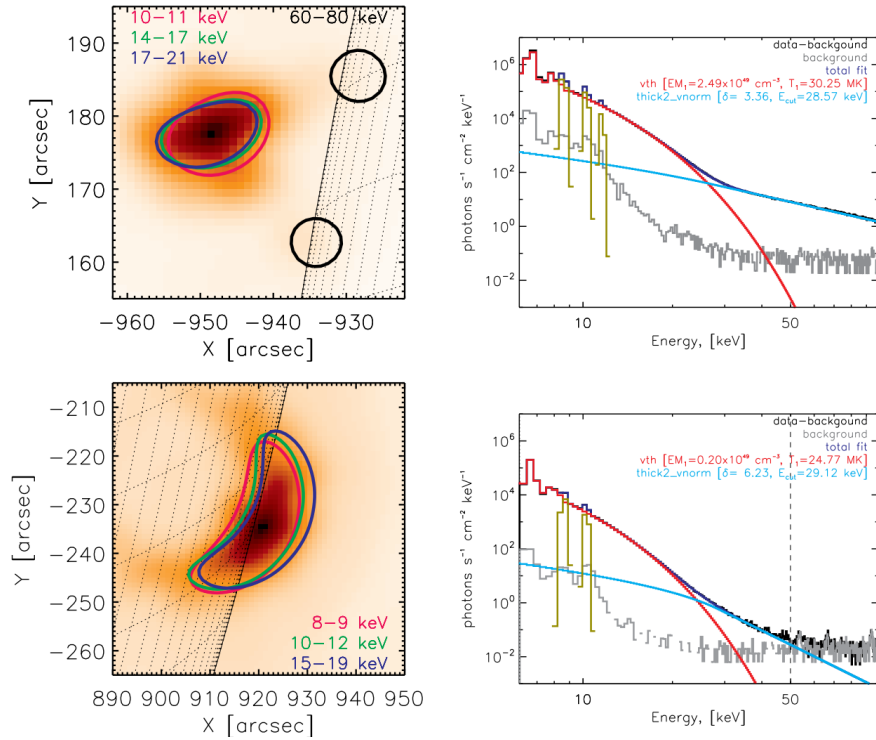


Figure 2.3: Example of the thermal and non-thermal emission during flares. *Left-* Location of the X-ray emission. Red, blue and green contours show the thermal emission from coronal loops with energies ranging from ~ 8 to ~ 21 keV. The black contours on the top-left map show the HXR footpoints of the flare measured in the energy band 60-80 keV. *Right-* The X-ray energy spectra for each flare taken with RHESSI (black line). The flare spectrum is governed by two main components: the thermal emission coming from particles trapped in the coronal loops that dominates the spectrum up to ~ 20 keV (red fit). The non-thermal bremsstrahlung emission produced by charged particle beams being stopped in a thick target (chromosphere). This radiation dominates at higher energies of the flare's spectrum (blue fit). The image was taken from Jeffrey et al. (2015).

The thick target model is considered the explanation of the HXR emission during flares. This model states that accelerated electrons propagate upwards and downward in the solar atmosphere. Particles that precipitate to lower layers are decelerated due to Coulomb collisions when they interact with a denser medium (a thick target) and emit HXR (Hudson 1972). Figure 2.3 shows the SXR and HXR footpoints during two solar flares, as well as the high-energy spectrum for both events.

The usual classification of solar flares is based on the SXR observations made by the Geostationary Operational Environmental Satellite (GOES) system. Observations by GOES have taken place since July 1974. GOES instruments measure the flux within 1 - 8 Å with a cadences of few seconds to one minute. The one-minute cadence data is used for the classification of flares. Thermal emission in this band is produced by particles in coronal loops after the reconnection process (Hudson 2011). Therefore, SXR emissions are a reliable measure for the classification of solar flares.

GOES Class	Flux 1-8 Å [W m ⁻²]
A	$F_{\text{SXR}} < 10^{-7}$
B	$F_{\text{SXR}} < 10^{-6}$
C	$F_{\text{SXR}} < 10^{-5}$
M	$F_{\text{SXR}} < 10^{-4}$
X	$F_{\text{SXR}} \geq 10^{-4}$

Table 2.1: GOES classification for flares. The F_{SXR} is the flux in SXR at a flare's maximum.

The logarithmic classification provided by GOES depends on SXR fluxes. Each peak in the GOES light-curve is considered a flare (see figure 2.4). Flares are labeled with letters A, B, C, M or X class depending on the flux of the peak to indicate its class. For instance, a flare with a SXR flux of $F_{\text{SXR}} = 7.3 \times 10^{-5} \text{ W m}^{-2}$ is classified as a M7.3 class flare. The corresponding letters to the flux are in Table 2.1. The particular GOES times for each event is automatically recorded. The GOES start time is reported as the first minute when there is a steep monotonic increase in SXR flux in a 4-minute sequence. The peak maximum is recorded when the X-ray light-curve achieves its maximum after the starting time. The flare ends when the flux level decays to a point halfway between the maximum X-ray flux and the pre-flare background level.

Coronal Mass Ejections (CMEs) are explosive events observed in the corona that eject large amount of plasma towards the interplanetary space. Coronagraphic observations of scattered white-light are used to measure CMEs. With this technique, the solar disk is blocked and just the scattered light from the corona is measured. Flares and CMEs are related phenomena, though there is not a one-to-one relation between them (Webb & Howard 2012). Very energetic flares may be triggers of CMEs. For instance, $\sim 90\%$ of X-class, $\sim 56\%$ of M-class, and $\sim 30\%$ of C-class flares are associated with CMEs (Chen 2011; Yashiro et al. 2005; Wang & Zhang 2007).

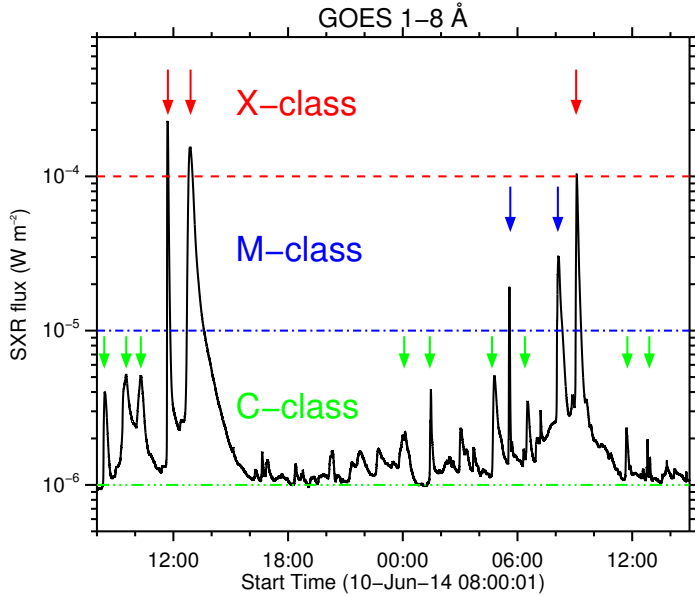


Figure 2.4: SXR lightcurve within 1 - 8 Å. Each peak in this plot represents a flare. The different classes of flares are indicated by the arrows, where red represents X-class, blue is assigned to M-class and green arrows point to C-class flares. Note that solar background is above 10^{-6} W m^{-2} which means that B and A flares are below the coronal emission during this day.

Figure 2.4 shows GOES observations during the 10th and 11th June, 2014. Each SXR light-curve peak represents a flare. Horizontal lines indicate the boundaries of the GOES classes. Colored arrows point to three X class flares (red) observed during this day, two M class flares (blue) and sixteen C class flares (green). A and B class flares are called micro- and nanoflares. During this time interval, the solar background was high enough to hide small events.

2.1 Irreversible Changes of the Magnetic Field During Flares

There is a close relation between solar flares and magnetic field restructuring. Observations have shown abrupt and persistent changes in the magnetic field during solar flares (e.g. Wang 1992, Cameron & Sammis 1999, Kosovichev & Zharkova 2001 Sudol & Harvey 2005, Petrie & Sudol 2010, Kleint 2016). The magnetic field changes stepwise with a sudden variation with duration of few minutes co-temporal with flares, and the magnetic field is changed permanently. Figure 2.5 shows an irreversible change of the magnetic field during an X-class flare SOL2012-10-23T03:17. In this thesis, we study these types of abrupt and permanent magnetic changes during 75 flares from the current solar maximum.

Solar magnetic fields were discovered in 1908 by G. E. Hale at Mount Wilson. Hale measured that the sunlight coming from a sunspot was circularly polarized, and he associated it with the Zeeman effect (see chapter §3). However, the idea that connects flares and magnetic field restructuring came in the 1930s, and it was not the 1990s, until the first clear evidence of photospheric magnetic field changes during flares was observed (Wang 1992). We follow now with a chronological sequence some of the pioneer works before the 1990s, and after, we present the current state of knowledge of non-transient changes of the magnetic field in the lower layers of the solar atmosphere.

Giovanelli (1939) related flares and magnetic fields. They associated the magnetic field, size and type of the sunspots with the occurrence of flares. Although, they did not find any correlation between the probability of occurrence of flares and magnetic fields mainly because sporadic daily measurements

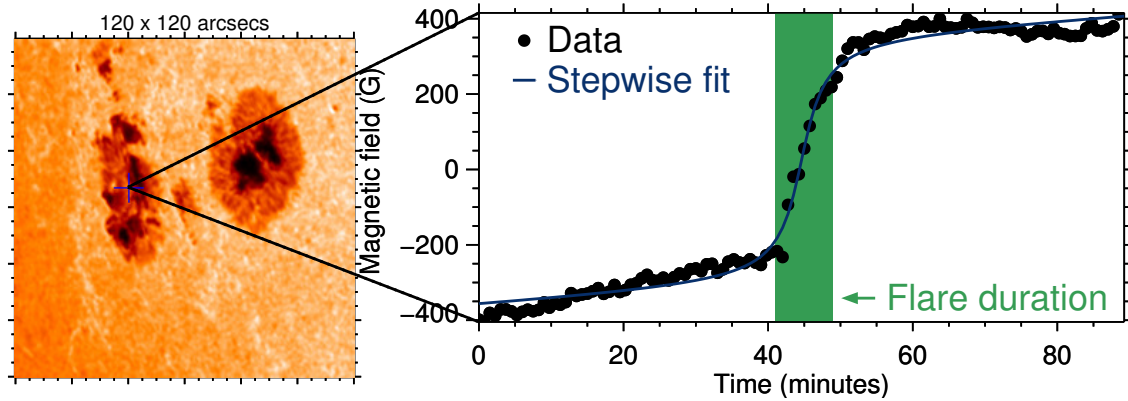


Figure 2.5: Example of a photospheric magnetic change during SOL2012-10-23T03:17 flare using the B_{LOS} data from the HMI instrument onboard the SDO satellite (black dots). The line is the best fit to the stepwise function from Sudol & Harvey (2005). The green interval represents the duration of the flare.

available at that time. Variations in the sunspot's area and the magnetic field have a relation with flares were observed (Howard & Severny 1963, Howard 1963). The evolution in instrumentation and techniques continued during the next two decades. For example, observations showed linear changes near the limb in magnetograms associated with a flare (Tanaka 1978). Patterson & Zirin (1981) claimed that during two flares there were regions that behaved particularly. The magnetic field changed transiently in some places of the active region, while in other parts, the field changed permanently. They claimed that a region disappeared one minute after the flare, and the field became weaker as a result of the permanent change. Patterson (1984) measured the magnetic field using two images in the spectral line Fe I 5324 Å. Firstly, the instrument took an image of the opposite circular polarization in the blue and red wings of the Fe I spectra line, and for the second image, the instrument switches the circular polarizers. The signal in the difference-image is proportional to the magnetic field. Patterson (1984) concluded that the magnetic transients were variations in the spectral line during flares that might produce artifacts.

It is believed that Wang (1992) discovered first permanent changes of the magnetic field. Wang (1992) found that the magnetic shear angle increased permanently after a flare. The magnetic shear is the angular difference between the measured transverse field and the transverse component of the calculated potential field. Abrupt increases of the magnetic shear coincident with the X-ray emission have been observed during the X-class flares (e.g. Wang et al. 1994). Although, not only increasing changes have been measured. In particular, Wang (2006) found increases in the magnetic shear during 3 X-class flares, while in other two events, the magnetic shear decreased. These type of abrupt and irreversible changes of the magnetic shear are accompanied by increases in the inclination of the magnetic field (e.g. Wang et al. 1996, Wang et al. 2012).

Flaring regions at photospheric heights show abrupt and non-transient changes of the magnetic field, and $\bar{\mathbf{B}}$ stays permanently changed for hours (e.g. Sudol & Harvey 2005, Petrie & Sudol 2010, Sun et al. 2012). More strong field changes in the line-of-sight (LOS) of the field occurred closer to the limb than near the disk-center, resulting in a correlation between the heliographic locations of the flares and their changes (Cameron & Sammis 1999, Petrie & Sudol 2010). This scenario might be explained in terms of a change in the geometry of the field. If the field tilts after the flare, the observed LOS component near the limb might change (Spirock et al. 2002).

Variations and flows in sunspots during flares may be associated with permanent changes. Magnetic field lines have seen tilting towards each other before an X-class flare, probably under the influence of external flows (Kosovichev & Zharkova 2001). Supersonic flows have been observed near the location of an X-class flare (Meunier & Kosovichev 2003). The disappearance of small sunspots, and the decay in penumbral regions have been observed almost simultaneously with flares (Wang et al. 2002a, Liu et al. 2005, Sudol & Harvey 2005).

Does the magnetic field change only in the photosphere? A recent study by Kleint (2016) found not only LOS-permanent changes in the photosphere during an X-class flare (Kleint et al. 2015, Kleint et al. 2016), but also, they discovered LOS-permanent changes in the chromosphere. They used spectropolarimetric data from the DST/IBIS ground-based instrument in the Ca II 8542 Å chromospheric spectra line to measure the LOS component of the field. The LOS-chromospheric changes ranged to 640 Gauss, and are stronger than the changes in the photosphere that have been measured (450 Gauss e.g. Sudol & Harvey 2005, Petrie & Sudol 2010, Johnstone et al. 2012, Burtseva et al. 2015, Kleint 2016).

The large energy emitted during flares may change the physical conditions of the line formation. During flares non-thermal electrons accelerated in the corona heat the plasma in the lower atmosphere. The changes in the thermodynamic result in the spectral line turning into emission and the movements of plasma produces Doppler shifts in the spectral lines (Qiu & Gary 2003, Ding et al. 2002). These type of variations in the spectral line may induce magnetic transients or sign reversal anomalies during the measurement of the magnetic field in a flaring atmosphere (e.g. Patterson & Zirin 1981, Zirin & Tanaka 1981, Patterson 1984, Kosovichev & Zharkova 2001).

It is still unclear if the field becomes stronger or weaker after the flare. Both scenarios of the longitudinal field increasing or decreasing have been observed in flares with different heliocentric locations (e.g. Cameron & Sammis 1999, Petrie & Sudol 2010). For example, Cliver et al. (2012), Kosovichev & Zharkova (2001) and Wang et al. (2002b) found that the unsigned fluxes increased. In contrast, Kleint (2016) reported that $\sim 60\%$ of the photospheric and chromospheric LOS-changes decreased the absolute value of B after the flare took place; and Burtseva & Petrie (2013) found considerably more regions where the magnetic flux decreases than increases. Usually a polarity changes more than the other, and permanent changes are not simultaneous in the two polarities (e.g. Wang et al. 2002b, Spirock et al. 2002).

The polarity inversion line (PIL) plays an important role in the flare production (e.g. Schrijver 2007, Falconer 1997). The PIL is the region that separates both positive and negative polarities. There are reports of movements and variations of the magnetic energy near the PIL during flares (Kosovichev & Zharkova 2001). The magnetic shear in the PIL changes permanently after flares (e.g. Wang et al. 1994). The photospheric changes occur near the PIL and tend to be located in regions with strong magnetic fields (e.g. Burtseva et al. 2015). Kleint (2016) found that the photospheric and the chromospheric LOS-permanent changes were not co-spatial: the chromospheric changes were located near the footpoints of loops, while, the photospheric changes occurred near the PIL. In addition, different studies have found permanent changes in the horizontal component near the PIL correlated with flares (e.g. Wang & Liu 2010, Wang et al. 2012, Petrie 2012, Petrie 2013, Sun et al. 2012).

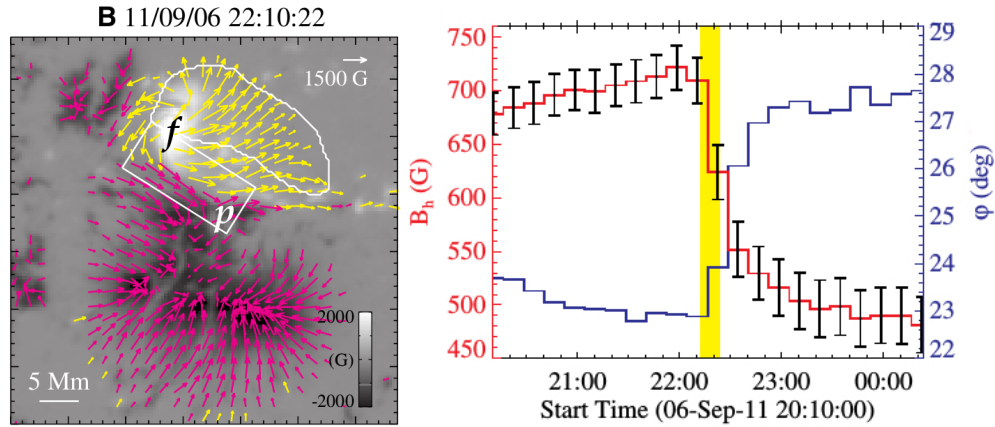


Figure 2.6: *Left* - Vector magnetic field before an X-class flare on September 6, 2011. *Right* - The mean temporal evolution of the longitudinal magnetic field and its inclination φ . Both magnetic field quantities showed irreversible changes as result of the flare. This image and further information can be found in Liu et al. (2014).

If irreversible changes are produced by the flare process, there must be a relation in time with other types of enhancements during flares. In particular, the photospheric permanent changes of B and the thermal emission in the 1 - 8 Å band are co-temporal, and occur during the impulsive phase of flares (Cliver et al. 2012). The timing of photospheric and chromospheric permanent changes of the field occurred with an onset up to 3 minutes (Kleint 2016). HRX emission and permanent changes are related during the early stage of the flare, though this correspondence is broken at later stages of the flare, when the HRX footpoints move away from the PIL (Burtseva et al. 2015).

During flares the lower solar atmosphere is heated and a correspondence between EUV/UV emission and permanent changes might be expected. Observations have shown that these phenomena are co-spatial. In particular, all photospheric irreversible changes occur in regions with chromospheric intensity enhancement, though not all chromospheric and coronal emission is accompanied by permanent changes (Johnstone et al. 2012, Kleint 2016). Also, high-energy particles that disturb lower layers of the solar atmosphere might produce the permanent changes of the field. Astronomers found that LOS-changes and HXR are co-temporal (Yurchyshyn et al. 2004, Cliver et al. 2012), and there is a controversy if these two phenomena are co-spatial or not. In some events, HXRs are observed at the same places of the LOS-changes during the impulsive phase of the flare (Petrie & Sudol 2010). On the other hand, irreversible changes are observed near the edges of HXR footpoints (Wang et al. 2002a, Kleint 2016), or the co-spatiality is lost at late state of HXR emission, when the HXR-kernels move away from the PIL (Petrie & Sudol 2010).

Permanent changes of the vector magnetic field have been observed as a consequence of flares (e.g. Wang et al. 1994, Wang et al. 2002b, Wang et al. 2012, Sun et al. 2012, Petrie 2013, Liu et al. 2014). The field has been observed more tilted and sheared after flares (e.g. Wang et al. 2012, Liu et al. 2014), however there are examples where the tilt angle did not change permanently (e.g. Petrie 2013). Figure 2.6 shows an example of the vector magnetic field before an X-class flare and its evolution. During this event, both horizontal field and inclination of the fields irreversibly changed by ~ 200 Gauss, and $\sim 5^\circ$, respectively. The horizontal component of the field near the PIL is found to increase its strength and become more parallel to the PIL (e.g. Petrie 2013, Sun et al. 2012). The generation of new penumbra region has been observed in one of such observations (Wang et al. 2002b).

How does the magnetic fields react after the coronal energy is released during a flare? Models suggest that the field becomes more horizontal after flare due to an *implosion* of the coronal fields (Hudson 2000). By *implosion* we mean that the magnetic lines contract after the flare process as a consequence of the energy conservation (Hudson 2000). From the observational point of view, different authors concluded that the implosion image of coronal-loops becoming more horizontal are observed during flares (e.g. Wang & Liu 2010, Petrie & Sudol 2010 ,Wang et al. 2012, Gosain 2012, Petrie 2013, Liu et al. 2014). Although, the spatial discrepancy between photospheric and chromospheric changes have shown the possibility that the field becomes untwisted, or that the height of the flare-loop after flares increase (Kleint 2016). In any of these scenarios, to produce the observed permanent changes in the photosphere/chromosphere, the energy must be transported from the corona. Alfvén wave pulses might be the mechanism that transports the coronal energy rapidly enough to permanently change the magnetic field in the lower atmosphere (Fletcher & Hudson 2008). The change of the horizontality of the magnetic field might produce a back reaction of coronal fields. The transmitted energy might produce seismic waves (sunquakes) in the photosphere as a consequence of the momentum conservation (Hudson et al. 2008 and Fisher et al. 2012). Observations have seen co-spatiality between sunquakes and permanent changes during flares (e.g. Alvarado-Gómez et al. 2012), though this is not always the case (Kleint 2016).

Previous studies have focused on extreme flares and used, in the majority of the cases, LOS measurements. In the past decades, significant advances have been done in the understanding of the relation between solar flare and abrupt and permanent changes of the magnetic field. But, there still are open questions in this field such as:

- Are the permanent changes of the photospheric magnetic field a cause or a consequence of the flare process?
- Are the permanent changes located above/in the umbra, penumbra and/or quiet Sun?
- Do the permanent changes modify the morphology of the active region?
- Do the permanent changes of the magnetic field have a relation with energy emitted during the flare?
- How is the magnetic shear produced?
- How are the magnetic field lines re-organized during flares?
- Is the strength of the field getting weaker or stronger due to the permanent changes?
- How does the topology of the photospheric/chromospheric magnetic field change?
- Does flux emergence or cancellation trigger the changes?
- Are the permanent changes and accelerated particles in upper layers related?
- Do the flare-loops decrease/increase their height during the flare?
- How does the twist of the field before and after the flare change?
- Is the twist correlated with irreversible changes?
- Does the Alfvén-wave mechanism transport the coronal energy and produce the permanent changes in the photosphere/chromosphere?
- Are the chromospheric and photospheric permanent changes produced by the same mechanism?
- What is the relation between the PIL and permanent changes?

In this thesis, we aim to tackle some of these questions using space-borne LOS and vector magnetic field measurements during 74 solar flares.

Chapter 3

Magnetic Fields on the Sun: Theory and Techniques

In this chapter, we present the theory behind magnetograms and vectorgrams, which is known as *spectropolarimetry*, based on Degl’Innocenti (2006), Stenflo (1994), and del Toro Iniesta (2003). We introduce the polarization of electromagnetic waves, and how the *Stokes parameters* describe the polarization states of electromagnetic waves. We use the Zeeman effect to describe how atoms respond to the presence of magnetic fields and how this field-matter interaction induces polarization of the observed sunlight. The measurements of photospheric magnetic fields are based on this effect. An *inversion code* is introduced, which is used to estimate the three components of the vector magnetic field. Finally, we describe how the Lorentz force is measured in the photosphere.

3.1 Polarization of Electromagnetic Waves

Maxwell’s equations describe the behavior of electric $\vec{\mathbf{E}}$ and magnetic $\vec{\mathbf{B}}$ fields as function of charge and current distributions, as well as the explicit variation of the fields with time. These equations summarize Coulomb’s law, Gauss’s law, Faraday’s law, Ampère’s law, and electric charge conservation. Maxwell equations in their differential form can be written as (Gauss units):

$$\nabla \cdot \vec{\mathbf{E}} = 4\pi\rho_c, \quad (3.1)$$

$$\nabla \cdot \vec{\mathbf{B}} = 0, \quad (3.2)$$

$$\nabla \times \vec{\mathbf{E}} = -\frac{1}{c} \frac{\partial \vec{\mathbf{B}}}{\partial t}, \quad (3.3)$$

$$\nabla \times \vec{\mathbf{B}} = \frac{4\pi}{c} \vec{\mathbf{j}}_c + \frac{1}{c} \frac{\partial \vec{\mathbf{E}}}{\partial t}, \quad (3.4)$$

where $\vec{\mathbf{E}}$ and $\vec{\mathbf{B}}$ are the electric and magnetic fields. c , ρ_c and $\vec{\mathbf{j}}_c$ represent the speed of light in vacuum, the electric charge density and the electric current density, respectively. The electric charge conservation is given by

$$\frac{\partial \rho_c}{\partial t} + \nabla \cdot \vec{\mathbf{j}}_c = 0. \quad (3.5)$$

By calculating the curl of equations 3.3 and 3.4 and applying a vector calculus identity one obtains the electromagnetic (EM) non-homogeneous wave equations given by

$$\begin{aligned}\nabla^2 \vec{\mathbf{E}} - \frac{1}{c^2} \frac{\partial^2 \vec{\mathbf{E}}}{\partial t^2} &= 4\pi \nabla \rho_c + \frac{4\pi}{c^2} \frac{\partial \vec{\mathbf{j}}_c}{\partial t}, \\ \nabla^2 \vec{\mathbf{B}} - \frac{1}{c^2} \frac{\partial^2 \vec{\mathbf{B}}}{\partial t^2} &= -\frac{4\pi}{c^2} \nabla \times \vec{\mathbf{j}}_c.\end{aligned}\quad (3.6)$$

Their homogeneous versions are the equations for electromagnetic waves:

$$\nabla^2 \vec{\mathbf{E}} - \frac{1}{c^2} \frac{\partial^2 \vec{\mathbf{E}}}{\partial t^2} = \vec{\mathbf{0}}, \quad \nabla^2 \vec{\mathbf{B}} - \frac{1}{c^2} \frac{\partial^2 \vec{\mathbf{B}}}{\partial t^2} = \vec{\mathbf{0}}, \quad (3.7)$$

with solutions:

$$\vec{\mathbf{E}}(t, \vec{\mathbf{r}}) = \vec{\mathbf{E}}_0(\omega) e^{i(\vec{\mathbf{k}} \cdot \vec{\mathbf{r}} - \omega t)}, \quad \vec{\mathbf{B}}(t, \vec{\mathbf{r}}) = \vec{\mathbf{B}}_0(\omega) e^{i(\vec{\mathbf{k}} \cdot \vec{\mathbf{r}} - \omega t)}. \quad (3.8)$$

The non-homogeneous equations 3.6 enable us to study the power emitted by different classical radiation processes, e.g. bremsstrahlung, synchrotron, dipole radiation, etc., while equations 3.7 tell us that once the electromagnetic wave is produced, it travels in vacuum at the speed of light c . In a medium with dielectric permittivity ϵ and magnetic permeability μ , the velocity of the EM wave is

$$v = \frac{c}{\sqrt{\epsilon \mu}} \equiv \frac{c}{n} \quad (3.9)$$

where n is the refractive index of the medium. It is customary to describe electromagnetic phenomena using the so-called scalar (Φ) and vector ($\vec{\mathbf{A}}$) potentials. These potentials are not uniquely defined unless we introduce an appropriate gauge. With these potentials the electric and magnetic fields are given by

$$\vec{\mathbf{E}} = -\nabla \Phi - \frac{1}{c} \frac{\partial \vec{\mathbf{A}}}{\partial t}, \quad \vec{\mathbf{B}} = \nabla \times \vec{\mathbf{A}}. \quad (3.10)$$

If we replace equations 3.10 into Maxwell equations 3.1 and 3.4 which contain the sources, and using the Lorentz gauge:

$$\nabla \cdot \vec{\mathbf{A}} + \frac{1}{c} \frac{\partial \Phi}{\partial t} = 0, \quad (3.11)$$

one obtains two non-homogeneous equations

$$\nabla^2 \Phi - \frac{1}{c^2} \frac{\partial^2 \Phi}{\partial t^2} = -4\pi \rho_c, \quad \nabla^2 \vec{\mathbf{A}} - \frac{1}{c^2} \frac{\partial^2 \vec{\mathbf{A}}}{\partial t^2} = \frac{4\pi}{c} \vec{\mathbf{j}}_c. \quad (3.12)$$

In radiation problems, we consider only the vector potential with the Coulomb gauge, $\nabla \cdot \vec{\mathbf{A}} = 0$, such that the electromagnetic wave equations are given by:

$$\nabla^2 \vec{\mathbf{A}} - \frac{1}{c^2} \frac{\partial^2 \vec{\mathbf{A}}}{\partial t^2} = \vec{\mathbf{0}}, \quad (3.13)$$

whose solution of equation 3.13 is given by

$$\vec{\mathbf{A}}(t, \vec{\mathbf{r}}) = \vec{\mathbf{A}}_0(\omega) e^{i(\vec{\mathbf{k}} \cdot \vec{\mathbf{r}} - \omega t)}. \quad (3.14)$$

Due to the Coulomb gauge EM waves are transverse. This condition can be seen by the relations

$$\vec{\mathbf{B}} = \hat{\mathbf{k}} \times \vec{\mathbf{E}}, \quad \vec{\mathbf{E}} = \vec{\mathbf{B}} \times \hat{\mathbf{k}}, \quad (3.15)$$

where $\hat{\mathbf{k}} = \vec{\mathbf{k}} / ||\vec{\mathbf{k}}||$, $k = 2\pi/\lambda$, and in vacuum one has $k = \omega/c$; $\hat{\mathbf{k}}$ is the unit vector in the direction of the wave propagation, i.e. in the direction of the wave vector $\vec{\mathbf{k}}$. The surface normal to vector $\hat{\mathbf{k}}$ is called the wave front and contains the electric and magnetic fields associated to an EM wave. Equations 3.15 determine the existence of only two independent components of $\vec{\mathbf{E}}$ (and $\vec{\mathbf{B}}$) that can be written as

$$\vec{\mathbf{E}} = \hat{e}_1(\hat{\mathbf{k}})E_1 + \hat{e}_2(\hat{\mathbf{k}})E_2, \quad (3.16)$$

for the electric field. These components correspond classically to the polarization states of the EM wave. We decompose the vector potential in terms of the EM wave polarization as

$$\vec{\mathbf{A}}(t, \vec{\mathbf{r}}) = \sum_{\vec{\mathbf{k}}, \alpha} \left[\hat{\mathbf{e}}_\alpha(\hat{\mathbf{k}})a_\alpha(\vec{\mathbf{k}})e^{i(\vec{\mathbf{k}} \cdot \vec{\mathbf{r}} - \omega t)} + \text{c.c.} \right], \quad (3.17)$$

where $a_\alpha(\vec{\mathbf{k}})$ is a scalar amplitude, $\hat{\mathbf{e}}_\alpha(\hat{\mathbf{k}})$ are the unit vectors perpendicular to the wave vector $\vec{\mathbf{k}}$, and c.c. stands for the ‘complex conjugate’. According to equation 3.17 the vector potential $\vec{\mathbf{A}}$ is a real vector. The energy flux density carried by the EM-wave is given by the Poynting vector

$$\vec{\mathbf{S}} = \frac{c}{4\pi} \vec{\mathbf{E}} \times \vec{\mathbf{B}}. \quad (3.18)$$

EM-waves are transverse waves, i.e. the oscillating plane is perpendicular to the propagation axis. EM-waves can be described by their polarization states due to their transverse nature. The actual direction of oscillation determines the polarization of the wave. This quantity is characterized in a fixed plane as seen from the direction of the observer. The general elliptical polarization state is given by

$$\frac{E_{0,x}^2}{a_{0,x}^2} + \frac{E_{0,y}^2}{a_{0,y}^2} - 2 \frac{E_{0,x}}{a_{0,x}} \frac{E_{0,y}}{a_{0,y}} \cos \delta = \sin^2 \delta, \quad (3.19)$$

where $a_{0,i}$ is the real amplitude of the EM-wave in the xy -plane and $\delta \equiv \delta_x - \delta_y$ is the phase difference between the x and y components. The special cases are

Case I: If $\delta = 0$ or π , the equation (3.19) becomes linear, which determines the linear polarization of the monochromatic wave.

Case II: If $a_x = a_y$ and $\delta = \pi/2$ or $3\pi/2$, the equation (3.19) degenerates to a circle, which yields the circular polarization states.

Case III: If none of the conditions of cases I or II apply, then the EM-wave has an elliptical polarization state.

In cases II and III, if $\sin \delta > 0$ the EM-wave rotates clockwise. In this situation the light is said to be right-handedly polarized. If $\sin \delta < 0$, the monochromatic wave rotates counter-clockwise, and the light is left-handedly polarized.

3.2 Stokes Parameters

Any polarization state such as linear, circular, elliptical or natural light (unpolarized) of an electromagnetic wave can be described by four quantities known as *Stokes parameters*. These quantities specify the total intensity and the polarization state of the light. From the observational point of view, detectors measure the energy carried by the EM-wave which is given by the square of the amplitude of the electric field carried by the wave. The electric and magnetic field can be decomposed into two independent components as

$$\vec{E} = \hat{e}_x(\hat{\mathbf{k}})E_{0,x} + \hat{e}_y(\hat{\mathbf{k}})E_{0,y}. \quad (3.20)$$

where E_i are the amplitudes of the field, and the unit vectors \hat{e}_k form an orthogonal base. Let us define the Jones vector as

$$\mathbf{J} = \begin{pmatrix} E_{0,x} \\ E_{0,y} \end{pmatrix}. \quad (3.21)$$

When the field \mathbf{J} passes through a medium its polarization state changes to \mathbf{J}' . The interaction with the medium can be described by a 2×2 matrix \mathbf{w} as

$$\mathbf{J}' = \mathbf{w}\mathbf{J}. \quad (3.22)$$

For example, two ideal linear polarizers at 0° and 45° can be described in terms of a \mathbf{w} matrix as

$$\mathbf{w}_{0^\circ} = \begin{pmatrix} 0 & 1 \\ 0 & 0 \end{pmatrix}, \quad \mathbf{w}_{45^\circ} = \frac{1}{2} \begin{pmatrix} 1 & 1 \\ 1 & 1 \end{pmatrix}. \quad (3.23)$$

Let us define the coherence matrix \mathbf{C} for a transverse EM-wave propagating along the z -axis as

$$\mathbf{C} \equiv \mathbf{J}\mathbf{J}^\dagger \equiv \begin{pmatrix} E_{0,x}(t)E_{0,x}^*(t) & E_{0,x}(t)E_{0,y}^*(t) \\ E_{0,y}(t)E_{0,x}^*(t) & E_{0,y}(t)E_{0,y}^*(t) \end{pmatrix}, \quad (3.24)$$

where diagonal terms are proportional to the total intensity of the wave, and non-diagonal terms describe the phase correlation between the x and y components of the EM-wave. The coherence matrix has two properties

$$\text{Tr}(\mathbf{C}) = E_{0,x}^2(t) + E_{0,y}^2(t) \geq 0, \quad (3.25)$$

$$\det(\mathbf{C}) = \mathbb{C}_{11}\mathbb{C}_{22} - \mathbb{C}_{12}\mathbb{C}_{21} \geq 0. \quad (3.26)$$

Equation (3.25) states that the intensity of a given beam is equal or greater than zero, i.e., negative intensities do not have physical meaning. Equation (3.26) is connected to the degree of polarization of the wave. Let us define the *Stokes parameters* as four real quantities obtained by linear combinations of the coherence matrix elements (del Toro Iniesta 2003) as:

$$\begin{aligned} I &\equiv \kappa(\mathbb{C}_{11} + \mathbb{C}_{22}) = \kappa [E_{0,x}^2(t) + E_{0,y}^2(t)], \\ Q &\equiv \kappa(\mathbb{C}_{11} - \mathbb{C}_{22}) = \kappa [E_{0,x}^2(t) - E_{0,y}^2(t)], \\ U &\equiv \kappa(\mathbb{C}_{21} + \mathbb{C}_{12}) = 2\kappa [E_{0,x}(t)E_{0,y}(t)\cos\delta(t)], \\ V &\equiv i\kappa(\mathbb{C}_{21} - \mathbb{C}_{12}) = 2\kappa [E_{0,x}(t)E_{0,y}(t)\sin\delta(t)], \end{aligned} \quad (3.27)$$

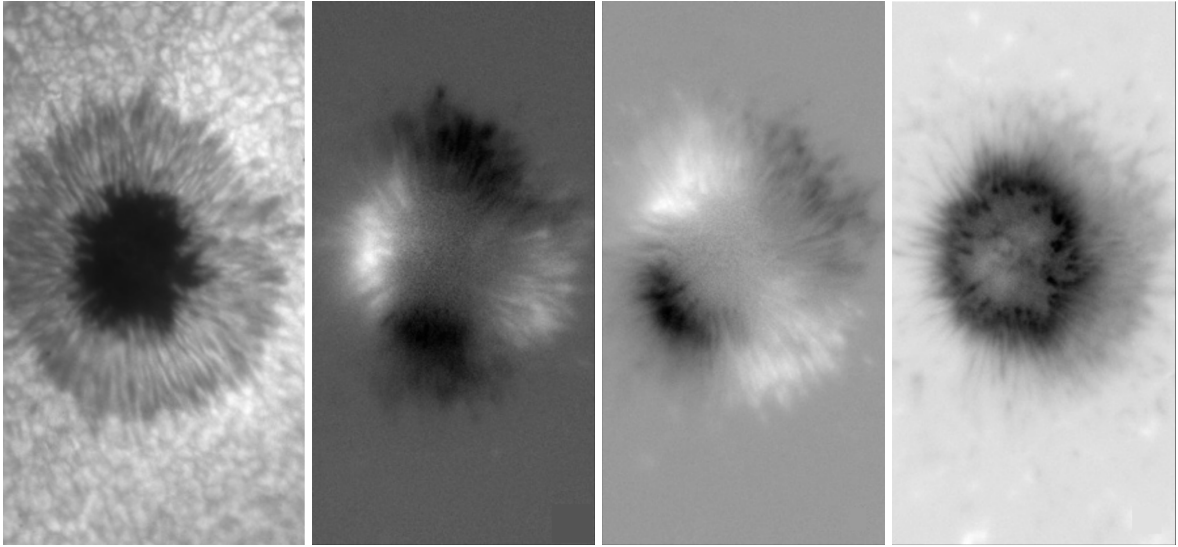


Figure 3.1: Sunspot images of the four Stokes parameters I, Q/I, U/I, V/I in the absorption line Fe 6302 Å, February 5, 2007. Images were taken from Kleint (2006).

where $\delta(t)$ is the difference between the x and y phases, and κ is a dimensional constant factor used to express the four parameters into intensity units. The total intensity of the incoming wave is described by I, while Q and U are obtained through the measurement of the linear polarization states, and V describes the circular polarization state of the EM-wave. I, Q, U and V can be derived by measuring the total intensity of the incoming light (I), and its intensity after it passes linear polarizers at certain degrees ($0^\circ, 45^\circ, -45^\circ, 90^\circ$), and the intensities after the light passes the right-handed (RHC) and the left-handed (LHC) circular polarizers. The measured relations can be written as

$$\begin{aligned} I &= I, \\ Q &= I_{0^\circ} - I_{90^\circ}, \\ U &= I_{45^\circ} - I_{-45^\circ}, \\ V &= I_{\text{RHC}} - I_{\text{LHC}}. \end{aligned} \tag{3.28}$$

Anisotropies in a medium induce or change the polarization states of the light as passes through it. In the case of the solar atmosphere, the magnetic field breaks the isotropic configuration and polarizes sunlight. By measuring the state of the polarization of the sunlight, solar physicists extract information about the magnetic fields in the Sun based on remote-sensing observations (see below). For example, strong magnetic fields are observed in sunspots. Images of the four Stokes parameters of a sunspot observed on February 5, 2007 are illustrated in figure 3.1 (obtained by Kleint 2006). The intensity image on the left shows a quasi-symmetric sunspot with an umbra (the darkest region on the image center), and a penumbra surrounding the umbra. The sunspot is located almost on the solar center, which means that the magnetic field in the umbra can be considered as pointing towards the observer. The two images in the middle show the linear polarization induced by the magnetic field (Stoke Q and U). The black-and-white pattern indicates perpendicular linear polarization states, which are related to the orientation of the tilted magnetic field in the penumbra. Stoke V is shown on the right. Stokes V shows signal most on the umbra where the magnetic field is *almost*-vertical.

3.3 Zeeman Effect

When an external magnetic field is applied to an element, its energy levels split into multiple states, and the radiation coming from the different transitions is polarized. The splitting of the energy levels in an atom due to the presence of an external magnetic field is called *the Zeeman effect*. This effect was first observed by the Dutch physicist Pieter Zeeman in 1897. A decade later, the US astronomer George Ellery Hale found observational evidence of the Zeeman effect in sunspots (Hale 1908). Hale, at the Mount Wilson Observatory, measured that the light of a doublet observed in a sunspot was circularly polarized. This was the first proof of the existence of magnetic fields on the Sun.

The Zeeman effect explains the energy states degeneracy of an atom in the presence of magnetic fields. The classical Hamiltonian of an electron in an external electromagnetic field is

$$\hat{\mathbf{H}}_0 = \frac{1}{2m}(\hat{\mathbf{p}} + \frac{e}{c}\hat{\mathbf{A}})^2 + V(r), \quad (3.29)$$

where $\hat{\mathbf{A}}$ is the vector potential and $V(r)$ is a central electrostatic potential. The eigenvalue E_j of the unperturbed Hamiltonian of an energy state is characterized by the quantum numbers l , s , j and m as

$$\hat{\mathbf{H}}_0|lsjm\rangle = E_j|lsjm\rangle. \quad (3.30)$$

If an external magnetic field $\vec{\mathbf{B}}$ along the z -axis is applied to the system, one has to add a term $\hat{\mathbf{H}}_B$ in the total Hamiltonian given by

$$\hat{\mathbf{H}}_B = \vec{\mu} \cdot \vec{\mathbf{B}} + \mathcal{O}(\mathbf{B}^2), \quad (3.31)$$

where $\vec{\mu}$ is intrinsic magnetic momentum of the atom, and $\mu_0 = 9.27 \times 10^{-21}$ erg G $^{-1}$ is the Bohr magneton. Let us define the *Landé g-factor* for a given energy state as

$$g = 1 + \frac{j(j+1) - l(l+1) + s(s+1)}{2j(j+1)}. \quad (3.32)$$

Note that $j \neq 0$ since $m = 0$ and the external magnetic field would become zero. The Hamiltonian eigenvalues of the perturbation produced by the external field for the linear Zeeman effect are

$$\langle lsjm|\hat{\mathbf{H}}_B|lsjm\rangle = mg\hbar\omega_L = mghv_L, \quad (3.33)$$

where $v_L = \frac{e_0 B}{4\pi mc}$ is the Larmor frequency. As a consequence, a given transition between a lower (l) and an upper (u) energy level, the Zeeman components can be written as

$$v_{m_u m_l} = v_0 + v_L(g_u m_u - g_l m_l), \quad (3.34)$$

where v_0 is the frequency of the transition without magnetic field interaction, g_l , g_u the Landé factors, and m_l , m_u are the total angular momentum eigenvalues for the two energy levels. The transitions follow the electric-dipole selection rules as

$$\begin{aligned} \Delta j &= \pm 1, \text{but } j = 0 \text{ is forbidden,} \\ \Delta l &= \pm 1, \Delta s = 0, \\ \Delta m &= 0, \pm 1. \end{aligned} \quad (3.35)$$

In the *normal Zeeman effect* three transitions are observed. The π component is the unperturbed spectral line. The σ_r transition refers to the displaced line to the red part of the spectra. The σ_b component is the blue-shifted. Solar magnetism is investigated via the Zeeman effect because the π and σ components are polarized.

The components and polarization states that can be observed depend on the direction of the magnetic field with respect to the observer. There are two main cases: the so-called longitudinal and transverse Zeeman effect. In the first scenario, the field is aligned to the LOS which results in two opposite circularly polarized components σ_r and σ_b . In the second case, the field is perpendicular to the LOS. In that case, the three components σ_r , σ_b and π are observed to be linearly polarized. σ transitions have a linear polarization state perpendicular to the direction of the field. The direction of the linear polarization of the π component is parallel to the field.

When magnetic fields are observed on the solar surface, e.g. in sunspots, the polarization signal that reaches to the telescope depends on the location of the sunspot on the solar disk. For instance, let us describe a scenario where we are observing a sunspot's umbra. The magnetic field in the umbra can be assumed to be perpendicular to the solar surface. If the sunspot is located at the solar center (LOS), the field is pointing to the direction of the observer. This is the case of the longitudinal Zeeman effect, and the sunlight from this region is circularly polarized. If the sunspot is no longer at disk center, the magnetic field of the umbra keeps pointing normal to the solar surface. From the observer point of view, the field now has a transverse and longitudinal component, and polarimetric signatures in Stokes Q, U, and V are recorded. In this case, a combination of the transverse Zeeman effect (linear polarization states) and the longitudinal Zeeman effect (circular polarization states) is observed.

3.4 Deriving the Solar Magnetic Field

As light travels along the solar atmosphere its polarization state changes due to the interaction with matter, and the presence of the magnetic field. In the next sections, we introduce how the HMI-team retrieves the LOS fields and the full vector magnetic fields. These sections do not attempt to give a detailed description of the HMI-pipeline, HMI-inversion code or the spectropolarimetry formalism (see e.g. Degl'Innocenti 2006, Hoeksema et al. 2014, Borrero et al. 2011).

3.4.1 Full Magnetic Field Vector: Inversion Techniques

It is almost impossible to measure solar magnetic fields in-situ. Solar physicists have inferred the three components of the field by the knowledge of how the polarized radiation is transported through the solar atmosphere. The radiative transfer equation (RTE) for polarized light describes how the intensity and polarization states of the light, the Stokes parameters, change in an anisotropic medium. The interaction of field and matter depends on the parameters of the atmosphere where the light passes through.

The inversion techniques solve the RTE to calculate synthetic Stokes parameters and compare them with the observed Stokes I^{obs} , U^{obs} , Q^{obs} and V^{obs} . The inversion codes iteratively modify the conditions of the atmosphere (medium) until the solution of the RTE is the same as the observed polarization.

Usually, the atmospheric models have a large number of free parameters, for example, 11 in the case of HMI's inversion code. The importance of each inversion code is how it weighs and reduces the space of the free parameters based on physical and mathematical arguments, to obtain the synthetic profiles output that fit the observations best.

In this thesis, data from the Helioseismic and Magnetic Imager onboard the Solar Dynamics Observatory is used. The HMI team uses *the Very Fast Inversion of the Stokes Vector for the Helioseismic and Magnetic Imager* inversion code (VFISV - Borrero et al. 2011, Centeno et al. 2014). The VFISV code works with 11 parameters to model the solar atmosphere, and as a result, it obtains synthetic profiles of the four Stokes parameters. The atmospheric parameters for VFISV are:

$$\mathcal{M} = \{|\vec{\mathbf{B}}|, \gamma, \psi, S_0, S_1, \eta_0, a, \Delta\lambda_D, v_{\text{LOS}}, V_{\text{mac}}, \alpha\}. \quad (3.36)$$

Those parameters can be classified as follows

Magnetic field parameters:

- $|\vec{\mathbf{B}}|$: Magnetic field strength constant with depth.
- γ : Inclination of the magnetic field with respect to the observer constant with depth.
- ψ : Azimuth of the magnetic field in the plane perpendicular to the observer constant with depth.

Thermodynamic parameters:

- S : Source function $S = S_0 + S_1\tau$, where τ is the optical depth and
 - S_0 : Source function at the outer layers of the atmosphere of the photosphere.
 - S_1 : Gradient of the source function along the atmosphere. In the case of VFISV atmosphere, the source function varies linearly with optical depth.

The source function is defined as the ratio between the emission coefficient and the absorption coefficient. The source function is equal to the Planck's blackbody radiation field when the medium is in local thermodynamic equilibrium.

- η_0 : The center to continuum absorption coefficient.
- a : Damping parameter, which is the electron dipole oscillation approximated as a simple harmonic oscillator.
- $\Delta\lambda_D$: Doppler width of the spectral line. For the Fe I 6173 Å Zeeman triplet the numerical Doppler width is (Borrero et al. 2011): $\Delta\lambda_D = \pm 4.66685 \times 10^{-10} [\text{m}\text{\AA}]$.

Kinematic parameters:

- v_{LOS} : LOS velocity of the plasma.
- V_{mac} : Macroturbulent velocity. This parameter accounts for turbulent motions which are not resolved and broaden the Stokes profiles.

Filling factor

- α : A geometrical parameter that defines which percentage of the resolution element is filled with magnetic fields.

HMI records 13.5 million pixels every 12 minutes. To diagnose the atmospheric parameters in every single pixel, and to accomplish the large computational power required, the HMI's team uses a Milne-Eddington atmosphere. This approximation simplifies thermodynamic parameters resulting in a time saving. The Milne-Eddington model assumes that the atmosphere is plane-parallel, and the important parameters in the line formation such as the damping, the Doppler width of the line, the center to continuum absorption coefficient, the magnetic field and the LOS velocity are constant along the solar atmosphere. In other words, these parameters do not depend on the height, and they are independent of the optical depth.

After the atmospheric parameters \mathcal{M} are selected, the inversion code produces synthetic profiles of the four Stokes parameters (I_j^{syn} , $j = 1, \dots, 4$). Afterward, the synthetic Stokes profiles are compared to the four observational Stokes profiles (I_j^{obs}) using a χ^2 -minimization procedure given by

$$\chi^2 = \frac{1}{4L - F} \sum_{i=1}^L \sum_{j=i}^4 \left[I_j^{obs}(\lambda_i) - I_j^{syn}(\lambda_i, \mathcal{M}) \right]^2 \frac{\omega_{ij}^2}{\sigma_i^2}, \quad (3.37)$$

where $4L - F$ refers to the free parameters of the inversion. σ_i and ω_{ij} are the noise level and weight function of the Stokes parameters, respectively. The code uses a non-linear least square algorithm to minimize χ^2 . If the merit function χ^2 is far from its minimum, the code suggests modifications of the atmospheric parameters. In each iteration, the atmospheric parameters are modified slightly, and then the four synthetic Stokes profiles are re-calculated. This closed loop remains until the merit function achieves its minimum with a synthetic model of the atmosphere that fits the observed Stokes parameters best. Once the inversion code has inferred the atmospheric parameters, one obtains the magnetic field strength $|\vec{B}|$, the inclination with respect to the observer γ and the azimuth ψ of the vector magnetic field, plus the other eight parameters.

3.4.2 Line-of-Sight Component

The HMI-algorithm directly measures the spectral line splitting due to the presence of the magnetic field (the Zeeman effect, see §3.3). This method is used to estimate the LOS magnetic fields without solving the radiative transfer equation. The HMI-algorithm determines the right- and left-circular polarization velocities, which correspond to the σ_b and σ_r blue- and red-shifted Zeeman components. The algorithm assumes that the line has a Gaussian shape, and it is expanded in Fourier series until the second order to measure velocities in circular polarization (see Couvidat & the HMI team 2011, Couvidat et al. 2012a). Due to the reduced number of sampling points in the Fe I spectral line (6 filters), look-up tables from simulations are used to correct the Doppler velocities. With both left- and right-circular polarized velocities (V_{RCP} and V_{LCP} , respectively), the LOS magnetic fields are calculated as

$$B_{LOS} = \frac{V'_{LCP} - V'_{RCP}}{K_m}, \quad (3.38)$$

where $K_m = (2.0 \times 4.67 \cdot 10^{-5} \times 0.000061733433 \times 2.5 \times 299792458.0)$ for a Landé g-factor of 2.5 of the Fe I line.

3.5 Lorentz Force

The force that moving charged particles feel in the presence of an electromagnetic field is known as the Lorentz force. We aim to understand how the flare process disturbs the photosphere in the regions where permanent changes are observed. By studying the Lorentz force in the photosphere, we can estimate the work done by this force due to the irreversible change of the field. This section introduces the analytic approach to calculate the Lorentz force following the description by Hudson et al. (2008) and Fisher et al. (2012). Let us write the Lorentz force per unit volume as

$$\vec{f}_L = \nabla \cdot \mathbf{T} = \frac{\partial T_{ij}}{\partial x_j}, \quad (3.39)$$

where T_{ij} is the Maxwell stress tensor in Cartesian coordinates for a magnetic field \vec{B} . T_{ij} is expressed as

$$T_{ij} = \frac{1}{8\pi} (2B_i B_j - B^2 \delta_{ij}), \quad (3.40)$$

δ being the usual Kronecker δ -function. Regarding the heliospheric components of the field (B_X , B_Y , B_Z) the Maxwell stress tensor can be written as

$$\mathbf{T} = \frac{1}{8\pi} \begin{pmatrix} B_Z^2 - B_X^2 - B_Y^2 & 2B_Z B_X & 2B_Z B_Y \\ 2B_Z B_Y & B_X^2 - B_Z^2 - B_Y^2 & 2B_X B_Y \\ 2B_Z B_X & 2B_X B_Y & B_Y^2 - B_Z^2 - B_X^2 \end{pmatrix}. \quad (3.41)$$

To calculate the total Lorentz force, the integral over the volume is evaluated using Gauss's divergence theorem

$$\vec{F}_L \equiv \int_V \frac{\partial T_{ij}}{\partial x_j} d^3x = \iint_{A_{tot}} T_{ij} n_j dA, \quad (3.42)$$

where n_j is the component of the unit normal vector pointing outward of the solar surface. After the substitution of the Maxwell stress tensor, the result is

$$\vec{F}_L = \frac{1}{8\pi} \iint_{A_{tot}} [2\vec{B}(\vec{B} \cdot \hat{n}) - \hat{n}B^2] dA. \quad (3.43)$$

Fisher et al. (2012) assumed a square volume with its boundaries ranging from the photosphere to some higher height above the active region. The upper edges and the walls of the box are negligible. This implies that only the lower limit, where the field is strong, contributes to the integral. In this case, the radial component can be expressed as $\hat{n} = -\hat{r}$ and $\vec{B} \cdot \hat{n} = -B_r$. Integrating over the surface, the resulting radial (F_r) and the horizontal (\vec{F}_h) components of the Lorentz force are

$$F_r = \frac{1}{8\pi} \int_{A_{ph}} (B_h^2 - B_r^2) dA, \quad (3.44)$$

and

$$\vec{F}_h = -\frac{1}{4\pi} \int_{A_{ph}} B_r \vec{B}_h dA. \quad (3.45)$$

A_{ph} is the photospheric area where the integration takes place. In chapters 5 and 6 the steps to calculate the Lorentz force from HMI LOS and vector magnetic field data are described, as well as the observational results, and their interpretation of the physics of solar flares.

Chapter 4

Data, Sample, and Methodology

In this chapter, we present an overview of the instruments and the data used in this study, as well as the flare sample and the conditions for choosing the events in our survey. Finally, in the last section of the chapter we describe the methodology followed for the data analysis.

4.1 The Solar Dynamics Observatory

The Solar Dynamics Observatory (SDO, Pesnell et al. 2012) has excellent capabilities to study solar flares. It has a large variety of observational products with a high cadence, is free from astronomical seeing, and has 24-hour coverage except during the two eclipse seasons near the equinoxes. SDO was launched in February 2010 to study solar variability and its relationship with space weather and Earth. This satellite flies with three instruments: The Helioseismic and Magnetic Imager (HMI, Schou et al. 2012), the Atmospheric Imaging Assembly (AIA, Lemen et al. 2012) and the Extreme Ultraviolet Variability Experiment (EVE, Woods et al. 2012). A sketch of the three instruments onboard SDO and a photo taken during SDO assembly are shown in figure 4.1.

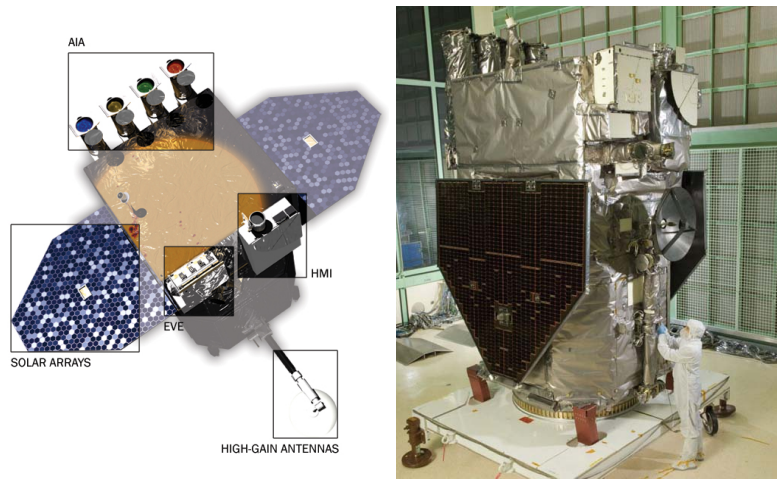


Figure 4.1: The Solar Dynamics Observatory. The image on the left shows the three instruments onboard SDO. The right picture was taken during the integration. All credits www.nasa.gov.

The three instruments onboard SDO measure different spectral ranges of solar radiation. The AIA instrument consists of four cameras that capture EUV images in ten different passbands. Each filter observes different height ranges in the solar atmosphere with a twelve-second cadence on average. Seven of these images observe highly ionized Fe and He II lines of the corona and the transition region at wavelengths: 94 Å, 131 Å, 171 Å, 193 Å, 211 Å, 304 Å, 335 Å. The other two passbands, centered at 1600 Å and 1700 Å, capture images of the chromosphere from the continuum and a carbon line. The last filter observes the photosphere at 4500 Å every hour.

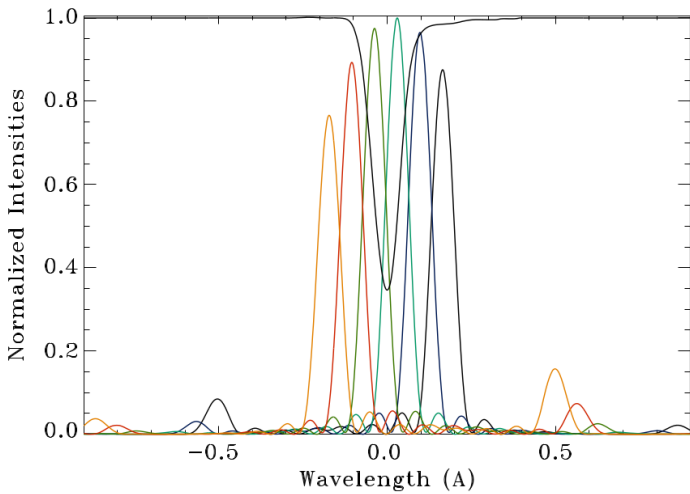


Figure 4.2: The HMI six tuning-position profiles in the Fe I solar line at disk center. The black line profile was measured at the Mount Wilson Observatory. Image from Schou et al. (2012).

employs an algorithm (Couvidat et al. 2012a) to obtain Dopplergrams, magnetograms and continuum images every 45 seconds.

HMI's second camera, the so-called vector camera, measures the full Stokes vector with a cadence of 135 seconds; however, to improve the signal-to-noise ratio, the data is averaged to a 720 seconds cadence. Hoeksema et al. (2014) explained in detail the series of software modules implemented in order to produce the scientific observables. One of the HMI data sets for the vector magnetic field is the Spaceweather HMI Active Region Patch (SHARP, Bobra et al. 2014). For this scientific product, the HMI-team automatically detects and tracks every active region in the photosphere as they rotate on the visible side of the solar disk, using LOS magnetograms and intensity images. For this study, we used the LOS, intensity images with a cadence of 45 second, and the SHARP series *hmi.sharp_720s*. The full description of the data set is described in the following subsections.

HMI was designed to measure full disk LOS magnetic fields, Doppler shifts, continuum images and vector magnetic fields of the solar photosphere using the polarization of the sunlight. HMI has a 14 cm diameter refracting telescope coupled with a CCD of 4096×4096 pixels that represents a sampling of 0.504 arcsecs. This instrument captures the four Stokes parameters I, Q, U, and V using six narrowband filters with a bandpass of 76 mÅ at Full Width at Half Maximum (FWHM) along the 6173 Å Fe I absorption line (figure 4.2).

HMI has two similar cameras to perform spectropolarimetric measurements, i.e., they record the linear and circular polarization states of the sunlight. The so-called Doppler camera measures the spectral line velocities for both right- and left-circular polarization states. HMI

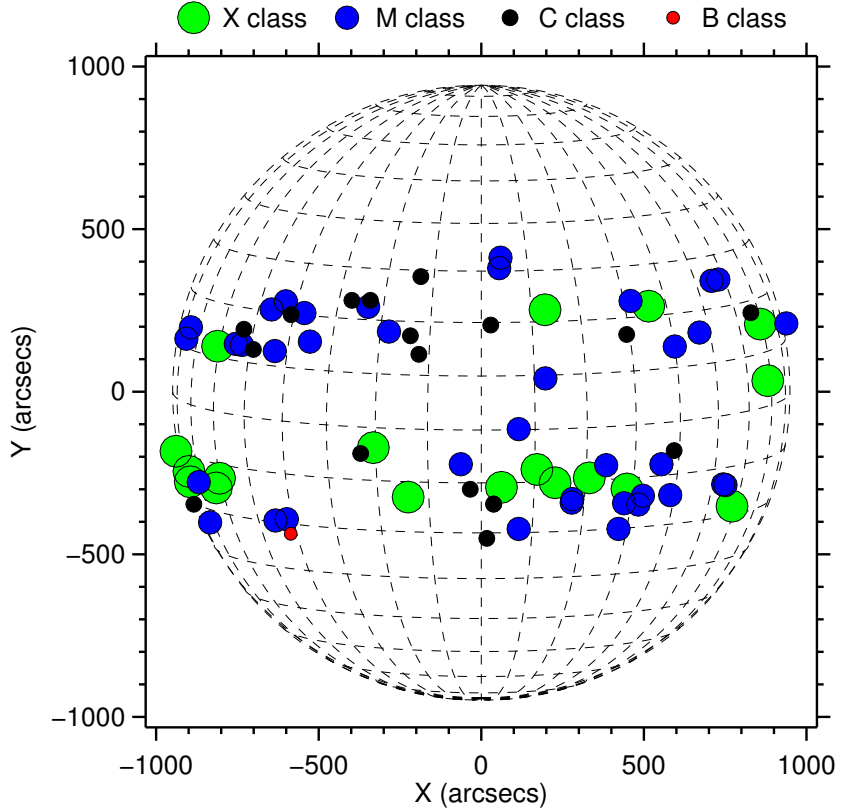


Figure 4.3: Positions on the solar disk of the selected 75 flares. The four colors and sizes of the circles represent the GOES classes: green (X-class), blue (M-class), black (C-class) and red (B-class). The dashed lines illustrate the heliographic longitudes and latitudes at every 10° .

4.2 Flare Sample

Flares with a wide energy range (small to extreme) and a wide range of heliographic longitudes (disk center to limb) were chosen for this study. We selected 75 solar flares of the current 24th solar cycle with GOES classes spanning from B to X. 43 events are based on the white-light flares (WLFs) catalog from Castellanos-Durán & Calvo-Mozo (2015). 32 events were added to expand the sample for the X-, C- and B-class events. The criteria for selection was that every event must have been simultaneously observed by both the SDO satellite and the Reuven Ramaty High Energy Solar Spectroscopic Imager (RHESSI, Lin et al. 2002) observed the event simultaneously. The resulting sample consists of 18 X-class, 37 M-class, 19 C-class and 1 B-class flares. Table 4.1 includes a full description of the dates, GOES start, peak and end times, GOES classes, NOAA active region numbers and flare coordinates (X and Y positions) in arcsecs with respect to image center. To permit to us the study of projection effects, there were no sample restrictions about the event position on the solar disk. The locations for the whole survey are shown in figure 4.3 where the circles illustrate the flare positions and the colors their GOES classes: green for X-class, blue for M-class, black for C-class and red for B-class flares.

Flare	Date	Start [UT]	End [UT]	Peak [UT]	Class	NOAA AR	X pos ["]	Y pos ["]	ΔB_{LOS}	WLF
FL01	2011/08/09	07:48:00	08:08:00	08:05:00	X6.9	11263	858	208	Yes	Yes
FL02	2014/02/25	00:39:00	01:03:00	00:49:00	X4.9	11990	-939	-183	Yes	Yes
FL03	2014/10/24	21:07:00	22:13:00	21:41:00	X3.1	12192	332	-265	Yes	Yes
FL04	2014/06/10	11:36:00	11:44:00	11:42:00	X2.2	12087	-899	-245	Yes	Yes
FL05	2011/02/15	01:44:00	02:06:00	01:56:00	X2.2	11158	171	-239	Yes	Yes
FL06	2015/03/11	16:11:00	16:29:00	16:22:00	X2.1	12297	-332	-172	Yes	Yes
FL07	2014/10/27	14:12:00	15:09:00	14:47:00	X2.0	12192	771	-352	Yes	Yes
FL08	2011/09/24	09:21:00	09:48:00	09:39:00	X1.9	11302	-811	140	Yes	Yes
FL09	2014/12/20	00:11:00	00:55:00	00:28:00	X1.8	12242	448	-299	Yes	Yes
FL10	2012/10/23	03:13:00	03:21:00	03:17:00	X1.8	11598	-805	-266	Yes	Yes
FL11	2014/10/22	14:02:00	14:50:00	14:28:00	X1.6	12192	-225	-324	Yes	Yes
FL12	2014/06/10	12:36:00	13:03:00	12:52:00	X1.5	12087	-895	-277	Yes	Yes
FL13	2011/03/09	23:13:00	23:29:00	23:23:00	X1.5	11166	196	252	Yes	Yes
FL14	2012/07/12	15:37:00	17:30:00	16:50:00	X1.4	11520	62	-294	Yes	No
FL15	2013/11/10	05:08:00	05:18:00	05:14:00	X1.1	11890	227	-280	Yes	Yes
FL16	2014/06/11	08:59:00	09:10:00	09:06:00	X1.0	12087	-815	-296	Yes	Yes
FL17	2014/03/29	17:35:00	17:54:00	17:48:00	X1.0	12017	515	263	Yes	Yes
FL18	2013/10/28	01:41:00	02:12:00	02:03:00	X1.0	11875	881	34	Yes	Yes
FL19	2011/07/30	02:04:00	02:12:00	02:09:00	M9.3	11261	-527	154	Yes	Yes
FL20	2011/09/08	15:32:00	15:52:00	15:46:00	M6.7	11283	595	139	Yes	Yes
FL21	2011/02/18	09:55:00	10:15:00	10:11:00	M6.6	11158	744	-285	Yes	Yes
FL22	2011/02/13	17:28:00	17:47:00	17:38:00	M6.6	11158	-63	-223	Yes	Yes
FL23	2013/12/31	21:45:00	22:20:00	21:58:00	M6.4	11936	554	-223	Yes	No
FL24	2012/03/09	03:22:00	04:18:00	03:53:00	M6.3	11429	55	380	Yes	No
FL25	2012/07/05	11:39:00	11:49:00	11:44:00	M6.1	11515	483	-347	Yes	Yes

Table 4.1: Flare sample description: date, GOES start, peak and end times, class, NOAA active region number and flare coordinates in arcsec. ΔB_{LOS} indicates whether the flare showed magnetic field changes and ‘WLF’ whether it was a white-light flare. To selected the WLFs, we running differences between consecutive images and checked those regions with white-light enhancement larger than 5σ of the non-flare intensity .

Flare	Date	Start [UT]	End [UT]	Peak [UT]	Class	NOAA AR	X pos ["]	Y pos ["]	ΔB_{LOS}	WLF
FL26	2011/09/24	20:29:00	20:42:00	20:36:00	M5.8	11302	-736	144	Yes	Yes
FL27	2012/05/10	04:11:00	04:23:00	04:18:00	M5.7	11476	-348	261	Yes	Yes
FL28	2012/07/04	09:47:00	09:57:00	09:55:00	M5.3	11515	280	-330	Yes	Yes
FL29	2014/02/04	03:57:00	04:06:00	04:00:00	M5.2	11967	115	-115	Yes	Yes
FL30	2012/07/05	03:25:00	03:39:00	03:36:00	M4.7	11515	439	-343	Yes	Yes
FL31	2011/03/14	19:30:00	19:54:00	19:52:00	M4.2	11169	708	341	Yes	Yes
FL32	2014/10/24	07:37:00	07:53:00	07:48:00	M4.0	12192	115	-422	Yes	Yes
FL33	2011/10/02	00:37:00	00:59:00	00:50:00	M3.9	11305	197	41	Yes	No
FL34	2011/09/24	17:19:00	17:31:00	17:25:00	M3.1	11302	-755	147	Yes	Yes
FL35	2011/09/24	19:09:00	19:41:00	19:21:00	M3.0	11302	-635	125	Yes	Yes
FL36	2010/10/16	19:07:00	19:15:00	19:12:00	M2.9	11112	422	-422	Yes	Yes
FL37	2011/09/09	06:01:00	06:17:00	06:09:00	M2.7	11283	671	182	Yes	Yes
FL38	2011/12/31	13:09:00	13:19:00	13:15:00	M2.4	11389	-633	-396	Yes	Yes
FL39	2012/06/29	09:13:00	09:22:00	09:20:00	M2.2	11513	-544	242	Yes	Yes
FL40	2011/12/29	13:40:00	14:01:00	13:50:00	M1.9	11389	-834	-402	Yes	No
FL41	2012/06/09	16:45:00	16:56:00	16:53:00	M1.8	11504	-869	-278	Yes	Yes
FL42	2012/06/30	18:26:00	18:34:00	18:32:00	M1.6	11513	-284	185	Yes	No
FL43	2012/07/06	08:17:00	08:27:00	08:23:00	M1.5	11515	581	-318	Yes	Yes
FL44	2011/12/31	16:16:00	16:34:00	16:26:00	M1.5	11389	-598	-392	Yes	Yes
FL45	2011/12/26	02:13:00	02:36:00	02:27:00	M1.5	11387	497	-320	No	No
FL46	2012/05/08	13:02:00	13:12:00	13:08:00	M1.4	11476	-645	253	Yes	Yes
FL47	2011/02/18	12:59:00	13:06:00	13:03:00	M1.4	11158	751	-287	Yes	Yes
FL48	2012/07/04	14:35:00	14:42:00	14:40:00	M1.3	11515	278	-341	Yes	Yes
FL49	2012/05/05	22:56:00	23:04:00	23:01:00	M1.3	11476	-907	163	Yes	Yes
FL50	2012/03/17	20:32:00	20:42:00	20:39:00	M1.3	11434	384	-226	Yes	Yes

Table 4.1: Flare sample description (continued)

Flare	Date	Start [UT]	End [UT]	Peak [UT]	Class	NOAA AR	X pos ["]	Y pos ["]	ΔB_{LOS}	WLF
FL51	2011/02/18	20:56:00	21:14:00	21:04:00	M1.3	11162	59	412	Yes	Yes
FL52	2012/05/06	01:12:00	01:20:00	01:18:00	M1.1	11476	-893	198	Yes	Yes
FL53	2011/11/05	11:10:00	11:42:00	11:21:00	M1.1	11339	-601	278	No	No
FL54	2011/09/22	09:53:00	10:09:00	10:00:00	M1.1	11295	729	345	Yes	Yes
FL55	2012/04/27	08:15:00	08:29:00	08:24:00	M1.0	11466	459	279	No	No
FL56	2011/03/15	00:18:00	00:24:00	00:22:00	M1.0	11169	938	210	—	—
FL57	2012/07/03	03:36:00	03:48:00	03:42:00	C9.9	11515	38	-345	No	No
FL58	2011/08/03	07:38:00	08:06:00	07:58:00	C8.7	11261	447	176	Yes	Yes
FL59	2011/08/08	22:00:00	22:20:00	22:09:00	C7.7	11263	829	243	Yes	Yes
FL60	2011/05/27	16:38:00	16:47:00	16:43:00	C5.6	11226	-884	-346	No	Yes
FL61	2011/10/20	15:33:00	15:45:00	15:39:00	C5.4	11324	-701	130	Yes	Yes
FL62	2011/12/05	15:14:00	15:20:00	15:18:00	C4.9	11363	38	-346	No	Yes
FL63	2011/11/22	03:59:00	04:07:00	04:04:00	C4.7	11356	-730	192	Yes	Yes
FL64	2011/12/21	04:48:00	04:59:00	04:55:00	C4.3	11382	-34	-300	No	No
FL65	2011/11/07	03:05:00	03:16:00	03:10:00	C3.5	11339	-341	281	Yes	Yes
FL66	2011/07/27	09:56:00	10:12:00	10:02:00	C3.0	11260	-585	237	Yes	No
FL67	2011/08/20	22:54:00	23:00:00	22:58:00	C2.9	11271	-192	115	No	Yes
FL68	2011/10/27	18:38:00	18:49:00	18:44:00	C2.6	11333	-218	172	No	No
FL69	2011/03/31	15:26:00	15:46:00	15:35:00	C2.6	11176	593	-181	No	No
FL70	2011/09/03	07:47:00	08:04:00	07:56:00	C2.4	11281	17	-451	No	No
FL71	2011/04/23	07:30:00	07:38:00	07:34:00	C2.4	11195	-371	-190	No	No
FL72	2011/08/01	12:33:00	12:45:00	12:40:00	C2.0	11261	29	205	No	No
FL73	2011/04/12	03:40:00	03:52:00	03:46:00	C1.7	11190	-398	281	No	No
FL74	2011/04/18	18:55:00	19:08:00	19:02:00	C1.5	11193	-186	354	No	No
FL75	2011/07/16	16:59:00	17:11:00	17:05:00	B6.2	11254	-586	-437	No	No

Table 4.1: Flare sample description (continued)

4.3 Methodology: Pipeline

An automatic *pipeline* is required to perform a statistical study of magnetic field changes for a large variety of flares without any restriction in class or position over the solar disk. For this project, the *pipeline* was developed as composed of independent modules controlled by Boolean tables. As input, the *pipeline* reads a table which organizes the required entries: date of the flare, GOES start, peak and end times, flare class, NOAA active region number, location of the flare and coordinates of the field of view (FoV). With this information each module is run following the steps in the flow diagram in figure 4.4.

The following subsections describe each module of the *pipeline*: the data (§4.3.1), time ranges (§4.3.2), FoV coordinates (§4.3.3), alignment between images (§4.3.4), fitting procedure (§4.3.5, §4.3.6), the approach to measure the amplitude of the magnetic field change (§4.3.7), and the conditions to distinguish between stepwise behavior and solar evolution (§4.3.8).

4.3.1 The Data

This survey of magnetic field changes used three data sets for the analysis: two from SDO/HMI to obtain the main results of the study, and one from SDO/AIA to derive a suitable FoV for each event that includes the different structures of the active region observed throughout the solar atmosphere. The three data sets are:

1. The SDO/HMI full disk LOS magnetic field (*hmi.M_45s*) and intensity images (*hmi.Ic_45s*) with a 45-second cadence and a spatial sampling of 0.504 arcsecs per pixel. Top-panels in figure 4.5 show a continuum image (left) and a magnetogram (right) of active region AR 11305.
2. We selected the SHARP series *hmi.sharp_720s*, which consists of the tree Cartesian components of the vector: the strength, the inclination with respect to the LOS, and the azimuth. This type of data has a 12-minute cadence and 0.504 arcsecs spatial sampling. SHARP data are described in CCD image coordinates as are the 45-second intensity images and magnetograms.

The inclination angle ranges from 0° to 180° . Zero degrees means the direction that points towards the observer, 180° points in the direction of the Sun, and at 90° degrees the field is perpendicular to the LOS direction. The azimuth angle takes values from 0° to 360° increasing counter-clockwise from the projected Sun's north. The ambiguity at 180° degrees of azimuth in SHARP data is

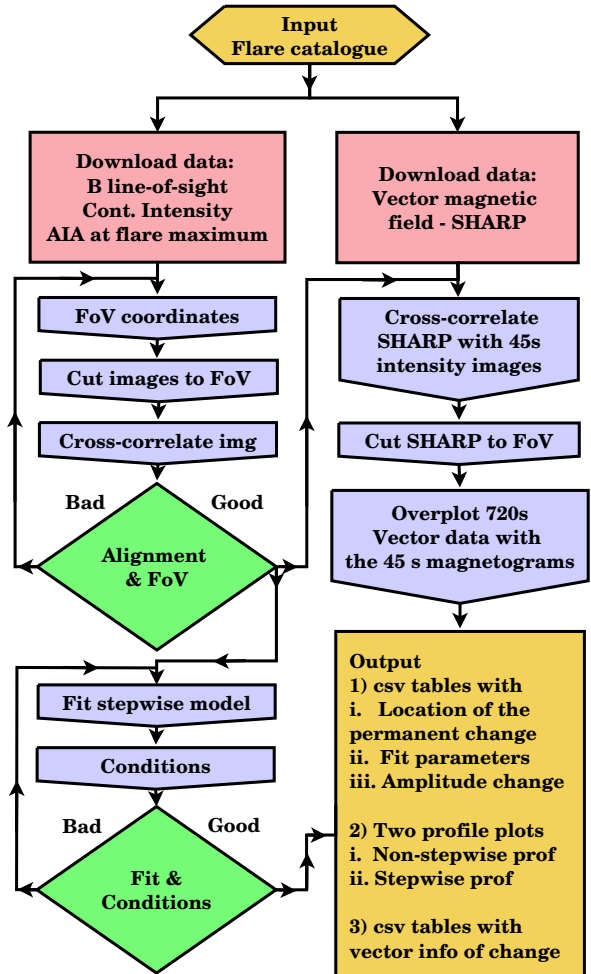


Figure 4.4: Pipeline flow diagram.

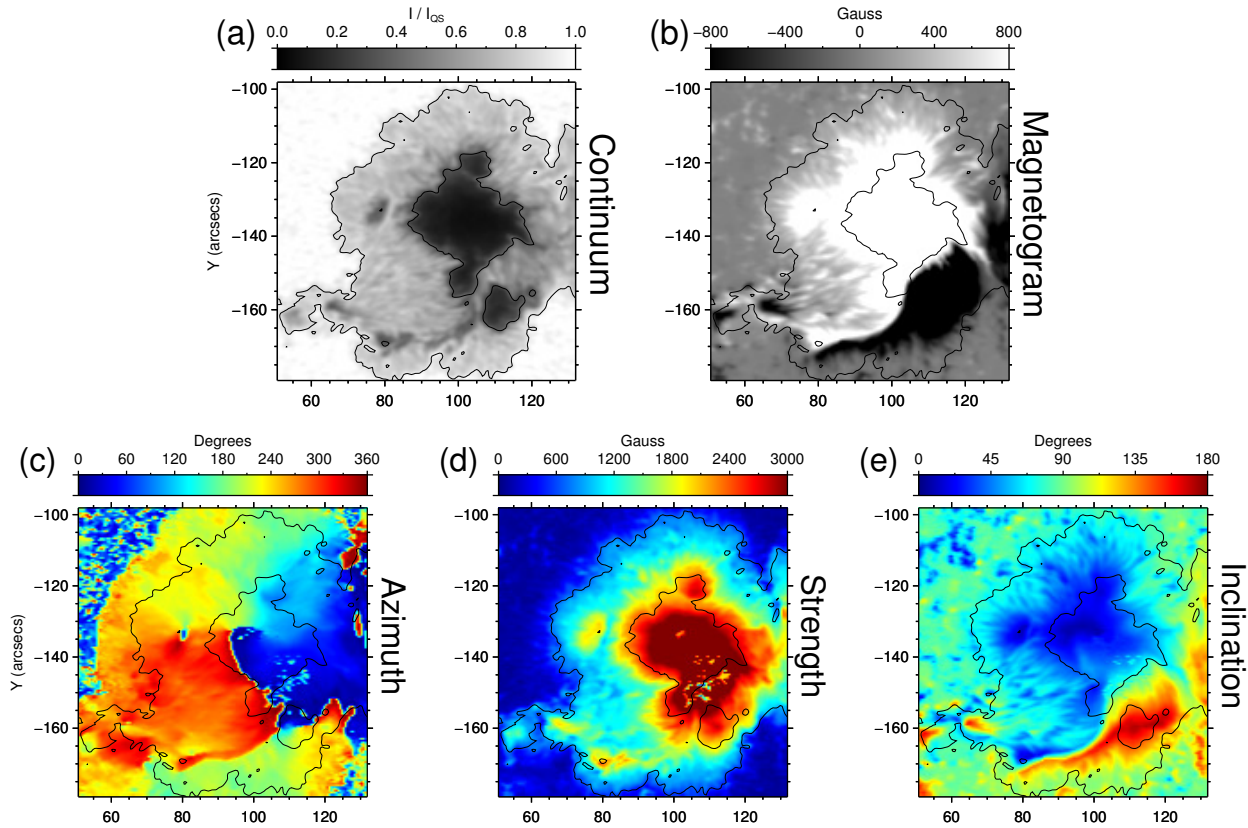


Figure 4.5: AR 11305 which produced an M5.2 flare (SOL2014–02–04T04:00). (a) intensity, (b) magnetogram. The three components of vector magnetic field: (c) azimuth, (d) strength of the field, and (e) inclination with respect to LOS component.

resolved using the minimum energy method (e.g. Metcalf 1994, Leka et al. 2009). The noise in the Stokes Q and U is larger for observations closer to the limb as the observations are. This implies that the magnetic strength values below 220 G of the pixels near the limb are considered to be noise. The bottom panels in figure 4.5 shows the three components of the magnetic field for AR 11305: azimuth (left), the strength of the field (middle), and inclination (right).

3. The eight SDO/AIA full disk images of the chromosphere, transition region, and corona with a 12-second mean cadence and a spatial sampling of 0.6 arcsecs. Three images per channel were downloaded around the peak of the flare time and the one with shortest exposure time was selected. These images were used to choose a suitable FoV containing all relevant magnetic structures (see §4.3.3).

4.3.2 Time Range

The solar photosphere evolves on different temporal scales: from seconds (granules and small magnetic structures) to days or even months (sunspot lifetimes). During long observing time intervals different processes may overlap with those associated with permanent magnetic field changes related to flares. We studied six different intervals to choose a suitable time range that accomplishes the requirements:

full observation of abrupt and permanent changes of the magnetic field, minimization of the non-flaring contributions, and the reduction of the amount of data storage that a statistical analysis requires. Eight hours were taken as the largest time interval while varying the cadence, as follows:

Interval I Four hours before flare until one hour before peak of the flare; the cadence between two consecutive images is ten minutes.

Interval II Two hours before peak of the flare until one hour after flare; the cadence is the maximum for the SDO/HMI instrument, i.e., one image every 45 seconds.

Interval III Same cadence as the interval (I) starting at the end of the interval (II) until four hours after the peak of the flare.

Six different time ranges were tested centered on the peak of the flare: 30 minutes, 1 hour, 90 minutes, 2 hours, 4 hours, and 8 hours following the cadence intervals described above. The time ranges were tested by fitting the Sudol & Harvey (2005) stepwise function (see below equation 4.1) to all LOS magnetic profiles and comparing the goodness-of-fit. The alignment of images during 8 hour or 4-hour intervals is not reliable. Tracking single pixels during such an amount of time is not possible, due to the evolution of the active region and the solar rotation. As a consequence, these intervals were discarded.

Figure 4.6 shows the evolution of the field in two different separated pixels in the FoV for a two-hour interval during the X1.0 solar flare SOL2014-03-29T17:48. Colored lines represent the fit for 120 minutes (blue), 90 minutes (green) and 60 minutes (red) time intervals. The 30 minute and 60 minute time ranges behave similarly; the solar evolution enables us to trace the variation of the magnetic field on single pixels. During the 30 and 60 minutes time intervals, some real permanent changes of the local magnetic field with a low rate of change (e.g. figure 4.6, right) are not clearly seen, for they need a longer time interval. During, the 2 hours and 90 minute intervals both, high and low rate changes are fully observed. We chose the 90-minute interval centered on the GOES peak time because it balances the required long duration interval to have sufficient data points of the twelve-minute cadence vector data, and it restricts the contributions of non-flaring solar evolution as much as possible.

4.3.3 Coordinates: Field of View

The observed flare sizes vary depending, for example, on the energy released (e.g. GOES class), the magnetic topology of the active region, and the location on the solar disk. We chose a suitable FoV manually because the location of each flare changes between catalogs. Furthermore, implementing an automatic procedure that takes into account the ample variety of sizes and shapes of flares in the survey is difficult and out of the scope of this work. Therefore, we used the intensity images from HMI and the AIA channels to look at the magnetic structures. The following steps were carried out to determine a suitable FoV

- I. Search the location of the flare in RHESSI, GOES and AIA catalogs. We obtained movies, images, and GOES light curves.
- II. Plot the HMI intensity images and all AIA channels with an FoV of 128×128 arcsecs² centered on the flare's coordinates given by either RHESSI or AIA catalogs, depending on the flare.

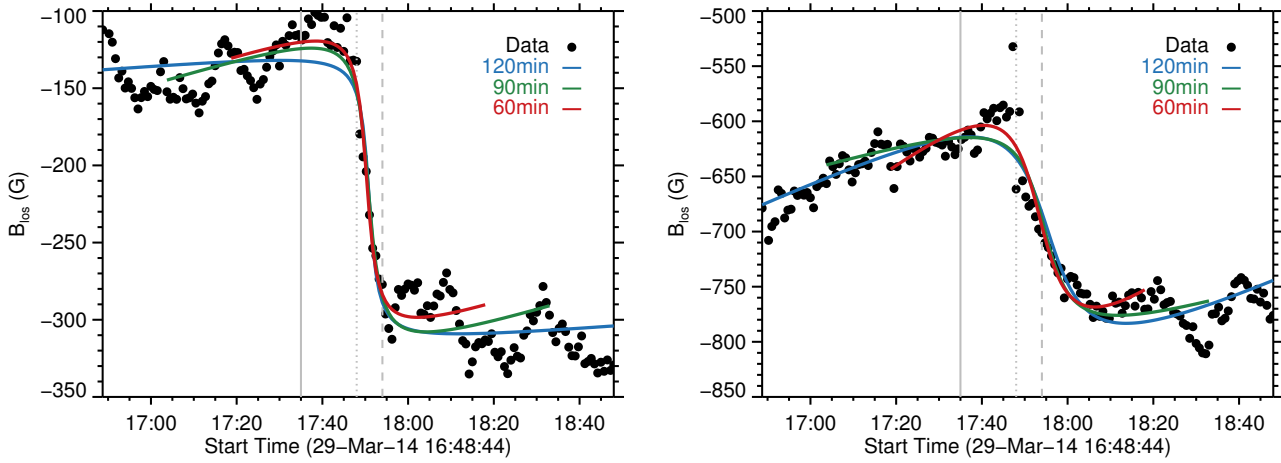


Figure 4.6: Magnetic evolution of two pixels during the X1.0 solar flare SOL2014-03-29T17:48 during a period of two hours (black dots). The blue, green and red lines are the best fit of the stepwise change for 2 hours, 90 minute and one-hour intervals, respectively.

- III. Verify each plot of the photospheric, chromospheric and coronal structures by eye (HMI continuum intensity and magnetogram, and all AIA channels).
- IV. Shift the center and change the size of the FoV to fit all the relevant structures observed at the peak of the flare, such as the active region, chromospheric emission, filaments, coronal loops and their footpoints. The size of each flare is different and therefore the FoVs in the sample ranges from 80×80 arcsecs 2 to 300×300 arcsecs 2 .

The last two steps (III and IV) were repeated many times, in some cases until an appropriate FoV was chosen for each flare. An example of the final FoV for the flare GOES M3.1 SOL2011-09-24-T17:20 is shown in figure 4.7, which shows (a) the continuum intensity, (b) the magnetogram, (c) the AIA images at 1600 Å, (d) 304 Å, (e) 211 Å, and (f) 193 Å. Note in panels (c) and (d) that the flare emission occurred in a compact region; however, the magnetic topology of the active region extends throughout the FoV.

4.3.4 Alignment

The Sun rotates with different rates depending on the latitude: faster close to the equator, and slower near the poles. This rotation makes that two consecutive HMI images are shifted between each other 0.08 arcsecs on average. The alignment of the 120 images taken during the 90-minute interval is a vital part of our *pipeline*, and the analysis in general, in order to be able to trace pixel-to-pixel variations. We did not set any restriction regarding solar rotation or evolution. We cross-correlated two images using a co-spatial sub-region in both images (test window) and measured how much an image has shifted compared to the other. In practice, one calculates the Fourier transform for both test windows, takes the complex conjugate of the second image and multiplies the two transforms. This multiplication in the Fourier space leads to a cross-correlation image containing information about the displacement between images. To carry out it, we used the SSWIDL `xyoff.pro` routine.

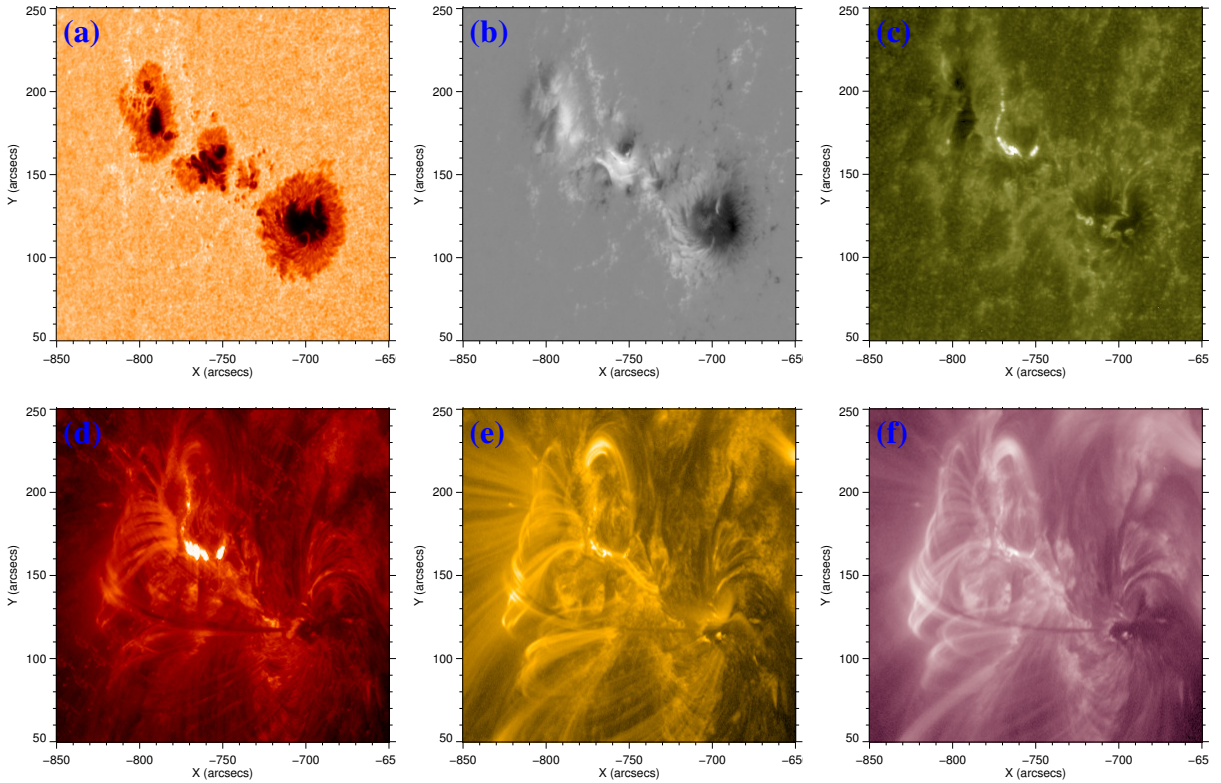


Figure 4.7: The panels show different layers of the solar atmosphere to determine the FoV for the event GOES M3.1 - SOL2011-09-24T17:20. (a) continuum intensity, (b) magnetogram, and the AIA channels at 1600 Å (c), 304 Å (d), 211 Å (e) and 193 Å (f).

In the *pipeline*, the continuum images are used for the alignment. In our procedure, we run the alignment method twice for each datacube to obtain a well-aligned set of consecutive images. For events located near the limb, it was necessary to find cross-correlation windows not containing the limb because the strong intensity gradient at the observed edge of the Sun makes the procedure fail.

It is also required to co-align the 12-minute vector data to the 45-second continuum images and magnetograms. The SHARP series `hmi.sharp_720s` also includes continuum images at each time step, and both datasets have the same 0.504 arcsecs sampling. We aligned each SHARP continuum image to the temporally closest 45-second continuum image.

4.3.5 Fitting Procedure

Previous studies (e.g. Petrie & Sudol 2010) have shown that permanent changes of the magnetic field related to the flare process may occur anywhere in the active region. Our aim here is to find the precise location of the non-transient changes in the temporal evolution of the magnetic field. Also, we need to avoid detecting only transient changes, which may arise from a failure of HMI's algorithm during flares. To deal with permanent changes of the magnetic field, we fitted the stepwise function from Sudol &

Harvey (2005) given by

$$B(t) = a + bt + c \left\{ 1 + \frac{2}{\pi} \tan^{-1}[n(t - t_0)] \right\}, \quad (4.1)$$

where the evolution of the field background is represented by a linear function with intercept (a) and slope (b). The stepwise evolution in time t is described by the half-amplitude of the field change (c), the midpoint of the abrupt field change (t_0), and the inverse of the timescale over which the field change occurs (n). The IDL MPFIT package (Markwardt 2009) solves the non-linear least square problem to fit a given model to a dataset, in this case, the stepwise model (equation 4.1).

4.3.6 Limits of Fitting Parameters

	Starting values	Units	Parameter space interval
a	Avg($B_{\text{LOS}}(t)$)	[G]	(-3001, 3001)
b	2.7	[G s^{-1}]	(-50, 50)
c	200	[G]	(-1000, 1000)
n	1.0	[s^{-1}]	(-500, 500)
t_0	45	[min]	($t_{\text{str}} - 5\text{min}$, $t_{\text{end}} + 5\text{min}$)

Table 4.2: Starting values and limits of fitting parameters for the fit procedure. t_{str} and t_{end} are GOES start and end times respectively.

The non-linear least-squares procedure requires starting values for the parameters to fit the stepwise model. This procedure minimizes the χ^2 to fit each magnetic field evolution; however, in some cases the minimization algorithm may end up in a local minimum if the parameter spaces are not well chosen. Furthermore, the procedure works faster when having smaller limits for the parameters. In our case, that is important because we are fitting three billion data points. We tested eighteen parameter spaces ranging from the widest cases to very narrow ones. The stable results are summarized in table 4.2.

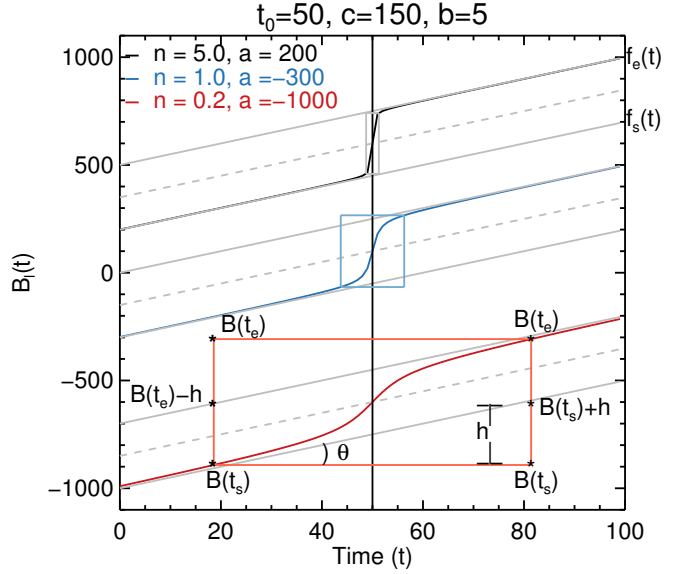


Figure 4.8: Geometrical approach to solve the degeneracy between parameters b and n .

4.3.7 Size of the Step

The abrupt and permanent variations of the magnetic field do not always follow a stepwise behavior (see §5.2). Although previous authors (e.g. Sudol & Harvey 2005, Petrie & Sudol 2010), measured the amplitude of the permanent change assuming a stepwise model (hereafter SH-model) and fitting it to the magnetic profiles. The SH-model implies that the amplitude of change is given by $\Delta B_{\text{stepwise}} = 2c$ (see equation 4.1). As the slope of the background and duration of change increase, the value of the change's amplitude retrieved using the parameter c from the SH-model model differs from the real size of the permanent change. Figure 4.9 shows the behavior of the stepwise model when varying (i) the slope of the background and (ii) the duration of the change, for a theoretical case with a

time range of 100 minutes, a step-size parameter c set to 150 Gauss, and the stepwise change occurring at the center of the working time interval (50 min). A real example magnetic profile which occurred during the flare SOL2010-10-16T19:12 is shown in the bottom panels (*iii* – *iv*).

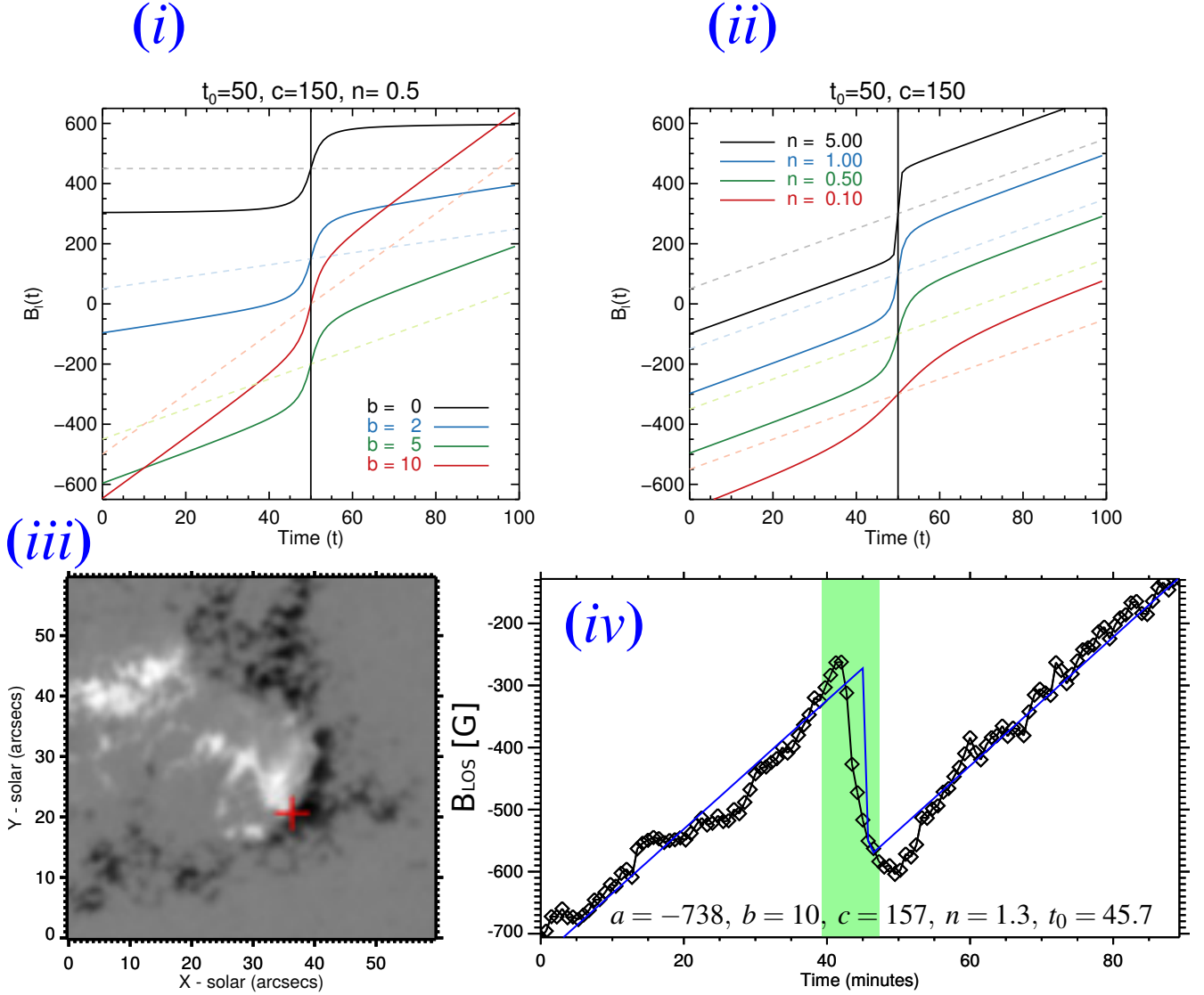


Figure 4.9: Panels (*i* – *ii*) show the behavior of the stepwise function with fixed parameters c and t_0 , and varying the slope of the background b from 0 to 10 (*i*) or the inverse of the step duration n^{-1} from 0.1 to 5 (*ii*). The panel on the bottom-right shows a real magnetic profile when the slope of the background is greater than zero and the inverse of the duration of the change n is greater than 1. Magnetogram (*iii*) of AR 11112; the red cross points to the location of the profile during the M2.9 flare SOL2010-10-16T19:12 shown in (*iv*).

Measuring the amplitude of the permanent change with the SH-model method cannot be used in all cases, but other concepts are required to compute the amplitude of the permanent change. A second approach based on the fact that permanent changes are observed to be co-temporal to the flare process. In this case, the amplitude is calculated by taking the difference between the maximum and minimum values before and after the change starts, in an interval no longer than 20 minutes from the peak of the flare.

The second method fails in cases when the slope of the background is high or when HMI's algorithm fails near the peak of the flare due to changes in the shape of the absorption line profile. For instance, the Fe I spectral line at 6173 Å may be Doppler-shifted or may take a non-Gaussian shape, or may go into emission (e.g. Ding et al. 2002, Qiu & Gary 2003). In these cases, the values from HMI's reconstruction algorithm show artifacts, such as: wrong sign of the field or transient jumps of a few thousand Gauss. These artifacts are produced because the model used to interpret the Stokes profiles is not correct. Figure 4.10 shows four examples where the HMI-algorithm failed during flares. A flare near disk center is shown in the top panel, while middle and bottom panels depict flares closer to the limb. The red line shows white-light (WL) emission.

The third approach to measure the amplitude of the permanent change is based on geometrical assumptions from the stepwise function (see figure 4.8). Let us define the start (t_s) and end (t_e) times as

$$t_s = t_0 - \frac{2\pi}{n}, \quad t_e = t_0 + \frac{2\pi}{n}. \quad (4.2)$$

The inclination angle θ of the stepwise model is given by

$$\theta = \tan^{-1} \left(\frac{y}{x} \right) = \tan^{-1}(b). \quad (4.3)$$

The difference in height h is written as

$$h = (t_e - t_s) \tan \theta = 4\pi \frac{b}{n}. \quad (4.4)$$

The equations of the $f_s(t)$ and $f_e(t)$ lines that intercept the stepwise function $B(t)$ at the start ($B(t_s)$) and end ($B(t_e)$) times are given by

$$\begin{aligned} f_s(t) &= \left(\frac{h}{t_e - t_s} \right) (t - t_e) + B(t_e), \\ f_e(t) &= \left(\frac{h}{t_e - t_s} \right) (t - t_e) + B(t_s) + h. \end{aligned} \quad (4.5)$$

The amplitude of the permanent change in the third method is the difference between the intercepts of the equations (4.5) which gives us

$$\Delta B'_{\text{Step}} = B(t_e) - B(t_s) - 4\pi \frac{b}{n}. \quad (4.6)$$

This third approximation assumes a perfect stepwise change which, for observational data, might not be the case. To summarize, there are three approaches to measure the amplitude of the permanent change: (i) from the c parameter of the SH-model, (ii) taking the difference between the maximum and the minimum in a temporal range near the peak of the flare, (iii) from the geometrical correction. Figure 4.11 shows three examples in which at least one of three methods failed measuring the amplitude of the change. We decided to apply the three methods to all profiles and, to select the smallest value given by the three methods.

4.3.8 Conditions

After the fitting, conditions for the exclusion of certain profiles must be specified to distinguish magnetic profiles of permanent changes from those due to normal solar evolution. These conditions must

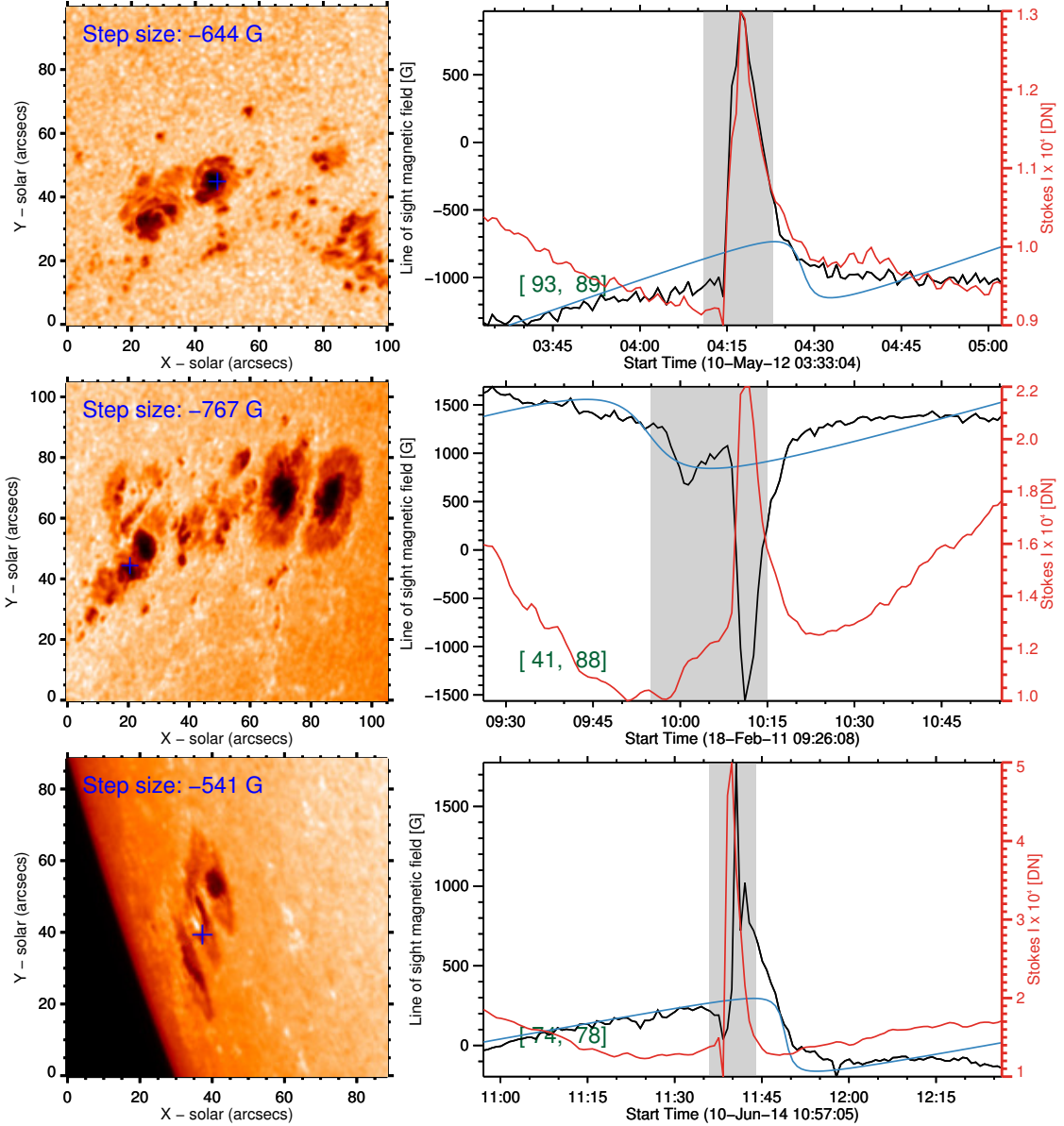


Figure 4.10: Extreme cases where the HMI's algorithm fails due to changes on the Fe I absorption line during the flares M5.7 - (SOL2012-05-10T04:18, top), M6.6 - (SOL2011-02-18T10:11, middle), X2.2 - (SOL2014-06-10T11:42, bottom). Each panel shows real examples of intensity (red) and LOS magnetic field (black) lightcurves. The blue line shows the stepwise function best fit. The images on the left show the active region, where the blue crosses point to the location of the lightcurves plotted on the right. The gray shade represents the duration of the flare.

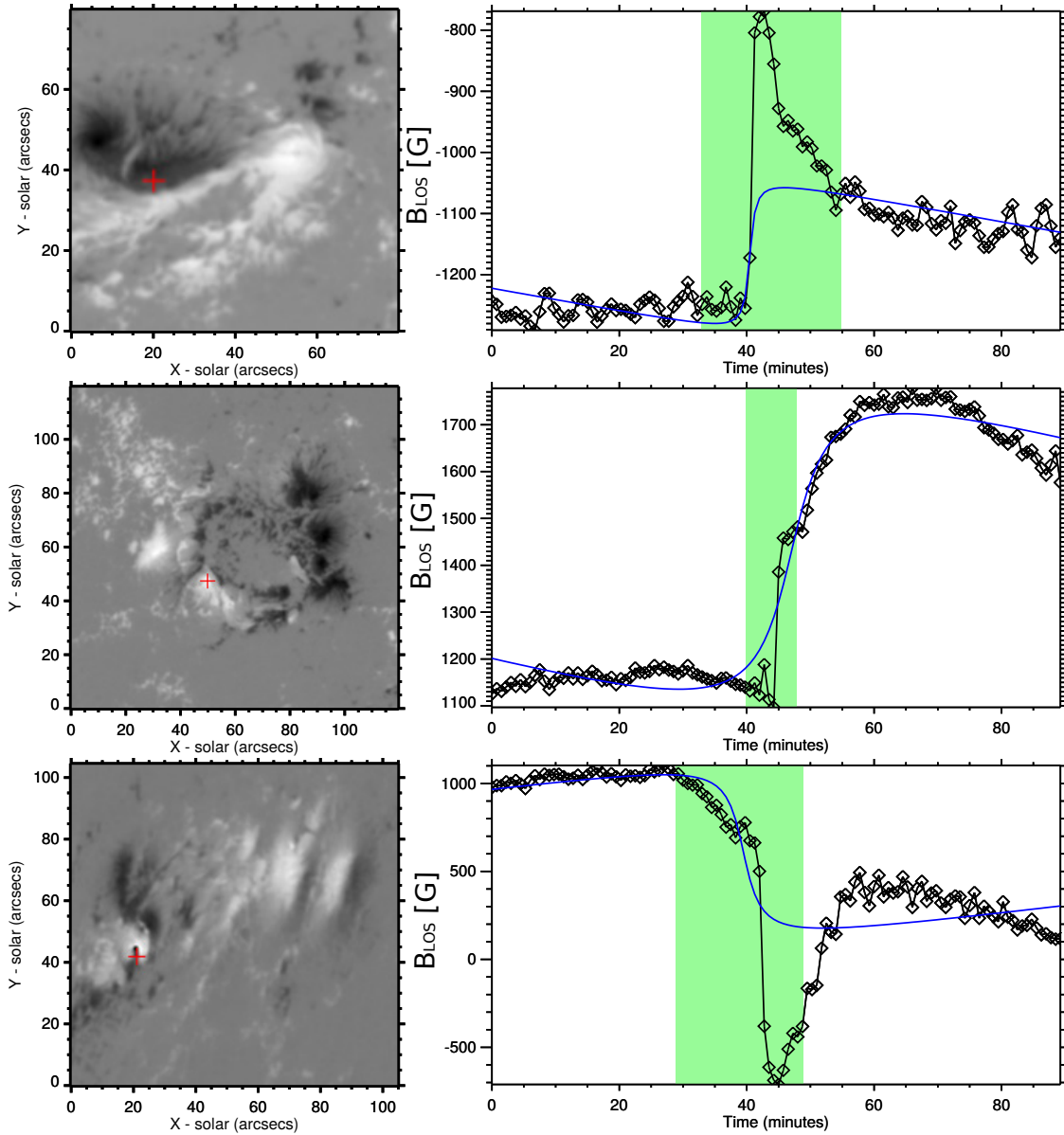


Figure 4.11: Three extreme cases to measure the amplitude change during the events X2.2 - SOL2011-02-15T01:56, M9.3 - SOL2011-07-30T02:09 and M6.6 - SOL2011-02-18T10:11, respectively. Each panel shows real examples in which approaches to measure the amplitude of change failed. The gray-scaled image on the left shows the active region, where the red cross points to the location of the magnetic profile plotted on the right with black diamonds. The blue line represents the best-fit and green intervals show the GOES flare duration.

automatically identify flare-related changes due to the large number of profiles involved in the study. A rough calculation shows that the number of data points in this statistical analysis are

$$\underbrace{400 \times 400}_{\text{pixels}} \times \underbrace{75}_{\text{events}} \times (\underbrace{120 \times 2}_{\text{BLOS + intensity}} + \underbrace{8 \times 3}_{\text{vector data}}) \simeq 3.2 \times 10^9, \quad (4.7)$$

grouped in $\sim 6 \times 10^7$ profiles. The majority of the magnetic curves show solar evolution or small variations above non-flaring regions, and for this reason they must be rejected from our analysis. Permanent changes are not all described by the stepwise model, because there is a broad diversity on the type of such changes. Therefore, we need conditions to select all the classes of permanent changes, and exclude the non-permanent changes of the magnetic field.

During our the first approach, we searched for permanent changes during the well-studied X class flare SOL2014-03-29T17:48 (e.g. Kleint et al. 2015, 2016). We looked for conditions that restrict the five parameters of the SH-model from having physical meaning. The sets of conditions was checked by comparing profiles associated to permanent changes with profiles of transient changes. In total, we obtained a few tens of thousand plots of magnetic profiles. However, these conditions do not apply to certain type of flares, particularly those events with relatively long impulsive phases.

We selected out from our sample five flares which showed permanent changes; we tried to generalize the conditions found previously for the X1.0 flare. The five flare events were chosen based on (1) the number of profiles showing permanent changes were discarded by the conditions, and (2) the number of non-flaring profiles were classified by the conditions as permanent changes. The five flares were ranked from excellent to noisy as how the first conditions behaved adding or eliminating flare-related or nonflare-related profiles. We ended up with the conditions we summarize in table 4.3.

	Condition		Condition
I.	$\Delta B_{\text{LOS}} > 80 \text{ G}$	VIII.	$ b \geq 10 \text{ and } n < 1$
II.	$t_0 + \frac{\pi}{2n} \geq t_{\text{end}}$	IX.	The profile passes the reduced- χ^2 test
III	$t_0 - \frac{\pi}{2n} \leq t_{\text{start}}$	X.	$ b > 1 \text{ and } \chi^2 > 30$
IV	$\eta \geq \Delta B_{\text{LOS}} $	XI.	$ b \geq 2 \text{ and } n < 0.5 \text{ and } \chi^2 > 20$
V	$\eta_{\text{non-flare}} \geq \Delta B_{\text{LOS}} /2$	XII.	$ b \geq 6 \text{ and } n < 0.5$
VI	$\eta_{\text{line}} < \eta$	XIII.	$ b \geq 3 \text{ and } 2\sigma < \Delta B_{\text{LOS}} \text{ and } \chi^2 > 10$
VII.	$ b > 20$	XIV.	Single pixels inside a 5×5 box are excluded.

Table 4.3: Pipeline conditions. The η , χ^2 and σ parameters are defined in equation 4.7. The sub-index line in condition 7 stands for a linear model, and $t_{\text{end}} = 90$ minutes and $t_{\text{start}} = 0$ minutes are the time range limits. ΔB_{LOS} are the amplitude of the permanent changes in the LOS component of the magnetic field. The nomenclature of the parameters σ , η , and, χ^2 is defined as: $\sigma = \sqrt{\frac{1}{n-1} \sum (y - \bar{y})^2}$, $\eta = \sqrt{\frac{1}{n-1} \sum (y - y_{\text{model}})^2}$, $\chi^2 = \frac{\sum (y - y_{\text{model}})^2}{\sigma}$.

Put into words, these conditions represent the following: the size of the changes shall be larger than 80 G (I). The change shall finish in a 90-minutes time range (II-III). The standard deviation of the data from the stepwise model shall be less than the size of the change during the full interval, and less than half of the amplitude before and after the flare (IV-V). The time series shall be better fit by the stepwise model than a lineal model (VI). The profile shall pass the reduced- χ^2 test (Greenwood & Nikulin 1996) (IX). The ratio, presented the slope of the background and the inverse of the change is less than $b/n = 10/1, 6/0.5$, and $b/n = 2/0.5$ if the $\chi^2 > 20$ (X-XIII). Single pixels inside square box with size equal to 5×5 pixels are rejected (XIV).

The conditions shown above were satisfied by 131 thousand pixels for the entire sample. However, the conditions also excluded permanent changes. We checked all profiles with an amplitude of change larger than 80 Gauss manually ($\sim 1.2 \times 10^6$) to eliminate false signatures using a Boolean GUI, i.e., it assigns 1 if the user considers the profile a permanent change, and 0 in the opposite case. The first run was organized by dividing the FoV in 50×50 pixels grids, and adding or eliminating pixels in each sub box. A second completely random run eliminated any kind of inconsistency bias by the user. The difference between the two runs was less than the 5%.

Chapter 5

Permanent Changes in the Line-of-Sight Component of the Magnetic Field

In this chapter, we present the observational results of the LOS component of the magnetic field (magnetograms) and continuum images. We discuss the morphology of the permanent changes, their location above the active region and their positions with respect to the PIL. We also discuss the spatial relation between the WL emission and abrupt changes of the magnetic fields. We conclude with statistics about the permanent changes in the LOS components of the magnetic field for the entire sample of flares.

Figure 5.1 illustrates an example of our results for an X-class event (SOL2012-10-23T03:17). The flare occurred in an active region that had coordinates S19° E62°. The top panels (a-b) show the intensity and the magnetogram images of the AR 11598, where the gray boxes enclose the location of the flare. During this event, a substantial continuum enhancement was observed before the GOES maximum. Panel (c) shows the WL kernels at the peak of the WL emission. We obtained the WL kernels by taking the difference of the image closest to the maximum of the WL emission minus a pre-flare image. The WL image is reversed in intensity for clarity.

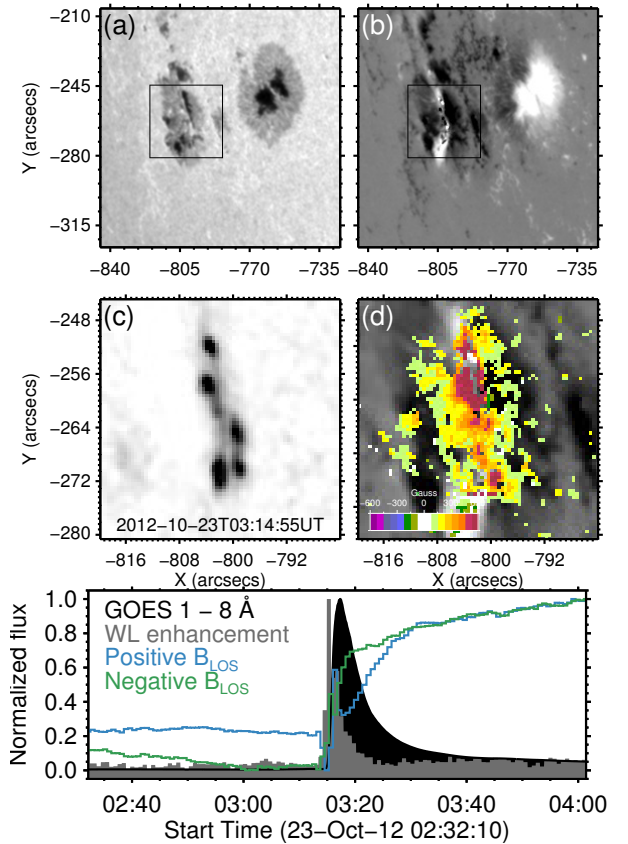


Figure 5.1: (a) intensity, (b) LOS magnetic field maps during the X1.8 solar flare SOL2012-10-23T03:17. Zoomed images of the gray boxes in panels (a-b) show the WL emission in reversed colortable (c), and amplitude of the permanent changes of the magnetic field (d). The bottom panel illustrates the normalized temporal evolution of the GOES 1 - 8 Å SXR (black), the WL enhancement (gray), the total positive (blue) and negative (green) magnetic field flux inside the zoomed FoV.

Permanent changes in the LOS component of the magnetic field (ΔB_{LOS}) were observed during this event as well. The ΔB_{LOS} are located in a compact kernel with a projected area $\sim 321 \text{ Mm}^2$, and the total unsigned change of the field was 283 Mx cm^{-2} . Panel (d) in figure 5.1 shows the locations of ΔB_{LOS} indicated as colored pixels. The scale ranges from -600 G to 600 G. The ΔB_{LOS} are located close to the PIL, and the strongest changes are located close to this line (blue and red pixels). The locations of the WL enhancement and ΔB_{LOS} mostly overlap, although they do not have a one-to-one spatial relation.

The bottom panel in figure 5.1 shows the temporal evolution of the thermal emission in the 1 - 8 Å GOES band (black shade), the WL enhancement (gray shade), the positive (blue) and negative (green) polarities of the LOS component inside region (d). Both positive and negative polarities permanently change from before to after the flare process. The enhancement in WL and the variation of the LOS field were observed before the emission in the GOES thermal band, and it was co-temporal with the permanent variations of the field.

Hereafter, the nomenclature FL plus the number (as in table 4.1) is used when flares are cited. Besides, to avoid confusion when we refer to the intensity images from the HMI instrument, we use the terms *continuum*, *white-light*, *Stokes I* and *intensity images* as synonyms. There are physical differences in the definition for each of these terms; however, taking into account the nature of the HMI measurements, we think it is legitimate to use them as synonyms without losing generality. The *LOS* and the *longitudinal* components are used as synonyms of each other as well.

5.1 Evolution of the Active Region

If the magnetic field changes irreversibly, one might expect variations in the sunspot itself. For example, a small sunspot has been observed to completely disappear within 60-minutes co-temporally with an M2.4 flare (Wang et al. 2002a). The appearing or disappearing parts of penumbra or changes in the morphology of the sunspots are tracked by comparing iso-intensity and iso-magnetic contours before, during and after the flare. The iso-intensity curves are drawn following the edges of the penumbra and umbra. The magnetic contours are selected at 300 G and 1200 G. We plot the lightcurves of those regions where changes in the shape were observed. When intensity gradients are found, we conclude that the active region changes its shape. We did not study self-movements of the sunspot or pores around the active regions.

How are the changes of the sunspot? Figure 5.2 shows an example of morphologic changes of the penumbra and PIL in AR 11890. The left column shows the magnetograms and right column shows intensity images 10-minutes before, at peak of the flare, and 20-minutes after the X1.1 flare (SOL2013-11-10T05:14). Contours on the magnetograms represent 300 G and 1200 G. Contours on the intensity images follow the edges of the penumbra and umbra. The red arrow points to one of the regions where part of the penumbra disappear before the flare (red lines) and after the flare (blue lines). The umbra of the same spot increased its area (pink arrow). These types of changes in the shape of the active region begin to be noticeable after the peak of the flare; therefore we conclude that morphologic variations in the active region are a consequence of the eruption process. The study of the dynamics of pores (blue arrow) is out of the scope of this thesis.

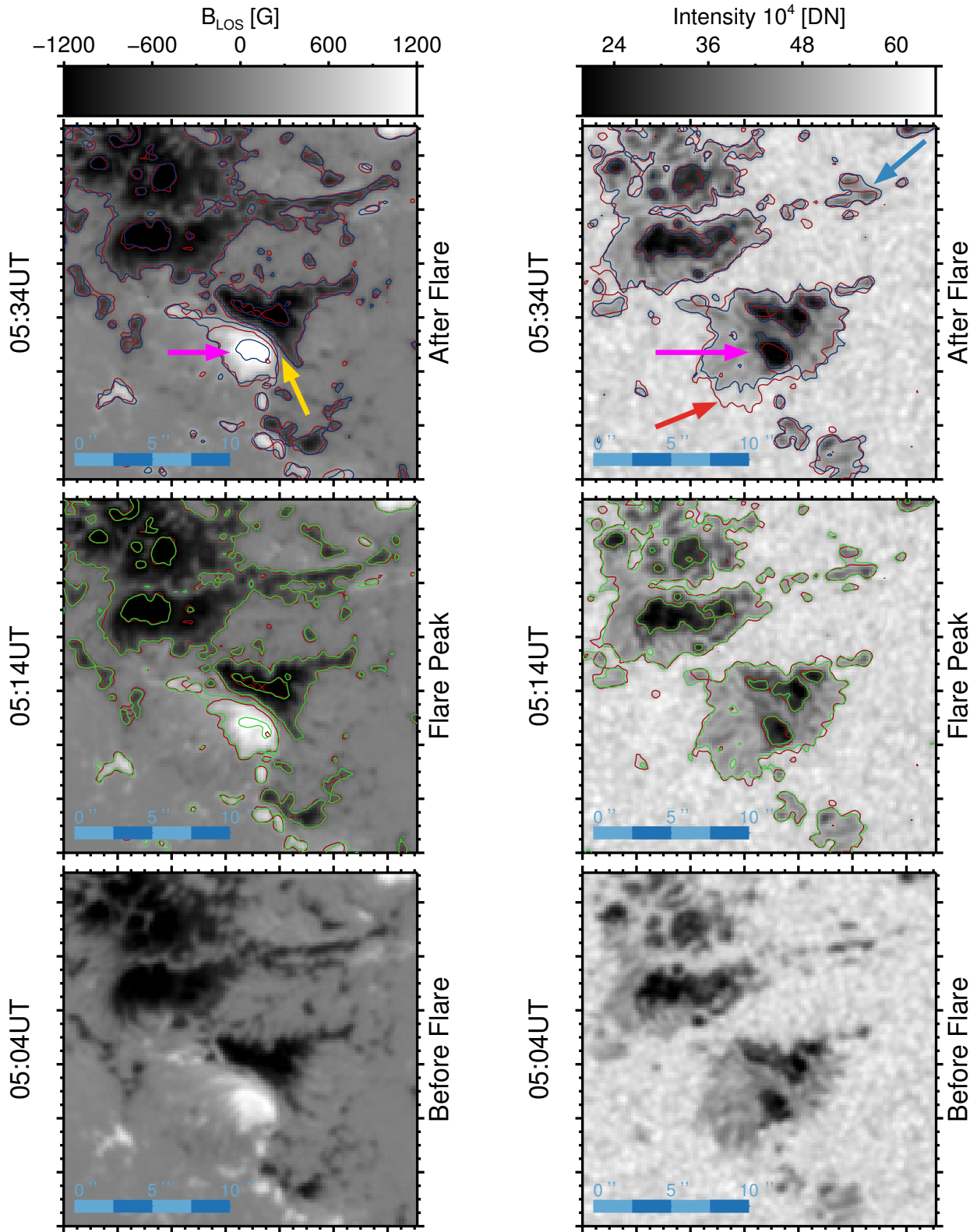


Figure 5.2: Evolution of AR 11890 during the X1.1 flare (SOL2013-11-10T05:14). The left column shows the magnetograms and the right column shows the intensity images at 04:29UT (before flare, bottom panels), 05:14UT (closest HMI-image to peak of the flare, middle panels), and 05:58UT (after flare, top panels). The iso-magnetic curves over the magnetograms represent 300 G and 1200 G. Contours drawn over the intensity images outline the edges of the umbra and penumbra. The red, green and blue colors of the contours illustrate how the active region looked before, at the peak of the flare, and after the flare, respectively. This figure shows an example of how the flare process changes the morphology of the active region.

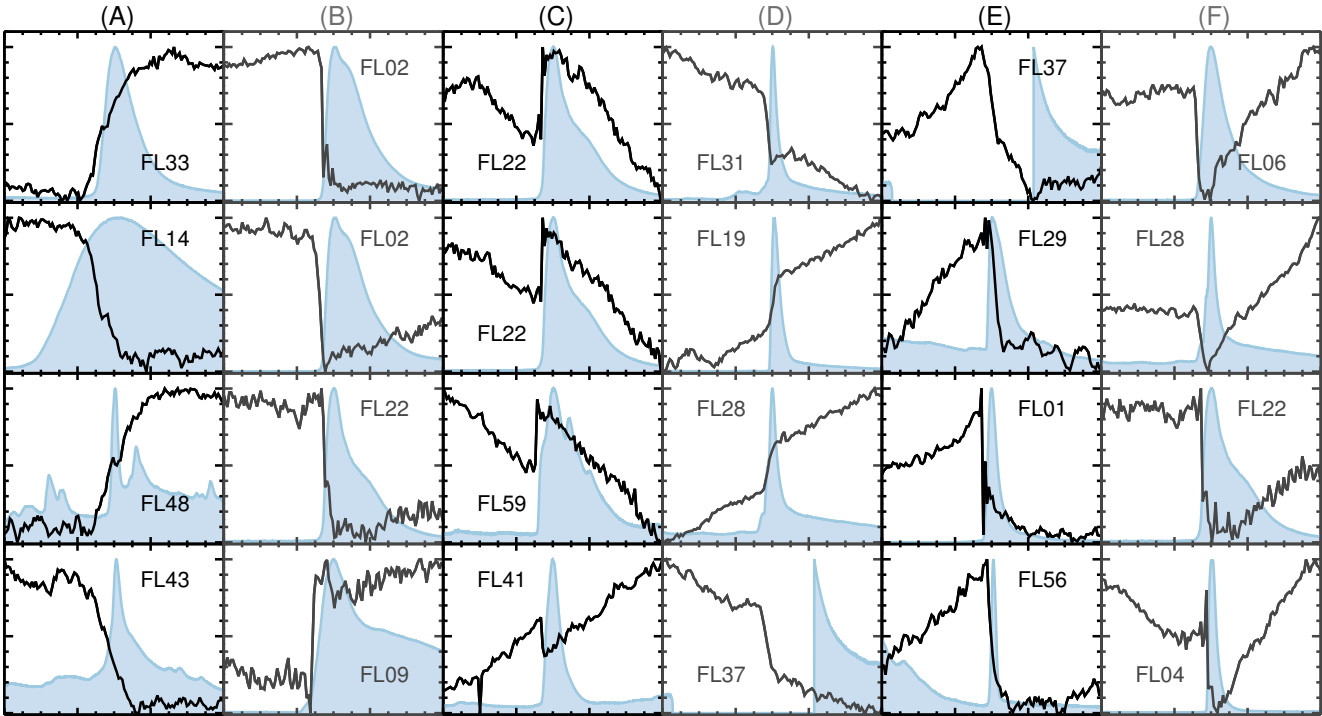


Figure 5.3: Morphologic classification of permanent changes, as found in our 75-flare sample. Each column presents four examples for each category, where the x -axis ranges 0 to 90 minutes centered at the peak of the flare, and the y -axis has its own limits for each profile. The blue shade is the normalized GOES 1 - 8 Å lightcurve. Each label represents the number of the flare in our catalog as appears in table 4.1.

For the entire sample, we found that parts of the penumbra near the location of the flare disappeared during 15 events¹. New patches of the penumbra that appeared at the same time as the flare were observed during 8 events². Different authors have also found motions of the PIL that are co-temporal with ΔB_{LOS} (e.g. Kosovichev & Zharkova 2001, Burtseva et al. 2015). During the X1.1 (SOL2013-11-10T05:14) and M2.9 (SOL2010-10-16T19:12) flares, motions of the PIL associated with the flare were observed (e.g. yellow arrow in figure 5.2).

5.2 Morphology of the Changes

A large number of permanent ΔB_{LOS} are well described by a stepwise function (equation 4.1), but we have found other types of permanent changes ΔB_{LOS} in our 75-flare sample that may not be well described by the SH-model. The entire variety of permanent changes is fully described below by twelve types of profiles. Figures 5.3 and 5.4 show a classification of the changes that we have found, where each row has four examples for each category. We selected profile examples from the entire sample. Different pixels in a given active region can behave differently and are therefore classified within different classes. The twelve (A)-(H) classes are:

¹Flares during which the area of the sunspot reduced: FL2, FL3, FL6, FL10, FL13, FL16, FL17, FL24, FL25, FL28, FL31, FL32, FL51, FL57, FL62.

²Flares during which the area of the sunspot increased: FL5, FL9, FL20, FL22, FL36, FL50, FL66, FL72.

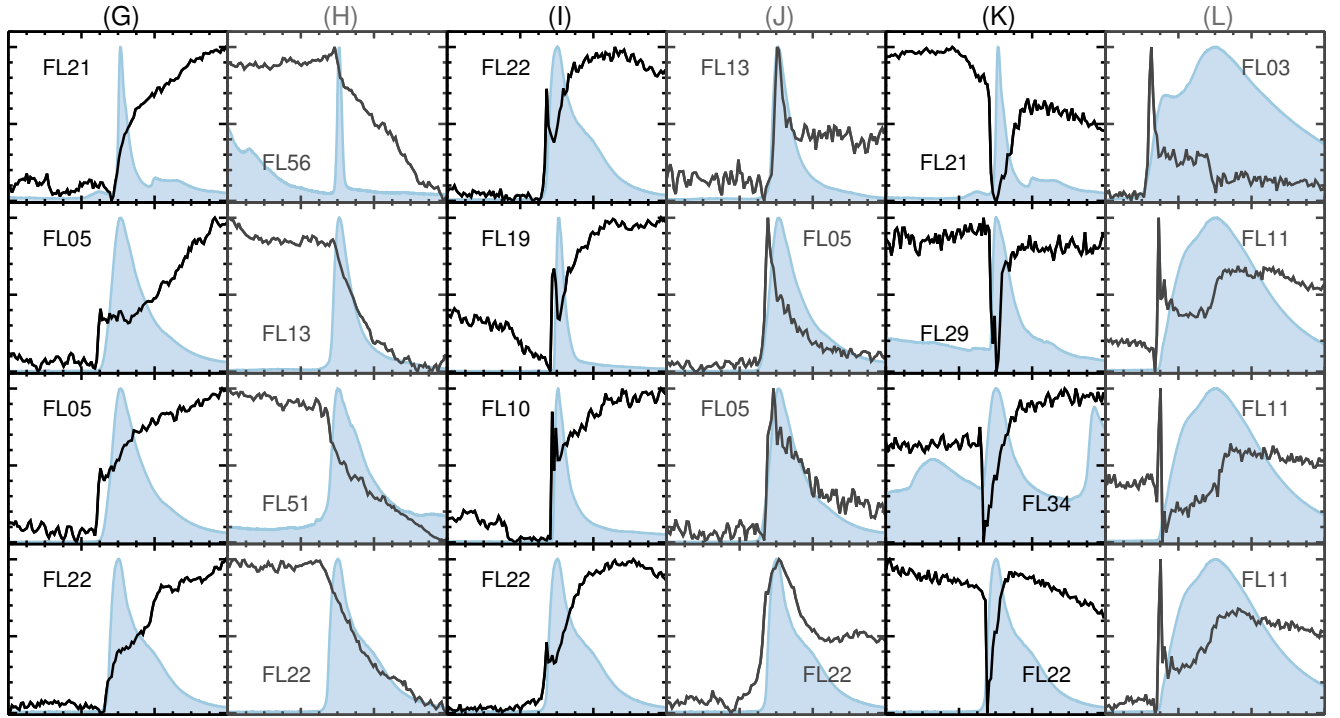


Figure 5.4: Morphologic classification of permanent changes, as found in our 75-flare sample. Each column presents four examples for each category, where the x -axis ranges 0 to 90 minutes centered at the peak of the flare, and the y -axis has its own limits for each profile. The blue shade is the normalized GOES 1 - 8 Å lightcurve. Each label represents the number of the flare in our catalog as appears in table 4.1.

- (A) Stepwise profile with a low rate of change between start and end values. On average, this type of change has a duration between three to fifteen minutes. The behavior of the field strength before and after the change does not vary much from an average value. In the majority of the cases, the polarity does not change during the entire interval, but we observed a sign change during the stepwise change in a few cases. This type of change has been also found by e.g. Sudol & Harvey (2005), Petrie & Sudol (2010), Petrie (2012), Petrie (2013), Wang & Liu (2010), Wang et al. (2012), Kosovichev & Zharkova (2001), Chen et al. (2007).
- (B) Stepwise profile with a high rate of change between start and end values. The duration of the change ranges between three minutes to forty-five seconds, i.e., the lower limit is set by the cadence of the instrument. Before and after the abrupt change, the field strength is almost constant. This type of change has been also found by e.g. Sudol & Harvey (2005), Petrie & Sudol (2010), Wang & Liu (2010), Wang et al. (2012), Chen et al. (2007).
- (C) The field strength before and after the flare varies linearly and with a slope of the same sign. The change occurs suddenly and the field crosses the value it already had before the change. This type of change has also been found by Sudol & Harvey (2005).
- (D) The field strength before and after the change varies linearly and with a slope of the same sign. The change occurs abruptly.
- (E) The field strength varies linearly until an abrupt change occurs and afterwards it remains almost constant. This type of change has been also found by Kosovichev & Zharkova (2001).

- (F) The field strength is constant just before a sudden negative change and after that change it varies linearly with a positive slope.
- (G) The field strength is constant just before a sudden positive change and after that change it varies linearly with a positive slope. This type of behavior could be due to flux emergence or cancellation.
- (H) The field strength is constant until a sudden change to a linear negative slope with a low rate of change.
- (I) The field strength is constant just before a sudden positive change. The field peaks in a short time and then it increases again. The change ends with the field strength almost constant at higher values than the short peak. This kind of profile is not fully described by a stepwise function. The amplitude of this type of the change is usually greater than 300 G.
- (J) The field strength is constant until a sudden positive change; then it shows a slow decay phase until the field strength reaches a constant value higher than the value before the change. The peak co-temporal to the maximum of the flare can be a misbehavior of the HMI-algorithm due to Doppler shifts or to changes in the shape of the Fe I line during the flare (e.g. Qiu & Gary 2003, Ding et al. 2002).
- (K) The main feature of this profile is that it shows a strong minimum pattern that is well correlated with the maximum of the flare. The strength of the field is constant with different values before and after the flare. This type of change has also been found by e.g. Burtseva et al. (2015), Sudol & Harvey (2005), Petrie & Sudol (2010), Kosovichev & Zharkova (2001), Chen et al. (2007). The strong minimum can also be a misbehavior of the HMI-algorithm due to Doppler shifts or to changes in the shape of the Fe I line during the flare (e.g. Qiu & Gary 2003, Ding et al. 2002).
- (L) During our selected timeframe the field strength shows two stepwise changes. This type of change was observed during the three long-duration X-class flares: SOL2014-10-24T21:41 (66 minutes duration), SOL2014-10-27 T14:47 (57 minutes duration), and SOL2014-10-22T14:28 (48 minutes duration).

Classes A to D include the *classical* stepwise change presented in the majority of previous studies (e.g. Sudol & Harvey 2005, Petrie & Sudol 2010, Wang & Liu 2010, Petrie 2012, Petrie 2013). The classes E to H are not well described by the SH-model. Type I - K could be a combination of permanent change plus a misbehavior of the HMI-algorithm due to changes in the absorption line produced by the flare process (Ding et al. 2002, Qiu & Gary 2003, Burtseva et al. 2015). Finally, class L is the first report of a double stepwise change during X-class flares.

5.3 Location of the Permanent Changes

In this section, we analyze the location where permanent changes occur, for example, whether they preferentially occur in the umbra or penumbra. During 59 flares from our sample we found irreversible changes in the LOS component of the magnetic field. In our sample 100% of X-class flares (18/18), 92% of M-class events (35/38), and 35% of C-class (6/17[†]) flares showed permanent changes. We did not find any permanent changes larger than 80 Gauss in the LOS component during the only B-class flare in our sample (SOL2011-07-16T17:05).

The magnetic field does not change randomly everywhere in the active regions. The irreversible changes of the longitudinal magnetic field tended to be concentrated in compact kernels. The image in figure 5.5 shows the magnetogram of AR 11476, and the colored pixels indicate the kernel of ΔB_{LOS} during the M1.4 event (SOL2012-05-08T13:08). The surrounding panels (a-f) illustrate the typical regions where the evolution of the magnetic field exhibited the following behaviors: (a) strong permanent change, (b) quiet sun without correlation to the flare process, (c) permanent change of the penumbra field, (d) abrupt changes near the PIL, (e-f) unperturbed magnetic fields in the penumbra and umbra. The shaded areas indicate the duration between the start and the peak (gray), and from the peak to the end of the flare (blue).

The continuum images and magnetograms for the full FoV of the entire sample of flares are shown in figures 5.6 and 5.7. The locations of the permanent changes are over-plotted as colored pixels scaled from -600 G to 600 G following the color scale on the bottom. The blue dashed bar on the bottom-left in each subplot represents a length of 60 arcsecs. Black labels indicate that permanent changes were detected during the event, and red labels indicate events without permanent changes larger than 80 Gauss.

The kernels of changes tend to be located in the penumbra, close to the PIL, and near the transition between umbra and penumbra. The kernel shape does not resemble any shapes of photospheric structures observed in the continuum images and in the magnetograms. The strongest changes are usually surrounded by weaker changes in the LOS-field. Figures 5.8 and 5.9 show a close-up view of the kernels. The bar on the bottom left represents 10 arcsecs and the colored pixels range between ± 600 G.

[†]We discarded FL69 because the 45 second data has large gaps of magnetograms during the 90 minutes interval, and the SHARP data was not available.

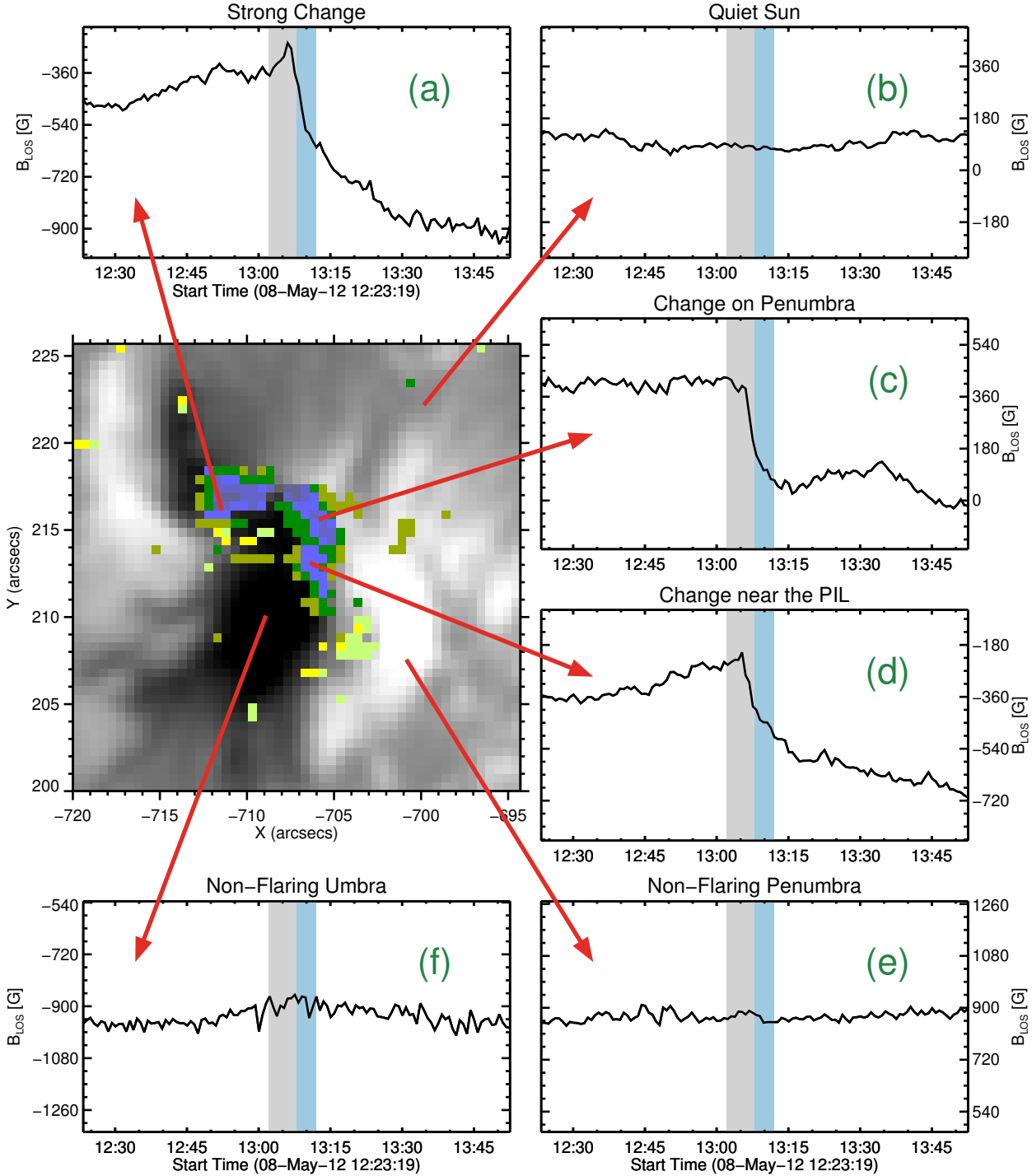


Figure 5.5: Kernel of ΔB_{LOS} during an M1.4 flare. The image shows the magnetogram of AR 11476. The colored pixels show the location of the permanent changes during SOL2012-05-08T13:08. The panels (a-f) illustrate typical evolutions of the LOS field. (a) strong permanent changes, (b) quiet sun, (c) permanent changes above the penumbra, (d) changes close to the PIL, (e) the non-flaring penumbra, and (f) the non-flaring umbra. The shaded areas in each panel show the GOES duration between the beginning and the peak (gray), and from the peak of the flare to its end (blue). The range of the y-axis is 800 G and it is centered on the average of each $B_{\text{LOS}}(t)$. This figure shows that ΔB_{LOS} changes appear in compact kernels.

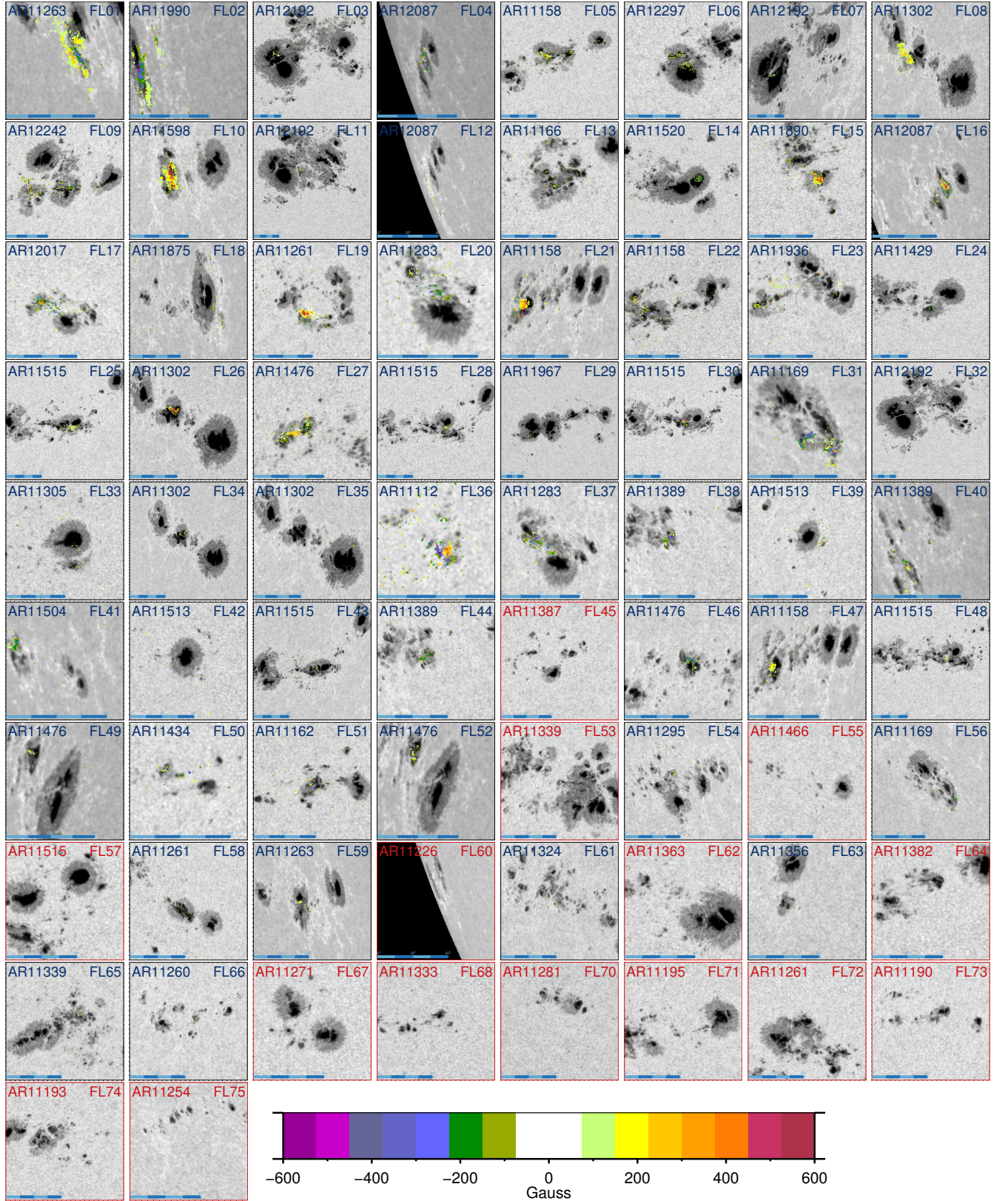


Figure 5.6: ΔB_{LOS} for the entire sample. Black boxes and labels indicate flares that showed kernels of ΔB_{LOS} . The red labels indicate events without clear evidence of ΔB_{LOS} . Colored pixels denote the size of permanent changes is clipped at ± 600 Gauss according to the color scale on the bottom. The intensity image in the background was taken during each peak of the flare. The blue dashed bar at the bottom-left represents a length of 60 arcsecs. This figure shows that ΔB_{LOS} changes appear in compact kernels.

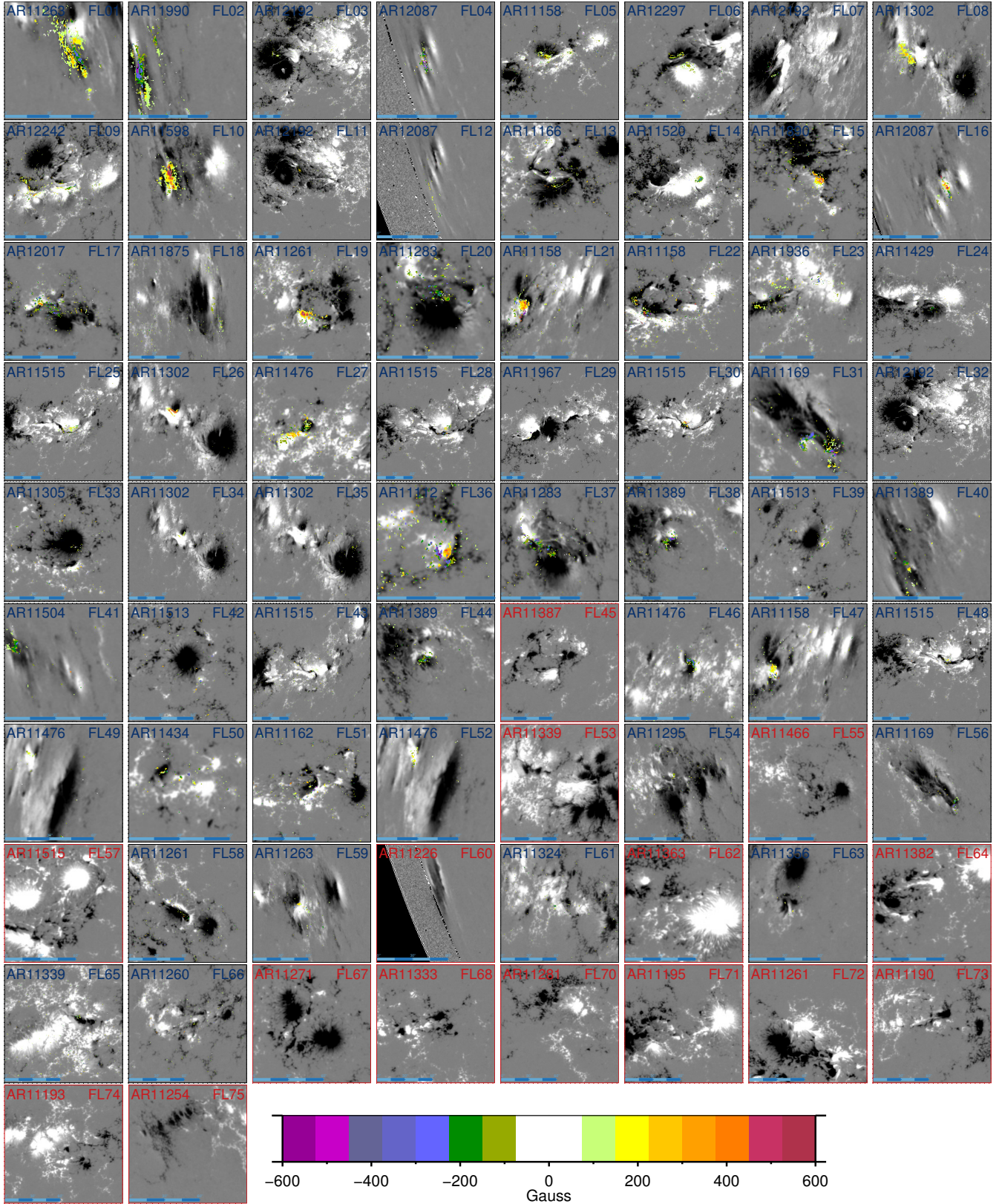


Figure 5.7: ΔB_{LOS} for the entire sample. Black boxes and labels indicate flares showing kernels of ΔB_{LOS} . The red labels indicate events without clear evidence of ΔB_{LOS} . Colored pixels denote the size of the permanent changes is clipped at ± 600 Gauss according to the color-bar on the bottom. The magnetogram in the background was taken during each peak of the flare, and is clipped to ± 800 Gauss. The blue dashed bar at the bottom-left represents a length of 60 arcsecs. This figure shows that ΔB_{LOS} changes appear in compact kernels.

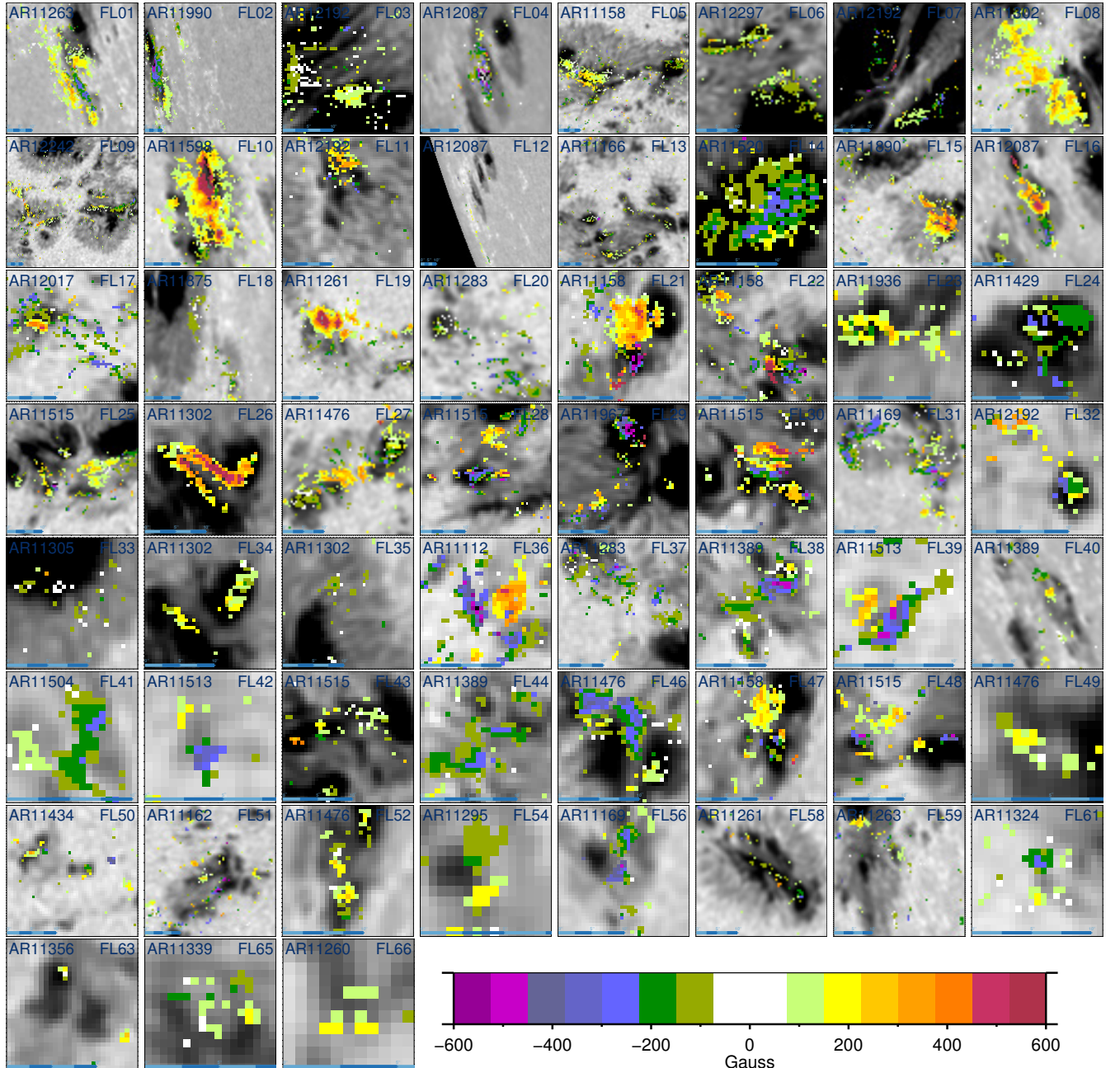


Figure 5.8: The entire sample of flares that showed kernels of ΔB_{LOS} overplotted on intensity images. Colored pixels denote the size of the permanent changes is clipped at ± 600 Gauss according to the color-bar on the bottom. The intensity image in the background was taken at peak of the flare. The blue dashed bar at the bottom-left represents a length of 10 arcsecs divided in four parts of 2.5 arcsecs. This figure shows that ΔB_{LOS} changes appear in compact kernels.

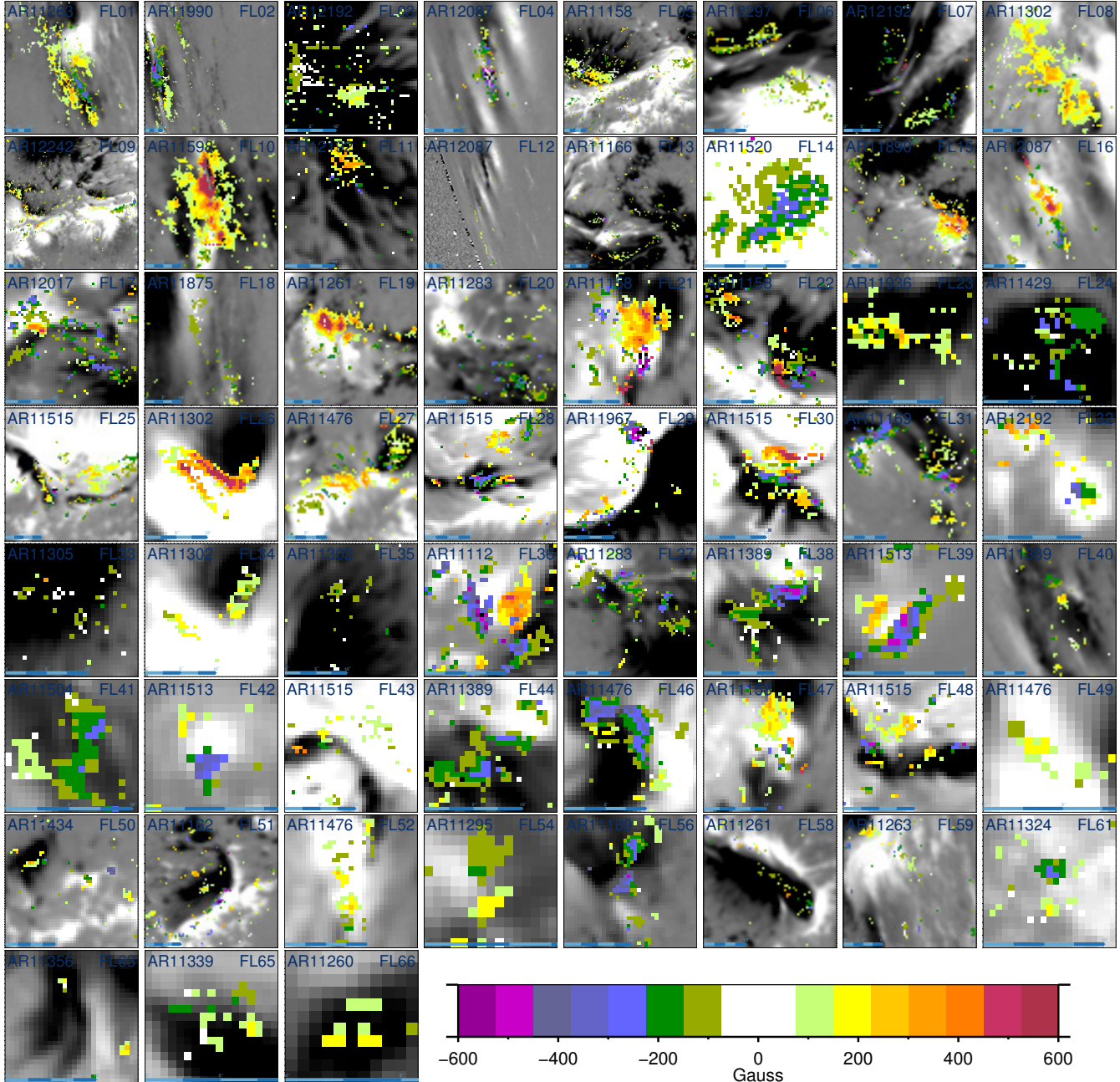


Figure 5.9: The entire sample of flares that showed kernels of ΔB_{LOS} for over magnetogram. Colored pixels denote the size of the permanent changes is clipped at ± 600 Gauss according to the color-bar on the bottom. The magnetogram image in the background was taken at peak of the flare, and clipped to ± 800 Gauss. The blue dashed bar at the bottom-left represents a length of 10 arcsecs divided in four parts of 2.5 arcsecs. This figure shows that ΔB_{LOS} changes appear in compact kernels.

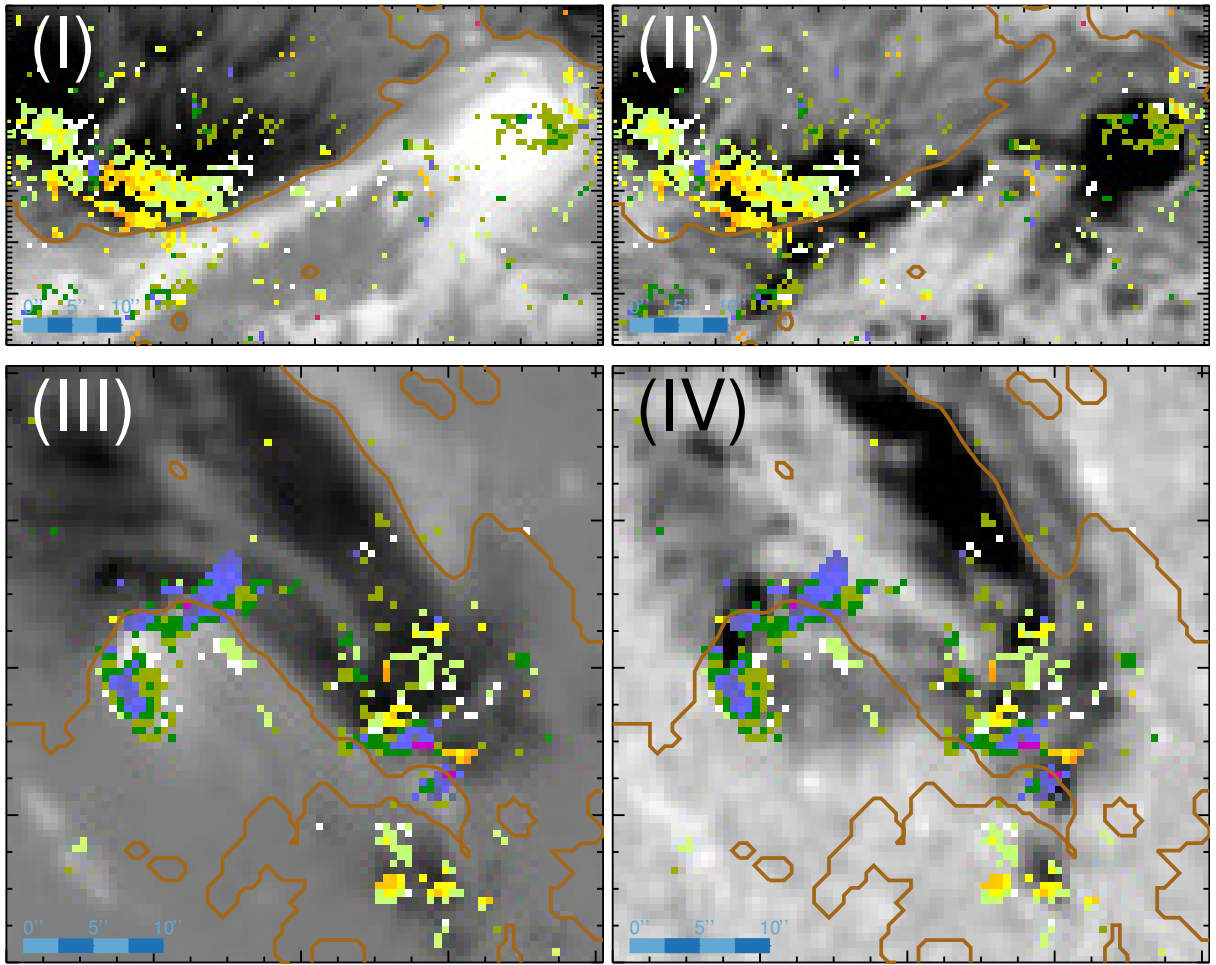


Figure 5.10: Location of ΔB_{LOS} (colored pixels) and the PIL (brown) during the X2.2 - SOL2011-02-15T01:56 (top) and M4.2 - SOL2011-03-14T19:52 (bottom) solar flares. The size of the changes clipped at ± 600 G. The magnetogram (left) and the continuum image (right) during the peak of the flare are shown in the background. The kernels of ΔB_{LOS} often appear near the PIL.

5.4 Relation between the PIL and Permanent Changes

In this section, we analyze the relation between the PIL and ΔB_{LOS} . We determine the PIL in the entire sample of active regions at the GOES peak of the flare time. We measured the closest distance of ΔB_{LOS} and the PIL. 90% of ΔB_{LOS} were within 10 arcsecs from the PIL, and 95% of ΔB_{LOS} were located within 15 arcsecs from the PIL. The LOS-changes in our sample were located near the PIL, and less than 3% of ΔB_{LOS} were located exactly on the PIL at the maximum of the flare. For all flares in our sample there was a lead polarity that showed more changes than the other polarity which is consistent with previous results e.g. Wang et al. (2002b). Figure 5.10 shows the relation between the PIL and permanent changes during the X2.2 (top) and M4.2 (bottom) flares. The brown lines in both magnetogram (left) and intensity images (right) illustrate the PIL at the peak of the flare. There were few permanent changes found on the PIL during these events (see figure 5.11, top panels). For the entire sample of changes, the number of changes (N) decay is positively correlated to the distance (d) measured from the PIL following

an exponential behavior given by the observational relation:

$$N(d) = 5093 \exp\left(-\frac{d}{4.95}\right), \quad (5.1)$$

with a Pearson correlation coefficient[†] $r_{\text{PIL}}^2 = 0.987$. Figure 5.11 - panel (a) shows the distribution of permanent changes as a function of the distance from the PIL.

We found that the strongest changes, those larger than 300 Gauss, tended to be near the PIL, and 94.5% of $\Delta B_{\text{LOS}} > 300$ G were no farther than 10 arcsecs from the PIL. The average distance of the permanent changes to the PIL is 4.95 arcsecs. This quantity is defined as *the mean distance from the PIL of ΔB_{LOS} over the active region*. It comes from the exponent distribution in equation 5.1 (see figure 5.11, a). 4.95 arcsecs is the distance from the PIL at which the population of the ΔB_{LOS} is reduced to $1/e$. Figure 5.11 - panel (b) shows the size of the change as a function of the distance measured from the PIL. The color scale illustrates the density of ΔB_{LOS} at a certain distance. The densest region with at least 30 changes was found no further than 5 arcsecs and with absolute typical changes lower than 200 Gauss.

We have seen by inspection that the distance from the PIL where permanent changes are located is larger for stronger flares. For example, for small flares, all permanent changes are located within 3 arcsecs from the PIL, but for X-class flares the permanent changes reach farther from the PIL. Figure 5.11 - panel (c) shows the histogram of the mean distance for the entire sample of flares. The average distance of ΔB_{LOS} for 54 flares ranged between 3.3 to 5.0 arcsecs. There was no correlation neither of the permanent changes and the GOES class of the flare with the median nor the mean distances from the PIL. Figure 5.11 - panel (d) shows the GOES class as a function of the mean distance measured from the PIL. The average value of the mean distance of ΔB_{LOS} from 80 G to 750 G measured from the PIL for all flares was 4.36 arcsecs.

[†]The definition of the correlation coefficient r^2 is given by

$$r^2 = \left(\frac{n \sum x_i y_i - \sum x_i \sum y_i}{\sqrt{\left[n \sum x_i^2 - (\sum x_i)^2 \right] \left[n \sum y_i^2 - (\sum y_i)^2 \right]}} \right)^2, \quad (5.2)$$

in case of a semi-log scale

$$x \equiv x, \quad y \equiv \log(y), \quad (5.3)$$

and in a log-log scale

$$x \equiv \log(x), \quad y \equiv \log(y). \quad (5.4)$$

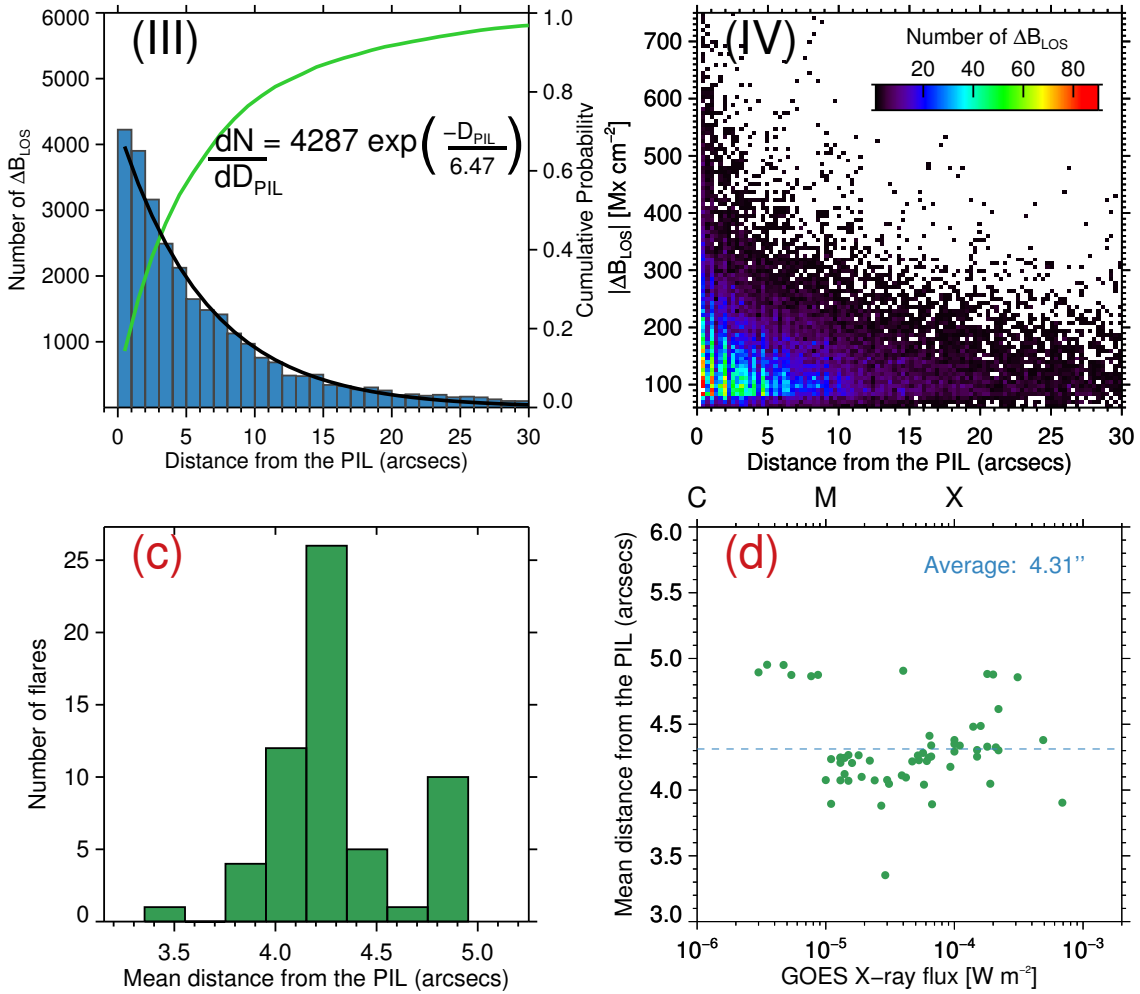


Figure 5.11: Permanent changes and distance from the PIL in arcsecs. (a) Histogram of the distance of permanent changes from the PIL, which shows an exponential decay. The green curve shows the cumulative probability, and the black shows the best-fit of an exponential model between 0 to 20 arcsecs. r^2 was calculated following the equation 5.2 without weighing any value. (b) Scatter plot of the distance from the PIL of the permanent changes as a function of the size of the change. Colors illustrate the number of changes from 1 (black) to 90 (red). (c) Histogram of the mean distance from the PIL of each flare. (d) The mean distance from the PIL as function of the GOES class. More ΔB_{LOS} and the ΔB_{LOS} strongest changes are found near the PIL.

5.5 White-Light Emission and Permanent Changes

During *some* flares enhanced WL emission is observed (e.g. Hudson et al. 1992, Matthews et al. 2003, Fletcher et al. 2007, Jess et al. 2008). Such events are known as WL flares. The origin of WL emission during flares is still under debate. Several authors have studied the physical mechanisms, the atmospheric conditions, and the relation of WL emission with other emissions during flares, such as HXR emission (e.g. Metcalf et al. 2003, Kuhar et al. 2016, Krucker et al. 2011). In particular, the WL emission and permanent changes of the magnetic field have been to be co-spatial, or near each other (Sudol & Harvey 2005, Kleint 2016). In this section we aim to study the relation between WL emission and ΔB_{LOS} during the 75 flares in our sample.

For very energetic flares, the WL enhancement is larger with respect to the average emission from the active region, but this may not be the case for small events. To find the location the WL emission and to be able to make the distinction, we masked the background. We calculated the running difference between two consecutive images to trace the temporal evolution of the WL, and we rejected pixels with intensities less than five times the standard deviation of each the running-difference profile (σ). σ was calculated in the non-flaring intervals before and after the flare. As the continuum emission is observed within a time range that covers various images, we searched for WL during the entire duration of the flare. The final mask contains all the locations with a WL enhancement at some time during the flare.

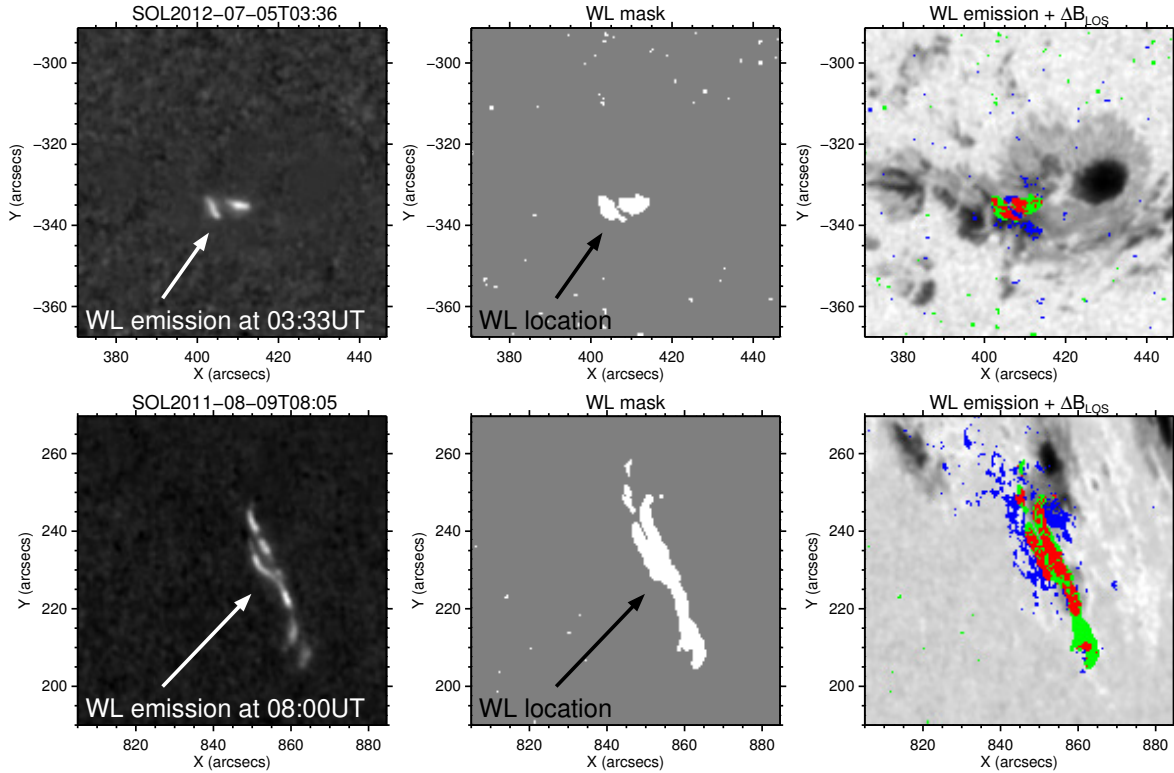


Figure 5.12: Correlation between WL emission and magnetic field changes during the M4.7 - SOL2012-07-05T03:36:00 (top), and X6.9 - SOL2011-08-09T08:05:00 (bottom). The left column shows the WL enhancement at the peak of the WL emission. The middle column shows the total area of the WL emission above a 5σ level. The right column shows the continuum image at the peak of the flare. Colored pixels indicate the location of ΔB_{LOS} (blue), WL emission (green), and red pixels show positions where ΔB_{LOS} and WL emission coincided. The ΔB_{LOS} kernels and the WL emission often overlap but do not have a one-to-one spatial relation.

The left column of figure 5.12 shows the WL enhancement at the peak of the WL emission. The middle column shows the location of the WL emission, based on the standard deviation criteria explained above. The right column displays the intensity image at the peak of the flare. The colored pixels indicate the location of the WL emission (green), the position of the permanent changes (blue), and the places where we found both WL emission and magnetic field changes (red). 55 flares showed WL emission and in 53 events both ΔB_{LOS} and WL emission were observed. We found WL emission without ΔB_{LOS} during 2 C-class flares. The compact magnetic field kernels cover areas comparable with the WL emission. The WL emission was often located at the center of the kernels of ΔB_{LOS} or next to them. Additionally, the closer the permanent changes are to the WL emission, the larger the amplitude of the permanent change. The compact kernels of magnetic field changes do not have a one-to-one relation to the WL emission.

5.6 Lorentz force in the LOS Component

A significant amount of energy is transported from the corona to other layers of the solar atmosphere during flares. The energy emitted can restructure the magnetic field and produce a back reaction in lower layers (Hudson et al. 2008). If irreversible changes occur during a flare, an external Lorentz force associated with the flare might be injected into the photosphere. We can estimate the vertical change of the Lorentz force in the photosphere as (Hudson et al. 2008):

$$\Delta F_Z = \int_{A_{\text{Pho}}} (B_Z \Delta B_Z - \Delta B_X B_X - B_Y \Delta B_Y) dA, \quad (5.5)$$

with an integral over an area A_{Pho} in the lower photosphere where irreversible changes were found. We neglect contributions from higher layers as we can assume that the magnetic field decreases fast enough with height. With the LOS data, we can quantify a lower limit of the injected Lorentz to the photosphere as $\Delta F_Z \simeq \Delta F_{\text{LOS}} \simeq B_{\text{LOS}} \Delta B_{\text{LOS}} A_{\text{Pho}}$. Figure 5.13 - panel (a) shows the distribution of all permanent changes of the Lorentz force. The mean ΔF_{LOS} unsigned change was 6.4×10^{22} dyne, and $\sim 54\%$ of the ΔF_{LOS} changes were negative.

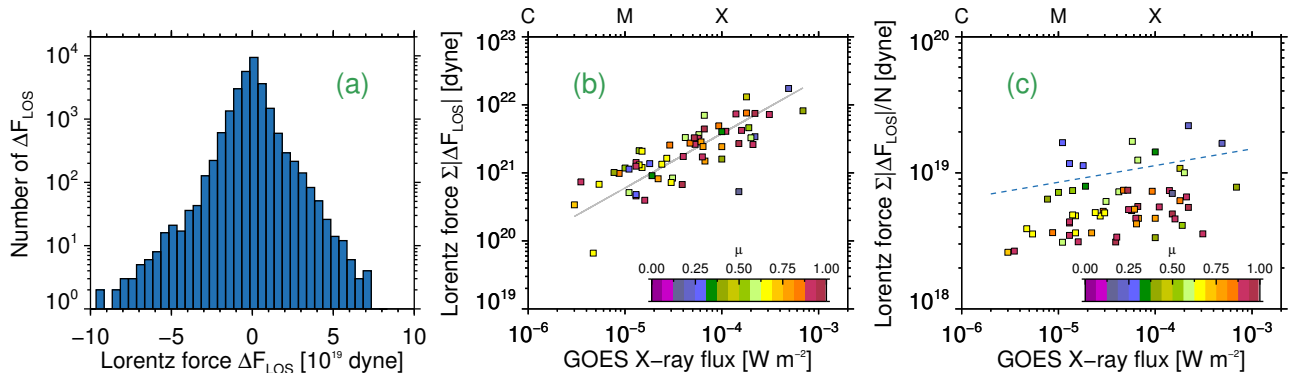


Figure 5.13: The change of the Lorentz force in the LOS. (a) Histogram of the whole sample of irreversible Lorentz-force changes in units of dyne. (b) total Lorentz force change and (c) total Lorentz force change normalized to the total number of permanent changes per flares as a function of the GOES class. The color scale represents the center-to-limb heliospheric location of each flare. Limb flares show stronger changes in the LOS component of the Lorentz force.

The Lorentz force changes ranged from 6.6×10^{19} to 1.7×10^{22} dyne. The mean changes for X-, M- and C-class events were 5.7×10^{21} dyne, 2.0×10^{21} dyne, and 6.4×10^{20} dyne, respectively. These values agree with Hudson et al. (2008) and Alvarado-Gómez et al. (2012). Figure 5.13b shows the total absolute value of the Lorentz force change per flare as a function of the GOES class. Panel b indicates positive correlation between the change in the Lorentz force and the GOES class. However, we mentioned earlier that the stronger the flare, the more changes are observed. To eliminated potential bias from the total perturbed area, we divided the total Lorentz force change by the number of permanent changes observed in each flare (see figure 5.13, panel c). In this case, the correlation that we observed before disappears, but there is a clear center-to-limb difference. The limb flares, represented by blue squares, show stronger changes in the LOS component of the Lorentz force.

5.7 Statistics of Permanent Magnetic Field Changes

In this section, we analyze the entire sample of LOS changes regarding the general features of the flares, such as the total signed/unsigned magnetic flux change, the area where the magnetic field changed, the rate the change, and the distribution of ΔB_{LOS} . Flares release most of their energy during the impulsive phase. The duration of this phase can be approximately calculated as the time between beginning and the peak of the flare, as observed by GOES. Top panel in figure 5.14 shows the SXR GOES lightcurve during the M3.9 flare SOL2011–10–02T00:50. The green shade illustrates the interval between the start and the peak times of the flare, while the blue shade covers from the peak until the end of the flare. The de-projected area of ΔB_{LOS} as function of the total duration of the flare is on the left side of figure 5.14. The de-projected area of ΔB_{LOS} as a function of the approximate duration of the impulsive phase is shown on the bottom right of figure 5.14. Colors in the bottom panels stand for the center-to-limb distance of each flare. We did not find any correlation between the approximate duration of the impulsive phase, the total duration of the flare, or the center-to-limb distance and the de-projected area of permanent changes.

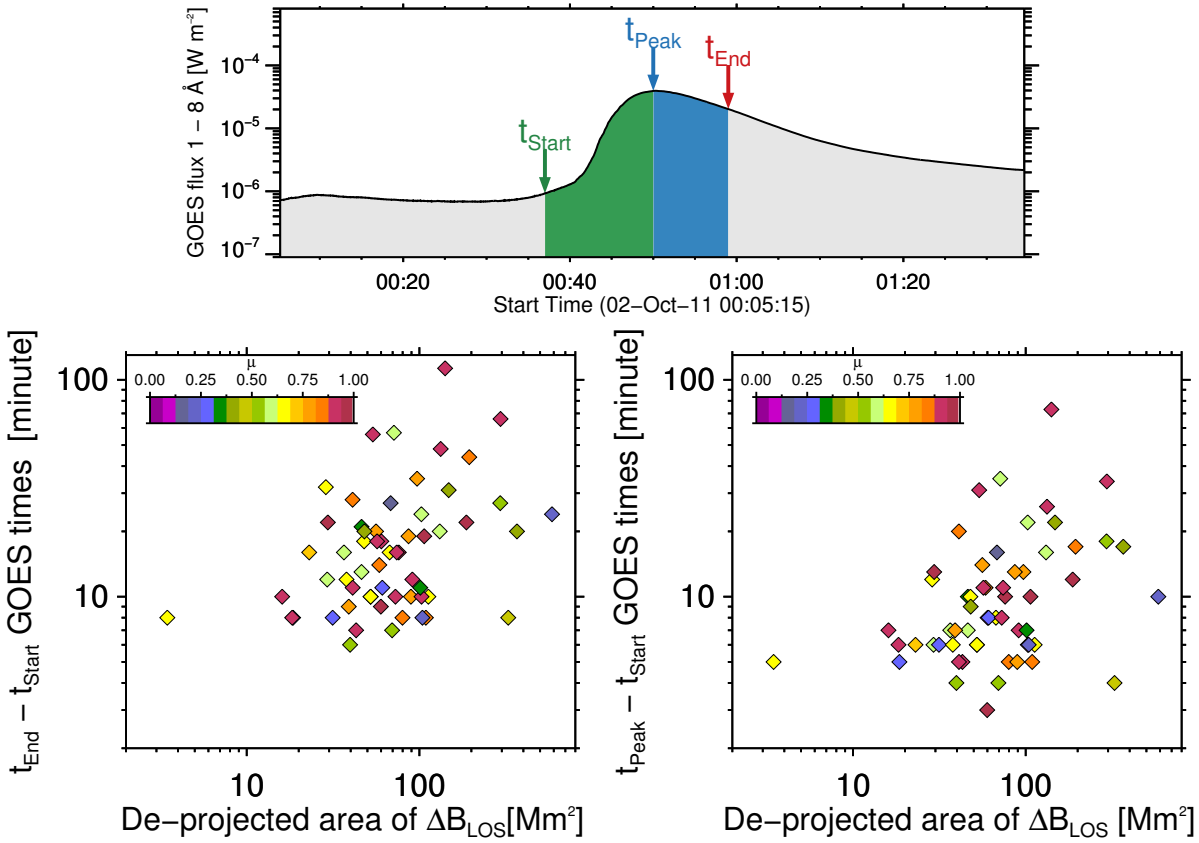


Figure 5.14: *Top:* GOES lightcurve during the M3.9 flare SOL2011–10–02T00:50. The interval between the start and peak times is shown in green, and the duration from the maximum of the flare until end in blue. *Bottom:* The duration between the start and peak times (left panel), and the total duration of the flare (right panel) as a function of the total de-projected area of ΔB_{LOS} disturbed by the flare. Colors illustrate the center-to-limb distance of the flare. We did not find any correlation between these variables.

Does the total permanent change in the signed/unsigned magnetic flux have any relation with the energy released by the flares? Figure 5.15 shows the total signed change for each flare as a function

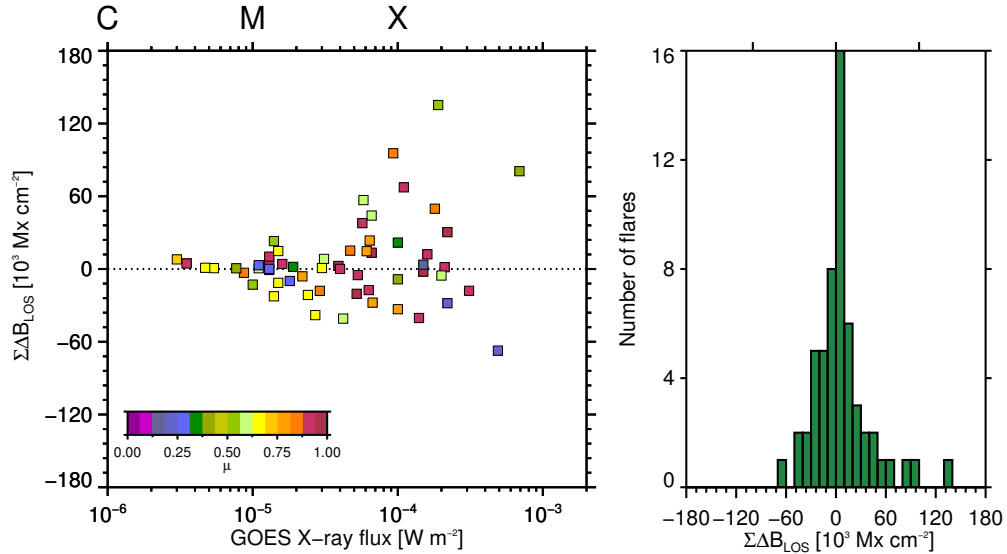


Figure 5.15: Total signed permanent flux change per flare regarding the GOES class (left). Histogram of flares and the total signed change (right). The distribution shows a tendency of the total signed flux change to be different from zero for flares larger than M-class.

of the GOES class (left), and as histogram (right). We found that the amount of positive and negative changes tend to be equal for small flares. For larger flares, one of the polarities dominates. All limb flares with longitude greater than 74° ($\mu \lesssim 0.275$) showed more negative changes and the total negative change was also larger. 12 flares located near disk center, i.e., with longitude less than 30° ($\mu \gtrsim 0.866$), showed more positive changes. In the 59 events with ΔB_{LOS} , 34 flares showed more negative changes. In terms of the total flux, during 32 flares the negative polarity changed more. The total signed change ranging between $-67.3 \times 10^3 \text{ Mx cm}^{-2}$ to $247.3 \times 10^3 \text{ Mx cm}^{-2}$. On the left of figure 5.16, we show the total unsigned change as a function of the GOES class. These quantities show a power-law relation with a correlation coefficient of $r^2 = 0.452$. The right panel shows the total positive (red) and negative (blue) permanent change as a function of the GOES class for each event. Both positive and negative changes also show a power-law correlation with a larger scatter than the total unsigned change.

The total magnetic area permanently disturbed by the flare process and the energy released during each event may be correlated suggesting that stronger flares would disturb more the photospheric fields. A more intense event may be able to inject more energy into the lower layers of the solar atmosphere and may disturb larger areas. Figure 5.17 shows the permanently changed area as a function of the GOES class for each event; the color scale stands for the center-to-limb location of each event. Let's recall that our sample of flares was chosen without any restriction on the location of the event on the solar disk. Events that occur close to the solar limb are largely affected by projection effects due to the spherical geometry of the Sun. We measured the projected area (figure 5.17, left), and the de-projected area (figure 5.17, right). The projected area ($A_{\text{Projected}}$) in Mm^2 is directly related to the number of changes per flare (N) as $A_{\text{Projected}} [\text{Mm}^2] = 0.133N \text{ Mm}^2$. 0.133 represents a constant that transform the 0.504 arcsecs spatial scale of HMI to mega meters². The de-projected area is equal to the projected area divided by the μ of each pixels. i.e., $A_{\text{De-projected}} = \sum_i A_{i-\text{Projected}} / \mu_i$, where $A_{i-\text{Projected}}$ and μ_i are the area and the heliographic angle of each pixel.

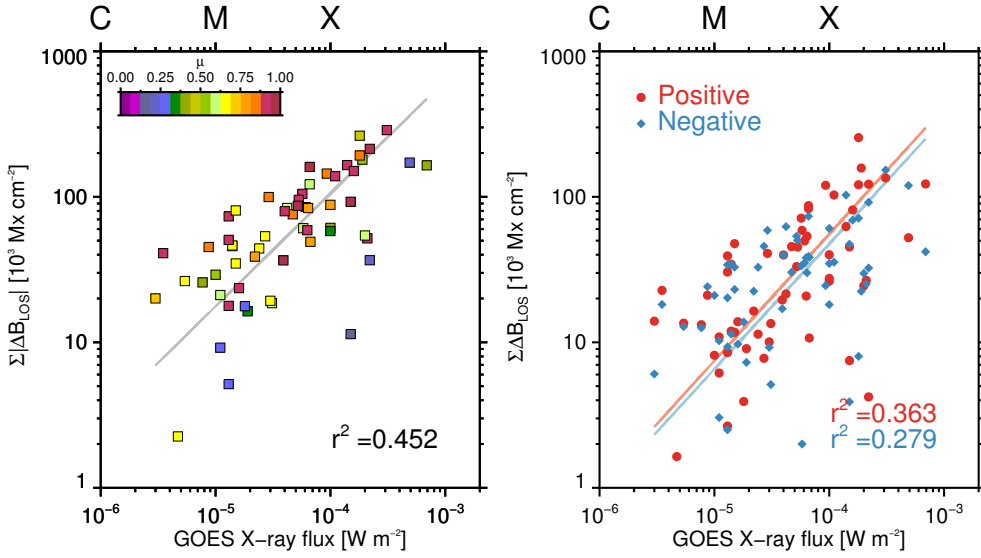


Figure 5.16: Total flux change in the LOS magnetic field. *Left:* Total unsigned change of the magnetic field where permanent changes were found, as a function of the GOES class. The color of the squares denotes the center-to-limb distance of each event. *Right:* The total LOS changes per polarity as a function of the GOES classification. Red illustrates the total positive changes and blue the negatives. The larger the flare, the larger the change in the magnetic flux. In addition, limb flares have lower unsigned changes.

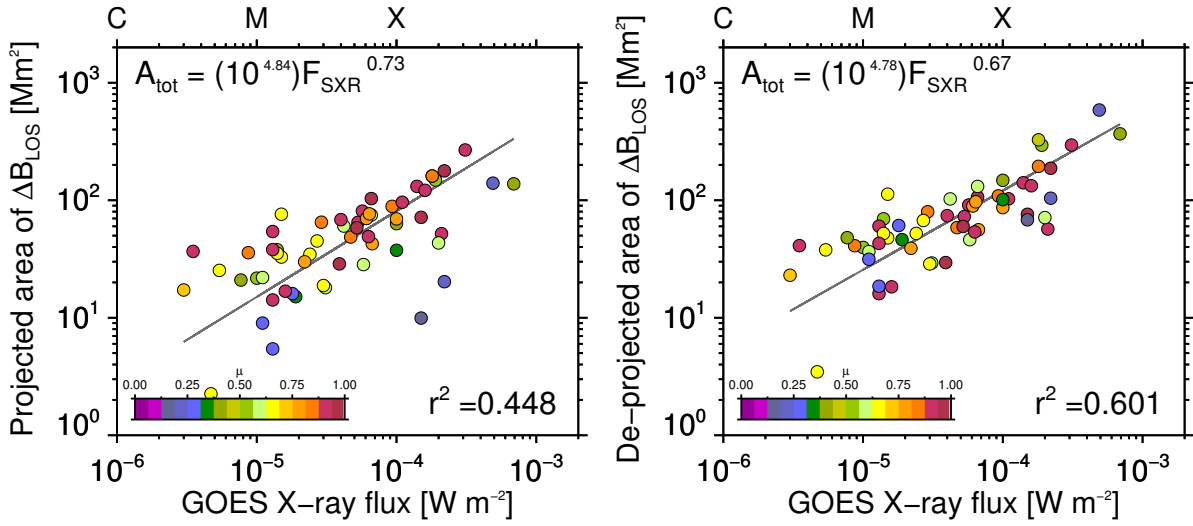


Figure 5.17: Area where the magnetic field changed as a function of the GOES class. The area that HMI measures suffers from projection effects. Panels show the projected areas A (left), and the real de-projected areas A/μ (right). The colors of the circles indicate the center-to-limb distance for each event. There is a power-law correlation with the thermal energy emitted by the flare and the area where ΔB_{LOS} are located. The larger the flare, the larger area where the magnetic field changed. This relation follows a power-law correlation with a positive exponent.

Figures 5.17 show a power-law relation between the size of the permanently changed area (A) and the GOES class (F_{SXR}) given by the relations:

$$A_{\text{Projected}}(F_{\text{SXR}}) = 10^{4.84} F_{\text{SXR}}^{0.73}, \quad A_{\text{De-projected}}(F_{\text{SXR}}) = 10^{4.78} F_{\text{SXR}}^{0.67}. \quad (5.6)$$

The correlation coefficients are $r^2_{\text{Projected}} = 0.448$ and $r^2_{\text{De-projected}} = 0.601$ for projected and de-projected areas, respectively. The dispersion of the de-projected area is lower. We did find a correlation of the area of permanent changes with the energy of the flare (GOES class).

Petrie & Sudol (2010) found a correlation between the location of the LOS-field permanent changes and the center-to-limb location of the flare. They suggested that limb flares tend to produce more changes than events near Sun center. We find the opposite as shown in figure 5.17. The colors stance of the heliocentric angle for each event, 1 being the solar center and 0 the limb. For the projected area case, we found fewer irreversible changes for limb flares than for flares near disk center (figure 5.17, blue circles in left panel). The de-projected area shows that flares near the limb do not disturb more area than those that occurred near solar center (figure 5.17, blue and dark red circles in right panel). Thus, we did not observe a center-to-limb relation of ΔB_{LOS} . The LOS-variations near the limb can be a consequence of a change in the configuration of the field (Spirock et al. 2002). If the field becomes more horizontal after the flare, the LOS component observed near the limb will increase. This change in the geometry of the field is a direct consequence of the momentum conservation (Hudson et al. 2008).

How fast does the magnetic field change? We measured the rate of change ($\Delta B_{\text{LOS}}/\Delta t$) as the ratio between the amplitude of the change and the duration of the change $\Delta t = \pi n^{-1}$ (Sudol & Harvey 2005). We estimated the rate of the change taking into account that the maximum temporal resolution for our data is 45 seconds, i.e., values of πn^{-1} less than this value were set to 45 s. Figure 5.18 shows the histogram of the rate of the magnetic change. We found that the rate of LOS-magnetic field change ranged between 0.2 and 307 G m⁻¹, with an average around 22.1 G m⁻¹. 91% of the changes ranged between 0.2 and 50 G m⁻¹. Our results are consistent with those presented by Sudol & Harvey (2005). These authors measured $\Delta B_{\text{LOS}}/\Delta t$ ranging between 2 and 200 G minute⁻¹, with the majority of $\Delta B_{\text{LOS}}/\Delta t$ were within 2 and 40 G minute⁻¹. In addition, we found that the rate of the changes decreases following an exponential behavior with a *mean-change-rate* equal to 20.7 G minute⁻¹.

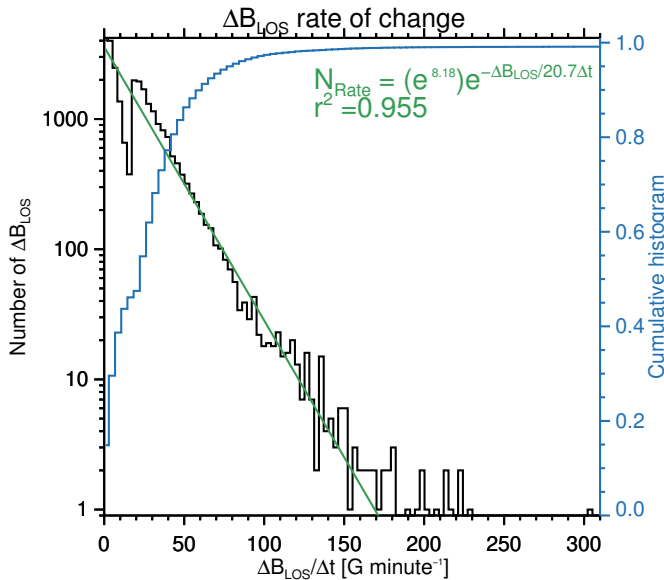


Figure 5.18: Number of ΔB_{LOS} as function of the rate of ΔB_{LOS} in units of G minute⁻¹. We fitted data within the interval between 0 to 150 G minute⁻¹. The majority of ΔB_{LOS} have a rate of change between 0.2 and 50 G minute⁻¹.

The energy required to perturb the complex magnetic network of the active region is larger for strong permanent changes. Is the occurrence of permanent changes of a few hundred Gauss therefore more probable? We tested this hypothesis individually for each flare in our sample that shows ΔB_{LOS} , and for the entire sample as well. Figure 5.19 shows the distribution of the LOS-magnetic changes during C7.7, M4.2 and X4.9 flares. The blue line represents the best-fit of an exponential model for the 3 examples flares with correlation coefficients of $r^2_{\text{C7.7}} = 0.946$, $r^2_{\text{M4.2}} = 0.971$ and $r^2_{\text{X4.9}} = 0.938$. For all flares where we found kernels of permanent changes, their distributions followed an exponential behavior with a median correlation coefficient $r^2_{\text{Median}} = 0.907$.

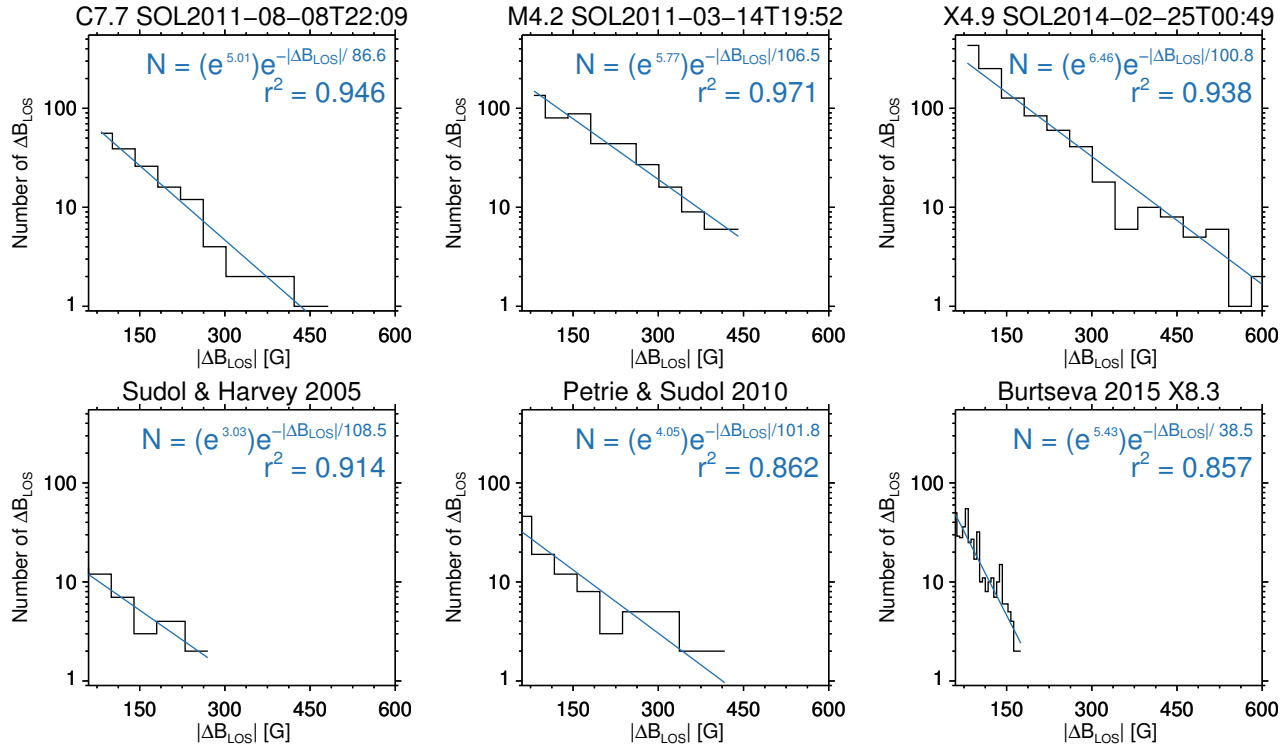


Figure 5.19: *Top:* The distribution of the changes during 3 examples flares with C (left), M (middle), and X (right) GOES classes. *Bottom:* The reconstructed histograms of the distribution of magnetic changes from Sudol & Harvey (2005), Petrie & Sudol (2010), and the X8.3 flare studied by Burtseva et al. (2015). The data binning is 40 G as in Sudol & Harvey (2005). The distribution of the Burtseva et al. (2015)'s event was not rebinned due to its low dynamic range. The distributions of ΔB_{LOS} for flares from other authors and our study follow an decreasing exponential law.

Distribution of permanent changes observed by the Global Oscillation Network Group (GONG) had ~ 2.5 to ~ 3 arcsecs of spatial binning (Sudol & Harvey 2005, Petrie & Sudol 2010, Burtseva et al. 2015), which is almost 5 times larger than HMI observations. We have re-calculated the distributions presented by these authors in semi-log scale in the bottom panels of figure 5.19. The histograms have bins of 40 G as in Sudol & Harvey (2005) to compare both data sets. However, the distributions from the Burtseva et al. (2015)'s X-class flares were not rebinned due to their low dynamic range. The distributions given by Sudol & Harvey (2005), Petrie & Sudol (2010) are the selection of profiles they considered best representing their flare sample. We found that their distribution follows an exponential behavior, and our own results agree with their studies because our distributions also follow an exponential pattern.

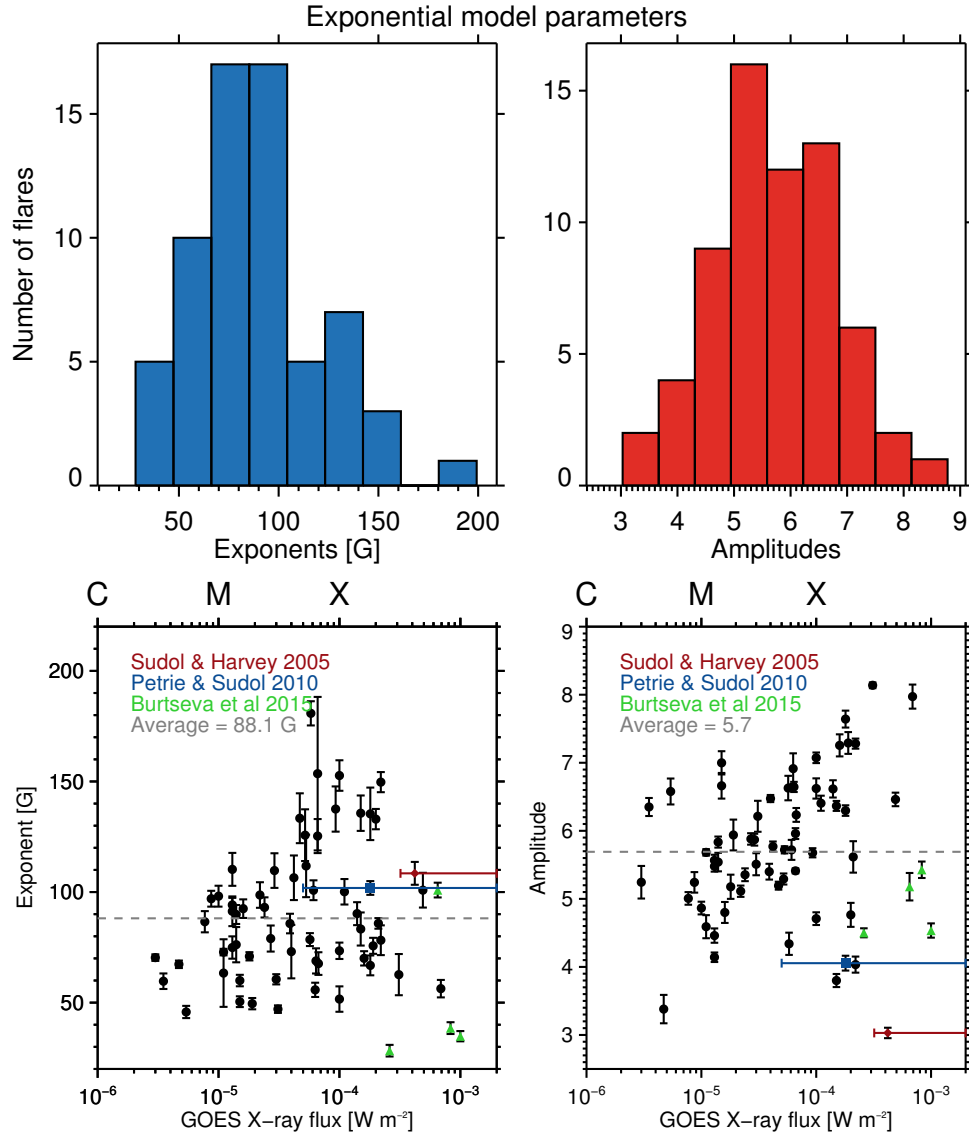


Figure 5.20: Top panels show the histogram of the exponents (left) and the amplitudes (right) of the exponential model best-fit. Bottom panels illustrate the relation between the exponential model parameters as a function of the GOES class. We fitted flares that show ΔB_{LOS} plus three events from Burtseva et al. (2015), and the distributions from Sudol & Harvey (2005), Petrie & Sudol (2010). The averaged decay constant τ is $\tau = 88.1 \pm 31.7$ G, and the average value of the amplitudes is $A = 5.7 \pm 1.1$.

We fitted an exponential function $N(|\Delta B_{\text{LOS}}|) = (e^A)e^{-|\Delta B_{\text{LOS}}|/\tau}$ to the distribution of the changes given by for each flare in our sample, plus to six distributions from other authors cited previously. A is the amplitude and τ is the inverse exponent of the function. The top panels in figure 5.20 show the histogram of the exponents and the amplitudes. The bottom panels in the same figure show the relation between the model parameters as a function of the GOES class. The assigned value for the GOES class (x-axis, red and blue data points) is the average GOES class for the sample of Sudol & Harvey (2005), Petrie & Sudol (2010) and the bars cover the entire range of energies studied by them. We found that (1) the exponents for Burtseva et al. (2015) are smaller, (2) the averaged decay constant τ is $\tau = 88.1 \pm 31.7$ G, (3) there is no correlation between the exponent and the GOES class, and (4) the average value of the amplitudes is $A = 5.7 \pm 1.1$.

Weak ΔB_{LOS} of less than 100 G were observed more often than larger permanent changes (Sudol & Harvey 2005, Petrie & Sudol 2010). We examined the distribution of the entire sample of permanent changes during the 59 flares. We found in total ~ 27 100 pixels that showed ΔB_{LOS} . Figure 5.21 shows the unsigned size distribution of ΔB_{LOS} . The occurrence of permanent changes with different amplitudes follows an exponential model. The observational relation is

$$N(|\Delta B_{\text{LOS}}|) = (e^{9.26}) \exp\left(-\frac{|\Delta B_{\text{LOS}}|}{95.9}\right). \quad (5.7)$$

where the correlation coefficient is $r^2 = 0.985$. This relation suggests that there are many changes lower than the 80 Gauss limit that we set. We found the permanent changes range from 80 G to ~ 750 G, in contrasts with previous studies that found changes up to 450 G (Sudol & Harvey 2005, Petrie & Sudol 2010, Kleint 2016). 533 profiles, which corresponds to $\sim 2\%$ of the total sample of changes, showed irreversible changes larger than 450 G. The mean permanent change was 95.9 G, which is given by the inverse of the exponent of the fitted model. 95.9 G is the size of ΔB_{LOS} at which the population of the ΔB_{LOS} is reduced to $1/e$. The amplitude depends on the number of events studied, but the exponent does not.

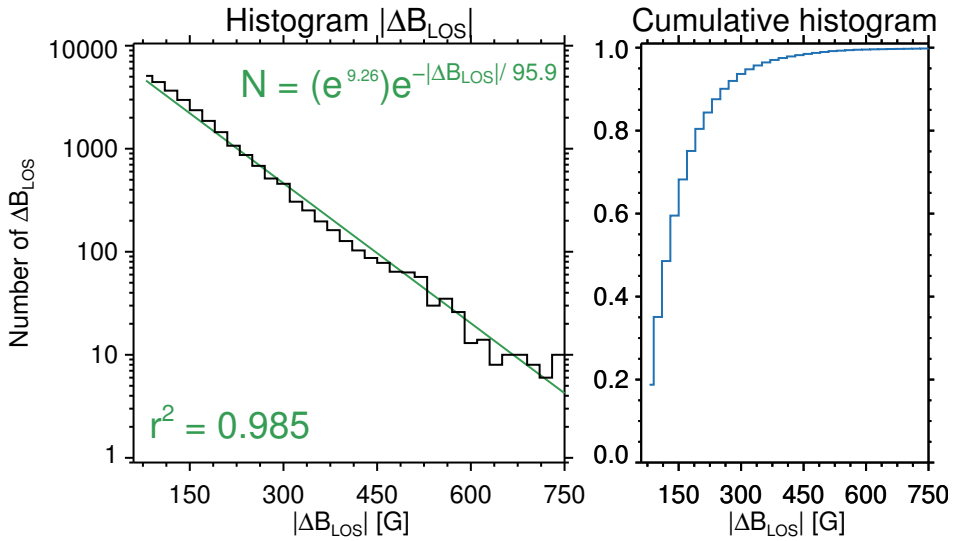


Figure 5.21: Exponential distribution of the LOS magnetic field changes. The left panel shows the histogram, and the right panel shows the cumulative histogram. The occurrence of permanent changes with different amplitudes follows an exponential model.

Chapter 6

Vector Magnetic Field Analysis

This work studies the relation between flares and the production of permanent and abrupt changes of the photospheric magnetic fields. Compared to chapter 5, the advantage is that we have all 3 components of \vec{B} (inclination, azimuth and strength), but the disadvantage is that the cadence is 12 minutes. We analyze the projection effects linked to permanent changes; is there a difference between the changes from the LOS observations and the same component derived from the vector data? We also search for purely vector magnetic field changes that were not observed in the LOS component. We analyze if all 3 components of the field change due to the flare process, or if there is a predominant component that changes most. Finally, we study the relation between the PIL and irreversible vector changes.

6.1 Vector Magnetic Field Quantities

The vector of the magnetic field allow us to study projections effects and the dynamics of the field during solar flares. The SHARP data have the three vector components' field strength $|\vec{B}|$, inclination γ with respect to the LOS, and azimuth ψ ranging from 0 to 360 degrees, where 0 points toward the north pole of the Sun. Measurements not at disk center of the LOS magnetic field are distorted due to the projection effects, such as the curvature of the Sun. The vector field components can be transformed from the image-plane reference frame to heliographic coordinates that help to solve ambiguities in the azimuth (Gary & Hagyard 1990). These transformation also help in the interpretation of the vector measurements off-center (see e.g. Gary & Hagyard 1990). Here we have converted HMI/SHARP vector components into the coordinates: B_X (westward), B_Y (northward), and the radial B_Z (out of photosphere) following the calculations explained in Sun (2013) and Gary & Hagyard (1990).

The dynamics of the photosphere and other types of events related to flares, such as sunquakes, can be studied by measuring the photospheric Lorentz force (see e.g. Kosovichev & Zharkova 1998, Hudson et al. 2008, Fisher et al. 2012, Alvarado-Gómez et al. 2012). We have calculated the three components

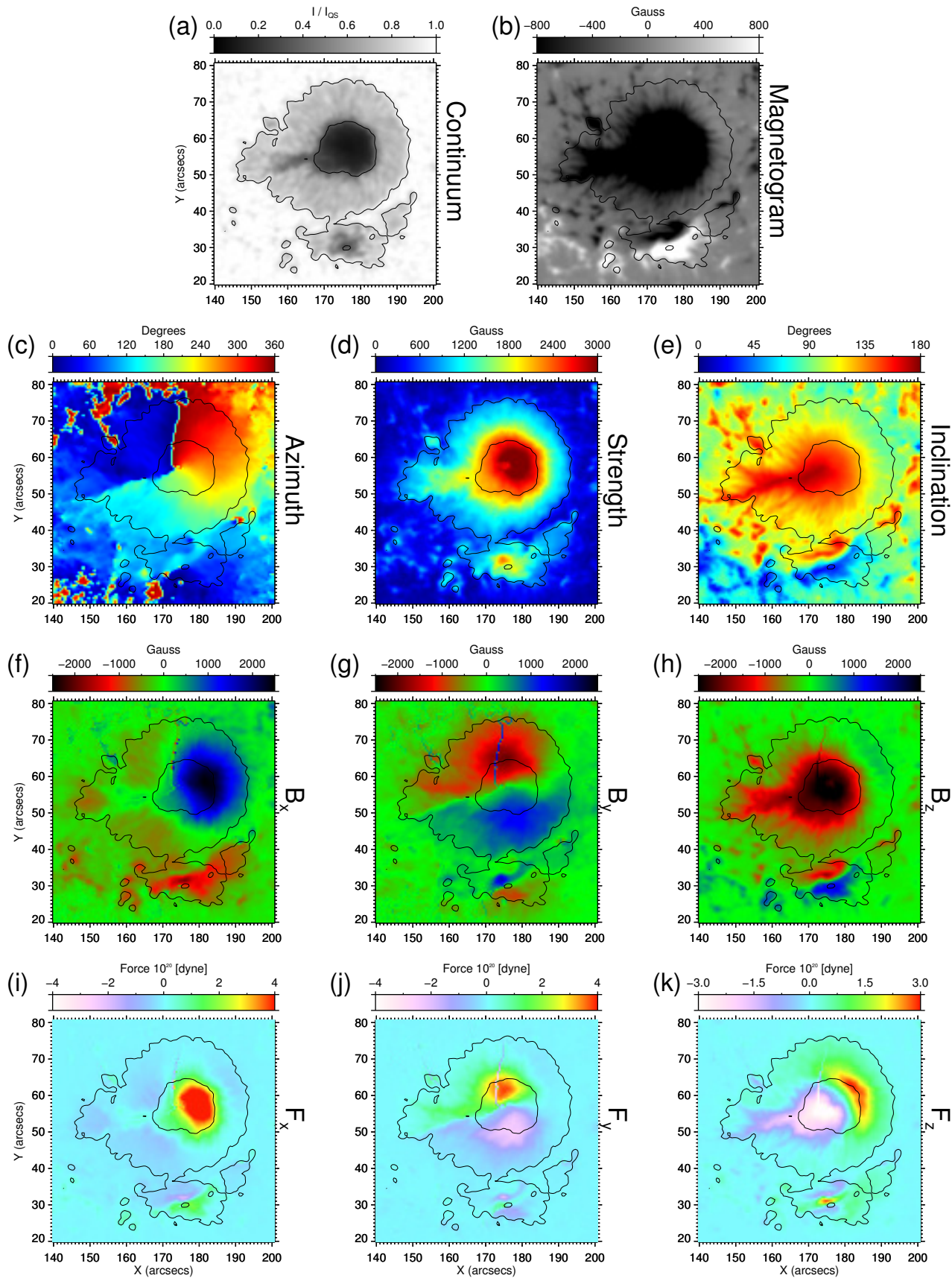


Figure 6.1: AR 11305 before the M3.9 flare SOL2011-10-02T00:50. From top-left to bottom-right the panels show images of the intensity (a), magnetogram (b). The three components of the vector magnetic field: azimuth (c), strength of the field (d), and the inclination with respect to the LOS component (e). The tree components of the magnetic field in coordinates: B_x (f), B_y (g), B_z (h). And the three components of the Lorentz force: F_x (i), F_y (j), F_z (k).

of the Lorentz force in heliographic coordinates as

$$F_X = -\frac{1}{4\pi} \int_{A_{ph}} B_Z B_X dA, \quad (6.1)$$

$$F_Y = -\frac{1}{4\pi} \int_{A_{ph}} B_Y B_Z dA, \quad (6.2)$$

$$F_Z = \frac{1}{8\pi} \int_{A_{ph}} (B_X^2 + B_Y^2 - B_Z^2) dA, \quad (6.3)$$

where A_{ph} stands for the photospheric area, i.e., the size of the pixel .

Past studies of permanent changes of the magnetic field during flares have mostly studied the LOS component of the field. The LOS component from the vector data is calculated as

$$B_{LOS}(\text{Vector}) = |\vec{B}| \cos(\gamma) \quad (6.4)$$

Figure 6.1 shows images of the active region 11305 of the continuum (a), magnetogram (b), the azimuth(c), strength (c), and inclination (d) of the field. The three components of the magnetic field B_X , B_Y , and B_Z are shown in panels (f-h). The three components of the Lorenz force F_X , F_Y , F_Z are in panels (i-k).

Comparisons of the LOS components of the magnetic field from 45 s cadence magnetograms and the vector data from the ME-inversion are shown in figure 6.2. This scatter plot represents all points where we have found stepwise changes. The 45s-magnetograms were chosen to be the closest to each 12m-vectorgram. The outliers between ± 800 G from the main trend were measured during the peaks of flares. The dashed line shows the one-to-one relation. Both LOS components match when the magnetic field has values smaller than ~ 1000 Gauss. For larger values (strong fields) the HMI-algorithm for the 45 second data underestimates the magnetic field (see Couvidat et al. 2012b, Liu et al. 2007). This behavior was previous explained by Hoeksema et al. (2014), and described in their figure 17, page 3515.

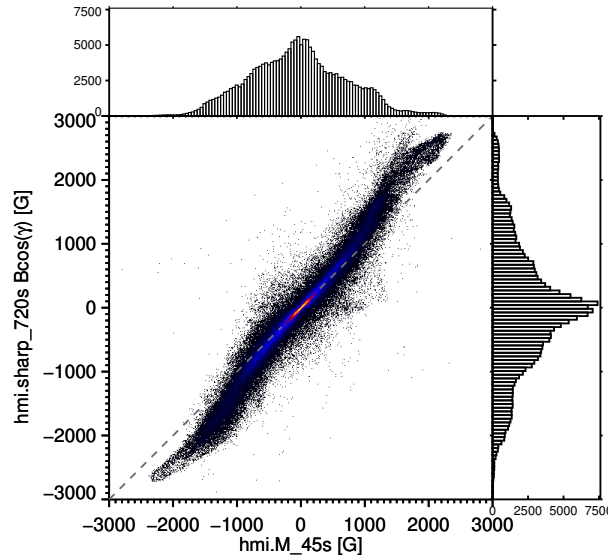


Figure 6.2: Comparison between the LOS components from vector data and the 45 s magnetograms. Both LOS components of the magnetic field from magnetograms and vector data match when the magnetic field has values smaller than ~ 1000 Gauss.

6.2 Co-spatiality between ΔB_{LOS} and Vector Magnetic field changes

The HMI vector magnetic field SHARP data have a relatively low cadence when compared with the timescales of flares. For our analysis, we selected a time range of 90 minutes around the peak of the flare (see §4.3.2). Therefore, we studied the evolution of the magnetic field with ten data points for each profile during an extended interval of few minutes longer than 90 minutes (in the best case). Taking into account that the stepwise model has five free parameters (equation 4.1), it is not reliable to fit this model to the vector magnetic field data. We co-aligned the 12-minute vector magnetic field data to the 45-second magnetograms. We over-plotted the three components of the magnetic field on the stepwise changes that we had previously determined. Figure 6.3 shows the temporal variation of the vector component during an M- and an X-class flare. In those two locations, the LOS components of the magnetic field (black and orange lines) showed permanent changes when approaching the peak of the flares with amplitudes of 220 G (M-class) and 100 G (X-class), while in the two examples the azimuth varied linearly. The field strength did show permanent changes related to the flare. The inclination angles showed irreversible changes of $\sim +7^\circ$ and $\sim -5^\circ$ are the reason of the observed changes in the LOS component.

The three components of the field may show changes, but not all the three components varied equally. We observed four cases for the temporal evolution of the vector magnetic field: (i) Irreversible change in the three vector components. (ii) Change in the strength of the field and one angle (inclination or azimuth). (iii) Change in only one component. (iv) None of the three components showed a clear permanent change. Figure 6.4 shows the changes in the three components of the field in the same locations where permanent changes in the LOS component were found during an M6.1 and an X1.9 flares. We measured the variations of the vector components by taking the difference of non-flaring images before and after the flare. During these two examples, changes in the inclination and the azimuth up to 21 degree were observed. The permanent changes in the magnetic field strength ranged mostly between ± 400 G. The patch of changes for the whole sample of flare showed a structure characterized by the stronger changes begin located in the *center* of the patch or near the boundary zone between umbra-penumbra, or/and penumbra-quiet-sun. The larger changes were usually surrounded by smaller changes.

In total, we checked manually for permanent vector changes in 44 flares: 7 X-class, 31 M-class, and 6 C-class flares. We verified the changes in 10 components independently: $B_{\text{LOS}}(\text{vector}) = |\vec{B}| \cos \gamma$, $|\vec{B}|$, γ , ψ , B_x , B_y , B_z , F_x , F_y , F_z . The statistics of the percentage of LOS-irreversible changes that also show permanent changes in the each component of the vector magnetic field is shown in table 6.1. Each column from the top to bottom represents the whole B_{LOS} in the 44 flares ('All flares'), the X-class, M-class, C-class, disk-center and limb flares. Disk-center and limb flares were divided by the hemisphere located at half of the solar radius from disk center ($\sim 35^\circ$).

Does $B_{\text{LOS}}(\text{vector})$ show stepwise changes when the magnetogram does not? The correlation between the LOS component measured directly and obtained from the vector is 80%. The remaining 20% might be associated to underestimation of the LOS component of the field. LOS component is obtained through calibration, so it fundamentally depends on the assumption of weak fields. Also, the cadence of the two quantities, in the best case, the vector data has 10 data points in an extended 90 minutes interval, while the LOS-component has 120 data points. This order of magnitude in the number of measurements along the observing time to reconstruct the evolution of the magnetic field might hide small or fast changes to the vector magnetic field data.

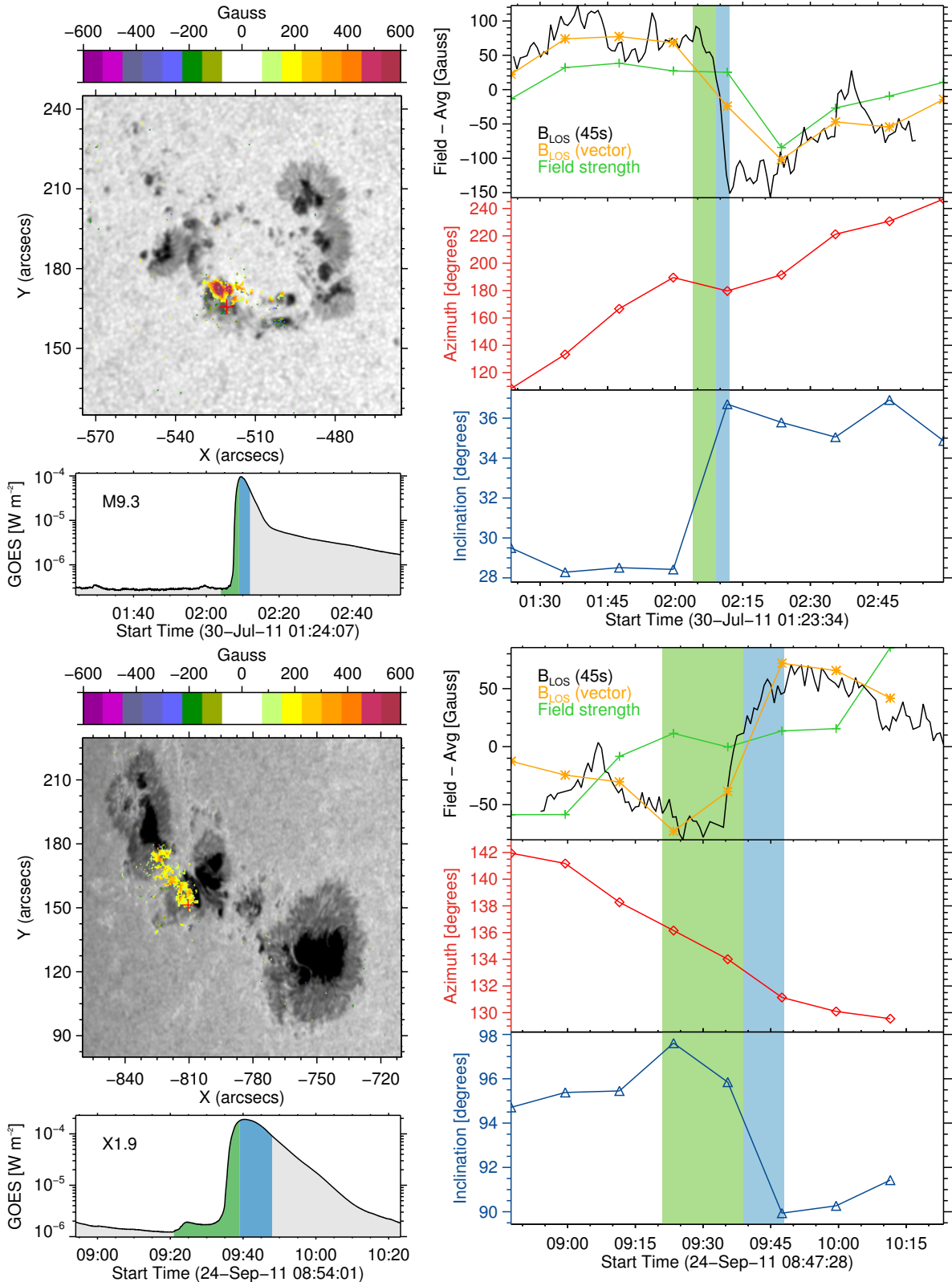


Figure 6.3: Permanent changes of the vector magnetic field. *Left:* Intensity images of the active regions and the GOES curves of the flares M9.3 (SOL2011-07-30T02:09) and X1.9 (SOL2011-09-24T09:39). *Right:* Temporal evolution of the three vector components of the field: inclination (bottom), azimuth (middle), and strength (top, green). The LOS component calculated from vector data is plotted in yellow, and the 45s LOS data are shown in black. The shades represent the start to peak (green), and peak to the end (blue) GOES times. This figure shows two examples of the permanent vector magnetic field changes associated with ΔB_{LOS} .

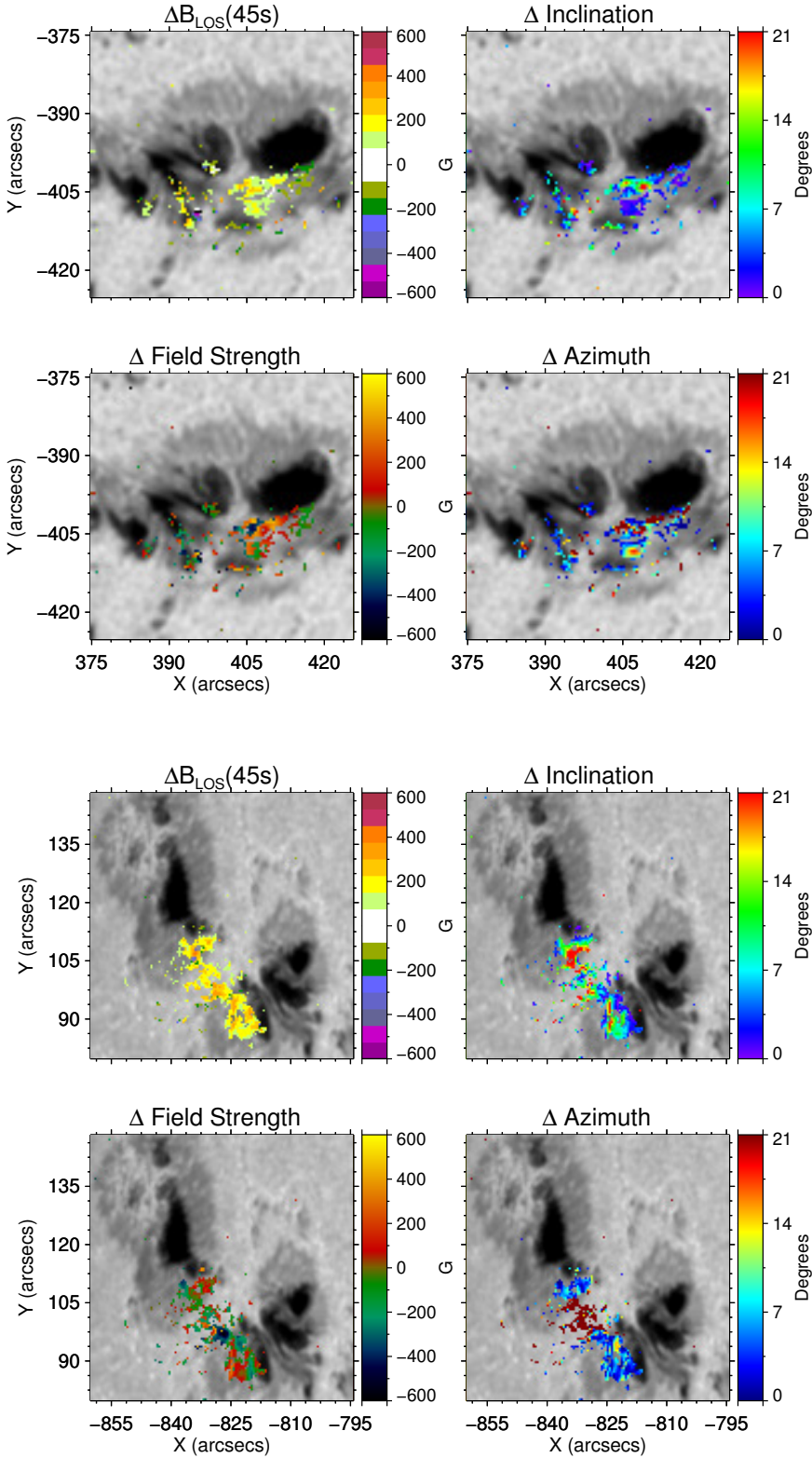


Figure 6.4: Changes of the vector field where permanent variations in the LOS component were found during the M6.1 (SOL2012-07-05T11:44) and X1.9 (SOL2011-09-24T09:39) flares. The sub-panels for each event show the patch of permanent changes in the LOS component (top-left), the variations of the inclination (top-right), field strength (bottom-left), and azimuth (bottom-right). The patch of changes showed a structure characterized by stronger changes being located in the *center* of the patch or near the boundary zone between umbra-penumbra, or/and penumbra-quiet-sun.

	Events	$\Delta \vec{B} \cos \gamma$	$\Delta \vec{B} $	$\Delta\gamma$	$\Delta\psi$	ΔB_X	ΔB_Y	ΔB_Z	ΔF_X	ΔF_Y	ΔF_Z
All Flares	44	80%	58%	59%	40%	52%	46%	56%	51%	49%	54%
X - class	7	82%	56%	67%	45%	59%	51%	57%	53%	51%	60%
M - class	31	80%	61%	57%	39%	49%	45%	58%	51%	49%	52%
C - class	6	71%	47%	43%	27%	47%	28%	40%	38%	33%	45%
Disk-Center	30	79%	55%	59%	40%	54%	44%	52%	49%	47%	54%
Limb	14	81%	63%	59%	40%	50%	48%	63%	53%	53%	54%

Table 6.1: Percentage of the ΔB_{LOS} that showed irreversible vector changes as well.

Are changes predominantly in field strength, inclination, or azimuth? 59% the field strength, and inclination changes showed permanent changes in ΔB_{LOS} , while permanent changes in the azimuth were found in 40% of the cases. The stronger the flare, the more changes of the direction of the field were observed. The inclination and the azimuth decreased the percentage of correlation with the ΔB_{LOS} as the energy of the flare decreased. For instance, the correlation for the inclination with ΔB_{LOS} decreased from 67% for X-class, 57% for M-class, to 43% for C-class flares. For changes near-limb, the field strength showed 8% more permanent changes associated with ΔB_{LOS} than the disk-center changes. The angles γ and ψ had the same correlation for limb and disk-center locations. In addition, we found that the ΔB_{LOS} were associated with stepwise changes in $\Delta|\vec{B}|$ or $\Delta\gamma$ in the 67% of the cases. 74% of ΔB_{LOS} showed changes in the $\Delta|\vec{B}|$ or $\Delta\psi$. 75% of ΔB_{LOS} the magnetic field changed its direction permanently, i.e., we observed changes in $\Delta\gamma$ or $\Delta\psi$. Finally, 85% of ΔB_{LOS} were associated with a permanent change in either of the three components of the vector magnetic field, i.e., $\Delta|\vec{B}|$, or $\Delta\gamma$, or $\Delta\psi$. We also searched for places where two or the three component changed permanently in the same place. We found that the ΔB_{LOS} were associated changes in $\Delta|\vec{B}|$ and $\Delta\gamma$ in the 16% of the cases. 28% of ΔB_{LOS} showed $\Delta|\vec{B}|$ and $\Delta\psi$. 26% of ΔB_{LOS} changed permanently both angular components, i.e., we observed stepwise changes in $\Delta\gamma$ and $\Delta\psi$. Just 12% of ΔB_{LOS} showed permanent changes in the three components of the vector magnetic field, i.e., $\Delta|\vec{B}|$, and $\Delta\gamma$, and $\Delta\psi$.

Do the components of the magnetic field (B_X , B_Y , B_Z) and the Lorentz force show the same permanent changes? The maps in figure 6.5 show the orientation of the vector magnetic field before and after an M-class flare. The field became more horizontal after the eruption. The red (positive polarity) and blue (negative polarity) are observed larger and more oriented along the PIL after the flare. The bottom panels in figure 6.5 illustrate the type of permanent changes in B_X , B_Y , B_Z and the components of the Lorentz force. Panels (a) the three components decreased as well as F_X , while F_Y increases its magnitude and F_Z remains constant. Panel (b) shows the opposite behavior: B_X and B_Y decreased and B_Z increases, though the three Lorentz components show a positive change. Panel (c) illustrate a case during which the three components changed permanently with different amplitudes. Panel (d) shows a case where just one component changes irreversibly. In this example, the B_X and F_Z showed clear negative and positive changes, respectively.

The vertical and horizontal components of the field, as well as the Lorentz force components, change separately. B_X and B_Y are parallel to the solar surface. Variations in these components are associated with changes in the horizontal component of the magnetic field. In particular, there are more variations in B_X than in B_Y that were associated with ΔB_{LOS} . B_X points in the same direction as the solar rotation, and B_Y is in the direction of the solar poles. B_Z is radial to all points of the solar surface, and it is associated with the vertical field. 56% of ΔB_{LOS} shows irreversible changes in the vertical field. B_Z is equal to the LOS component only at disk-center, thus, the missing 44% of the changes can be explained by changes in

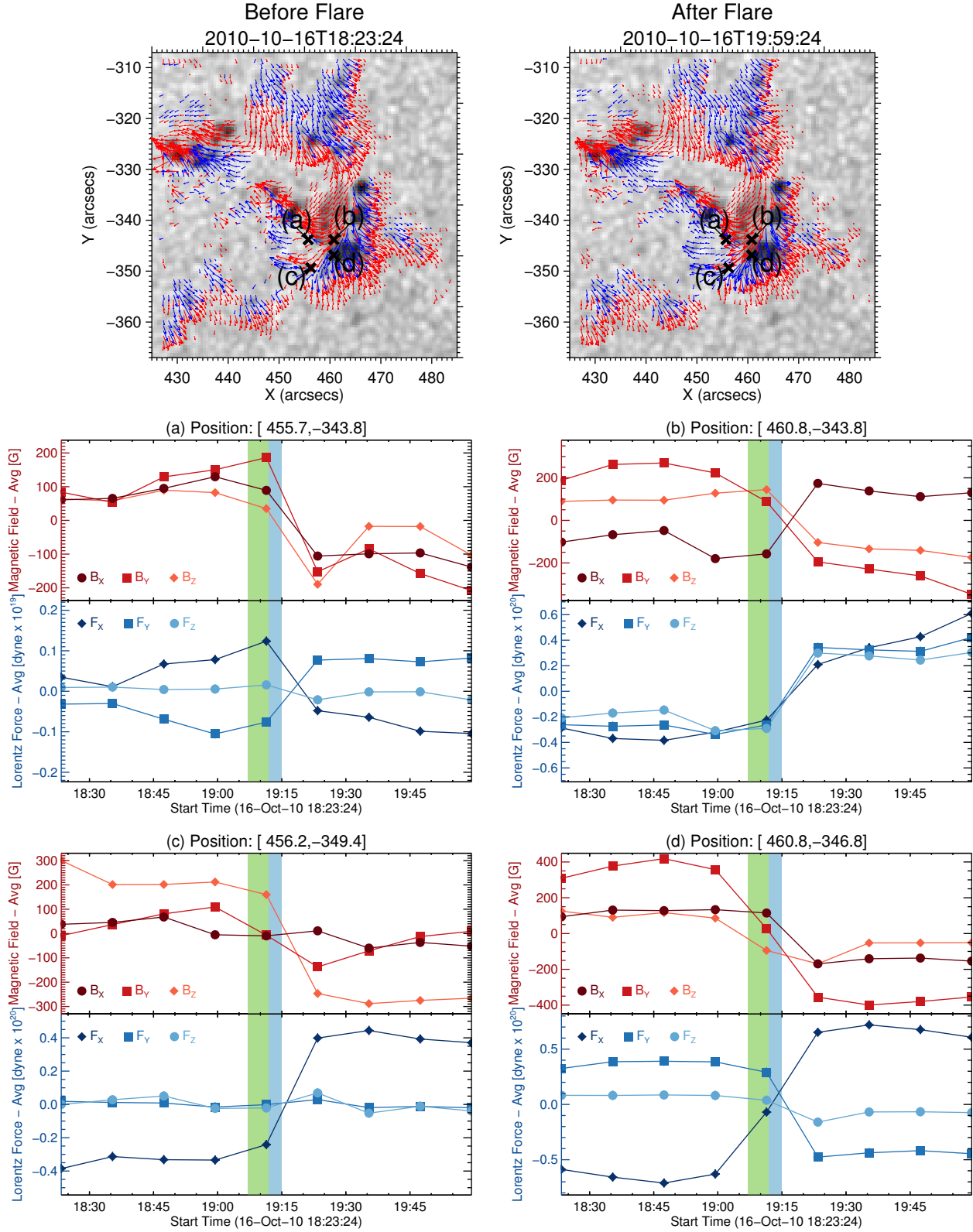


Figure 6.5: Permanent changes of the B_x , B_y and B_z components of the vector magnetic field and the Lorentz force. The maps on the top show the intensity images of active region AR 11112 before (18:23UT) and after (19:59 UT) a M2.9 flare. The vector magnetic field is overplotted. Red and blue arrows stand for positive and negative radial fields. Panels (a-d) show the temporal evolution of the magnetic field (top panels), and the Lorentz force components (bottom panels) of the points marked by crosses on the maps. The \vec{B} components (B_x , B_y , B_z) and the Lorentz force components change permanently but not always in the same way.

B_X and B_Y not at disk-center. Regarding the permanent changes of the Lorentz force, we found that the 54% of ΔB_{LOS} is accompanied by a change in the F_Z Lorentz force component. We observe that larger flares are associated with permanent changes in all three Lorentz force components.

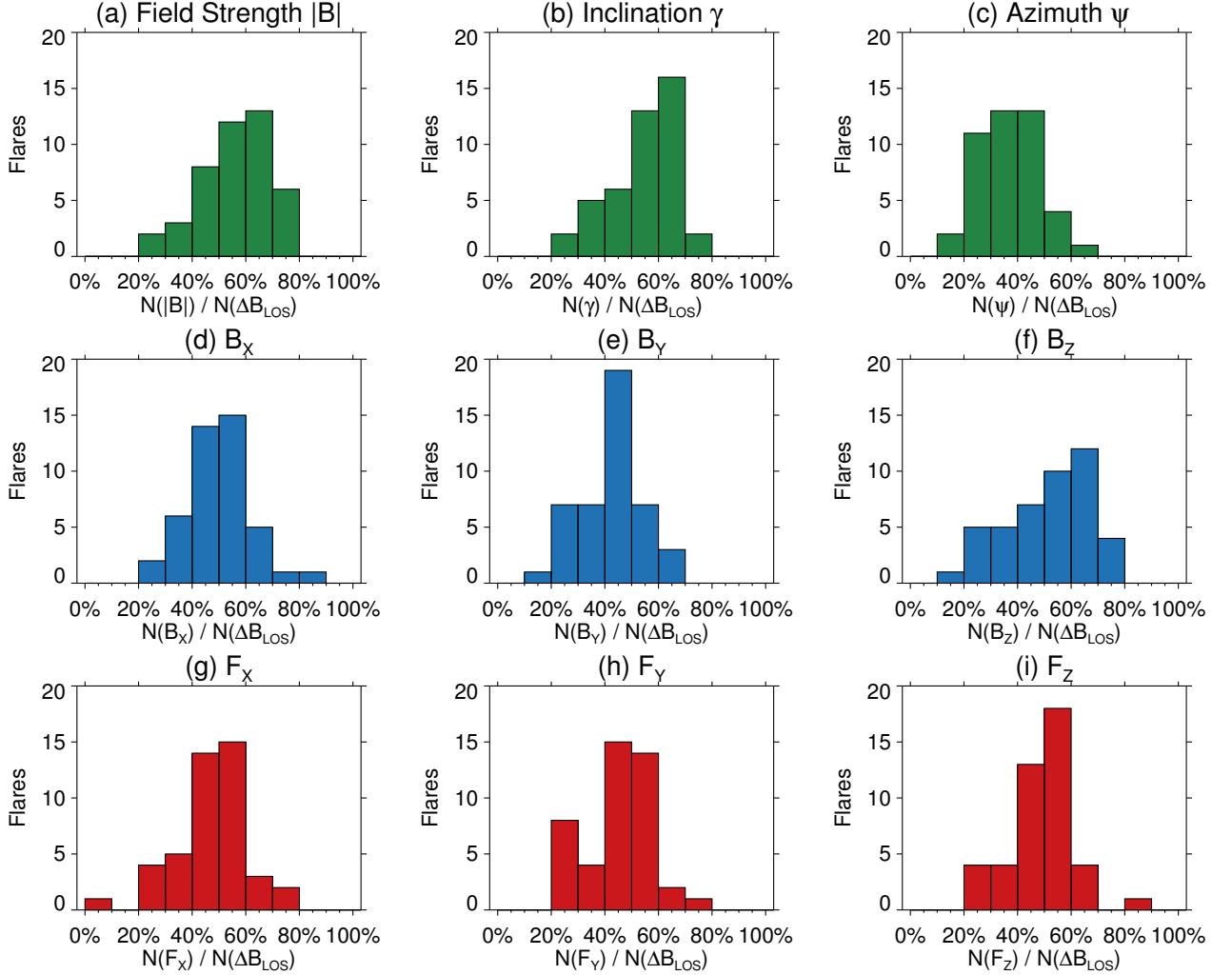


Figure 6.6: Histograms of permanent vector changes associated with ΔB_{LOS} per flare. N stands for the number of permanent changes observed in (a) field strength, (b) inclination, (c) azimuth, (d) B_X , (e) B_Y , (f) B_Z , (g) F_X , (h) F_Y , (i) F_Z . $N(\Delta B_{\text{LOS}})$ is the number of permanent changes in the LOS.

The statistics above were derived from the 44 flares associated with ΔB_{LOS} . But individual flares may differ. Here we analyze the relation of ΔB_{LOS} and permanent changes in the vector magnetic field components per flare. Figure 6.6 shows the number N of permanent vector changes associated with ΔB_{LOS} per flare. 21 flares showed correlations larger than 50% in $\Delta|\vec{B}|$ and $\Delta\gamma$ components (panels a, b), but 39 flares showed correlation smaller than 50% in the case of the γ (panel c). In 39 flares ΔB_{LOS} and the horizontal field correlated 40% and 60% (panels d, e), where 19 events showed a correlation between 40-50% for B_Y (panel e). The correlation with the vertical field ranged from 10% to 80%, with a peak of 12 events in the range of 50-60% of the correlation (panel f). For the Lorentz force components, 32 flares had a correlation with ΔB_{LOS} between 40-60% (panels g-i). There is one C-class flare that has a small correlation of 4% in F_X (panel g).

Larger LOS-permanent changes have been observed with a preference to occur near the limb (Cameron

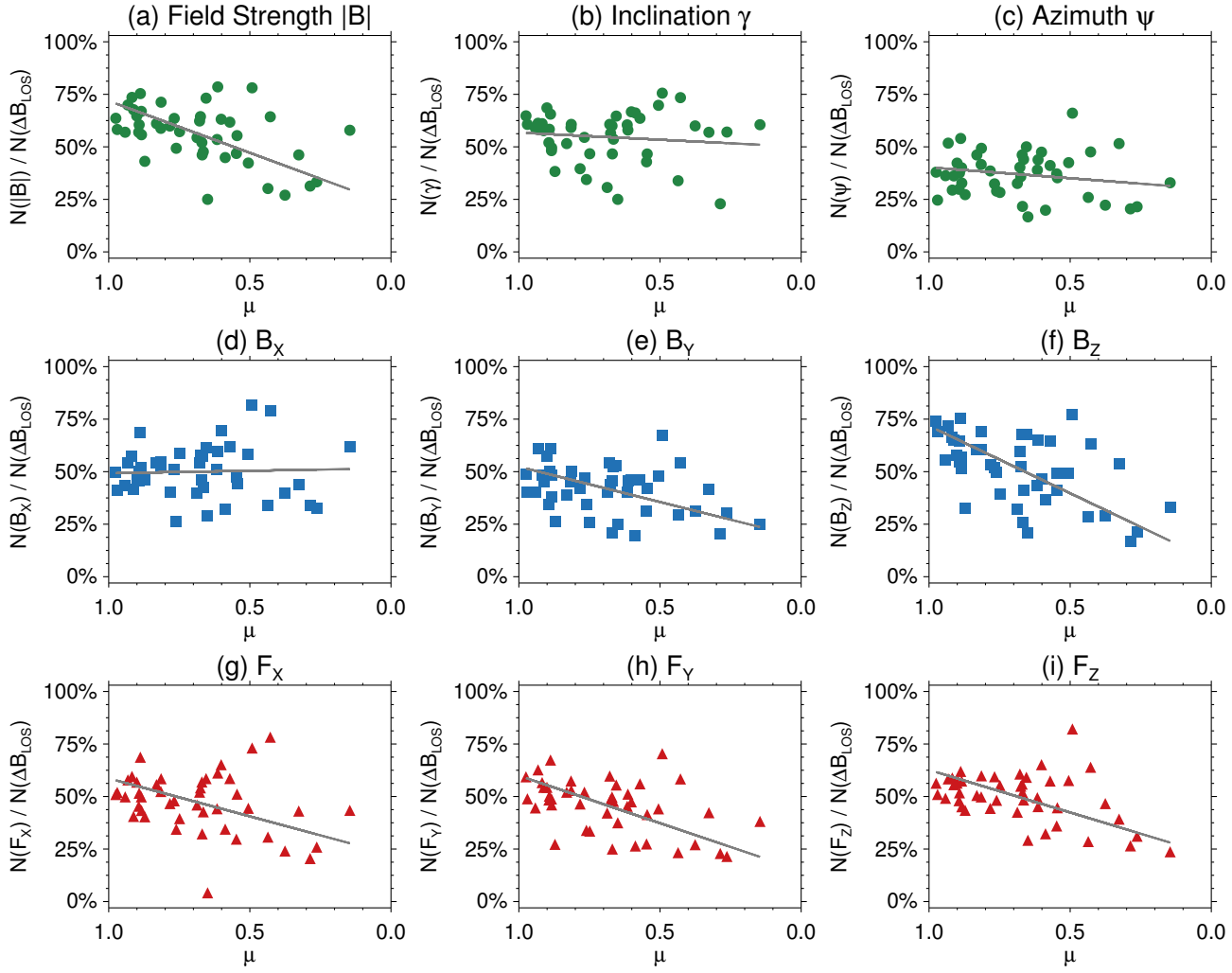


Figure 6.7: Heliocentric location of permanent vector changes associated with ΔB_{LOS} per flare. N represents the number of permanent changes observed in (a) field strength, (b) inclination, (c) azimuth, (d) B_x , (e) B_y , (f) B_z , (g) F_x , (h) F_y , (i) F_z . $N(\Delta B_{\text{LOS}})$ is the number of permanent changes in the LOS. The correlation of ΔB_{LOS} and permanent vector magnetic field changes decreases for limb flares.

& Sammis 1999, Petrie & Sudol 2010). Here we investigate the relation between ΔB_{LOS} and stepwise changes of the vector magnetic field. Figure 6.7 shows the heliocentric location of permanent vector changes associated with ΔB_{LOS} per flare. The locations of the flares are expressed regarding $\mu = \cos \theta$, where θ is the heliocentric angle of the flares. We found that flares with irreversible changes in azimuth and inclination do not depend on μ . The correlation of ΔB_{LOS} and changes in the field strength decreases for flares that were located near the limb. The B_x component for each flare does not have a center-to-limb dependence. The correlation of ΔB_{LOS} and B_y (towards poles) and B_z (radial) decreased for limb flares. The correlation between changes in the Lorentz force components and ΔB_{LOS} decreases near the limb. We investigated the correlation of the strength of the flare and the components of the vector magnetic field. Figure 6.8 shows the permanent vector changes associated with ΔB_{LOS} as a function of the GOES class for each flare. The colors show the center-to-limb location of the each flare. The correlation of all vector components with ΔB_{LOS} is larger for stronger flares. We did not find any correlation between ΔB_{LOS} and the vector changes in terms of the location of the flare. The outlier is the limb X6.9 flare (the strongest in the sample). In this event we observed that many of the vector profiles varied linearly.

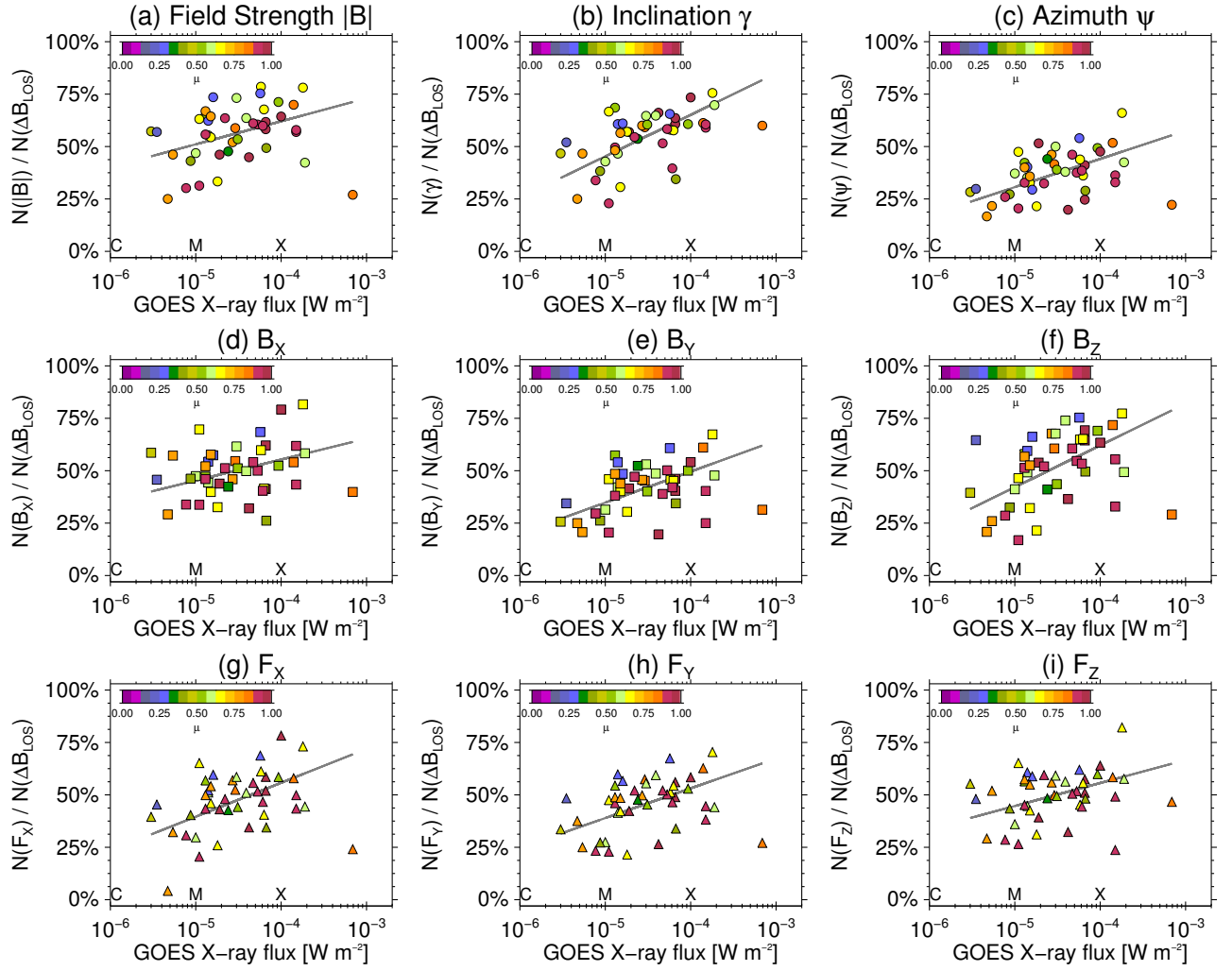


Figure 6.8: Permanent vector changes associated with ΔB_{LOS} as a function of the GOES class for each flare. N represents the number of permanent changes observed in (a) field strength, (b) inclination, (c) azimuth, (d) B_x , (e) B_y , (f) B_z , (g) F_x , (h) F_y , (i) F_z . $N(\Delta B_{\text{LOS}})$ is the number of permanent changes in the LOS. The colors show the center-to-limb location of the each flare. The correlation of ΔB_{LOS} and permanent vector magnetic field changes increases for larger flares.

Are there vector magnetic field changes without LOS changes? We analyzed an M6.6 class flare (2011-02-18T10:11), with coordinates 15.7°S , 52.5°W ($\mu = 0.57$). The magnetic field showed a complex geometry, and the ΔB_{LOS} kernel had a width of ~ 10 arcsec. We analyzed the permanent changes in the field strength, inclination, and azimuth inside a square region of 23×23 arcsec. This area contains the whole patch of changes plus regions that did not show ΔB_{LOS} larger than 80 Gauss (see right panels in figure 6.9). In total, the ΔB_{LOS} changes cover the 20% of the analyzed region. We investigated the permanent vector changes manually. We set lower limits to be able to comparable the ΔB_{LOS} and the permanent vector magnetic field changes. For γ and $|B|$ components, we did not count those pixels where permanent changes $\Delta\gamma$ (or $\Delta|B|$) were not large enough to produce changes of the LOS component calculated from the vector magnetic field data $\Delta B_{\text{LOS}}(\text{Vector}) \geq 80$ G. For ψ component, we counted the pixel if both permanent changes $\Delta\psi$ and $\Delta B_{\text{LOS}}(\text{Vector}) \geq 80$ G were observed. We found that 15%, 11%, and 12% showed permanent changes of $\Delta|B|$, $\Delta\gamma$, and $\Delta\psi$ (respectively) without ΔB_{LOS} . In the middle-right panel in figure 6.9, we show the location of ΔB_{LOS} (black pixels), $\Delta\gamma$ (blue pixels),

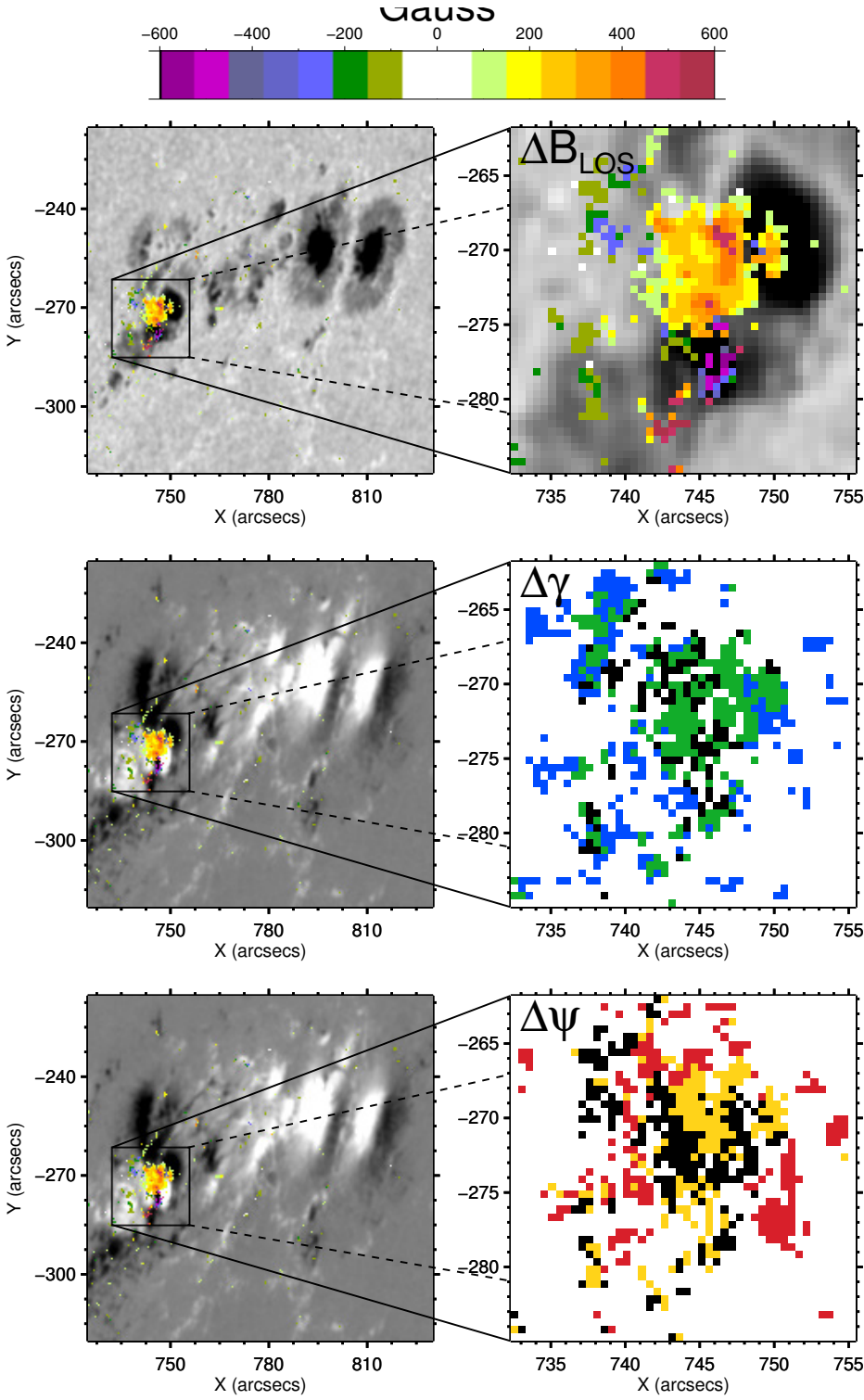


Figure 6.9: Permanent vector changes without ΔB_{LOS} . Left panels: Intensity (top) and magnetogram (middle and bottom) images of AR 11158 with ΔB_{LOS} . Right panels: Zoom of ΔB_{LOS} in a 23×23 arcsec box where we study the variations of the vector field. On the top-right, ΔB_{LOS} are denoted by their amplitude according to the color scale that ranges between ± 600 Gauss. On the middle-right, colored pixels indicate the location of ΔB_{LOS} (black), $\Delta\gamma$ (blue), and green pixels show positions where ΔB_{LOS} and $\Delta\gamma$ coincided. On the bottom-right, colored pixels indicate the location of ΔB_{LOS} (black), $\Delta\psi$ (red), and yellow pixels show positions where ΔB_{LOS} and $\Delta\psi$ coincided. This figure shows that there are $\Delta\gamma$ and $\Delta\psi$ without ΔB_{LOS} .

and green pixels show positions where ΔB_{LOS} **and** $\Delta\gamma$ coincided. On the bottom-right, colored pixels indicate the location of ΔB_{LOS} (black), $\Delta\psi$ (red), and yellow pixels show positions where ΔB_{LOS} **and** $\Delta\psi$ coincided. We found that there are permanent vector magnetic field changes without $\Delta B_{\text{LOS}} > 80$ G.

6.3 Vector Magnetic Field Changes along the PIL[®]

Previous studies of the photospheric vector data during solar flares pointed out the importance of the PIL, and the changes of the field around this region (e.g., Wang et al. 1994, Petrie 2012, Petrie 2013). Here we aim to study the permanent vector changes along the PIL of the sunspot where strong magnetic fields ($B_{\text{LOS}} > 100$ G) are measured. Note that the PIL[®] that separates strong magnetic fields greater than 100 G is just part of the whole PIL of the active region. With this definition, we are not taking into account the contribution of small magnetic fields. Hereafter, we are going to denote as PIL[®] just the part of this line that separates strong magnetic fields. We determined the PIL[®] of the full active region automatically for 72 flares (see below), and we studied the evolution of the magnetic field inside a region next to the PIL[®] of 4.95 arcsecs width. To find the PIL[®] for the 74 active regions, we applied the following steps on the magnetograms near the peak of the flare:

- i) Smooth the image using a boxcar of 3×3 pixels.
- ii) Mask all pixels with absolute values less than 30 Gauss ($|B_{\text{LOS}}| < 30$ G).
- iii) Find all points that surround the positive and negative polarities.
- iv) Trace a circle with a radius of 4.95 arcsecs for each point previously found on the iso-magnetic curve. If 25% of the pixels inside the circle have values greater than 100 Gauss for each polarity, then the point is considered part of the PIL[®]. In the other case, the point is not considered part of the PIL[®], and then it is rejected.

The 100 Gauss and 25% of the pixels limits described above were chosen after we tested cases of 72 sunspots. These conditions worked best to determine the PIL[®] for all the regions in our sample. The 4.95 arcsecs is the mean distance from the PIL[®] where ΔB_{LOS} are found (see §5.4 in chapter 5). The sunspots were located from the limb to the solar center without any restriction. Figure 6.10 shows the PIL[®] in green, and the areas around the location in of the PIL[®] in red with a width of 9.9 arcsecs of 3 sunspots that produced M5.2, M6.3, and X1.4 flares.

We studied the evolution of the vector magnetic field inside an area composed of circles with 4.95 arcsecs radius traced along the PIL[®]. We summed the total unsigned flux inside the area for the strength of the field, the vector components of \vec{B} (B_x , B_y , B_z), and the three components of the Lorentz force (F_x , F_y , F_z). For the inclination and azimuth angles, we took the average inside the areas because values greater than 180° and 360° , respectively, do not have a physical meaning in this context.

The evolution of the LOS components and vector data inside our selected area along the PIL[®] are shown in figures 6.11- 6.13. We show the temporal evolution for 3 flares: M2.2 (figure 6.11), M9.3 (figure 6.12), and X1.1 (figure 6.13). The images on the top show the location of the PIL[®] on the magnetogram (a), and the intensity image plus ΔB_{LOS} (b). The location of the temporal variations of the field follow the

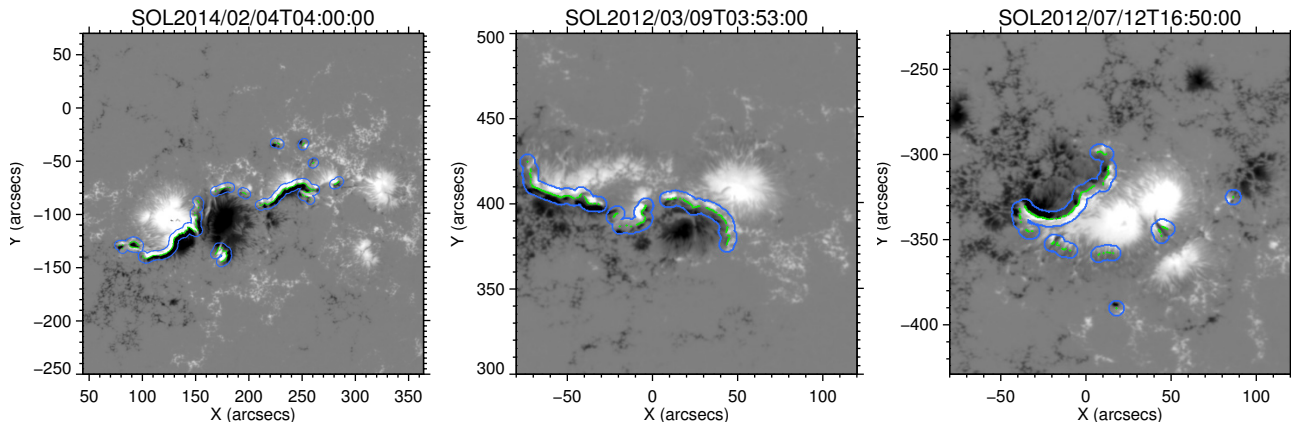


Figure 6.10: Location of the area along the PIL® in 3 active regions with flares M5.2 - SOL2014-02-04T04 (left), M6.3 - SOL2012-03-09T03:53 (middle), and X1.4 - SOL2012-07-12T16:50 (right). The background image shows the magnetogram closest in time to the peak of the flare. The PIL® of strong magnetic field is shown by the green pixels, and the area around the PIL® is denoted by the blue line. The area has 9.9 arcsecs width. Inside the area we study the evolution of vector magnetic fields.

color scale of the line in panel (b). Panels (c-n) show the temporal evolution of inclination (c), azimuth (d), and field strength (e). The magnetic field in coordinates (f) B_x , (g) B_y , and (h) B_z . The X, Y, Z components of the Lorentz force are shown in panels (i-k). The horizontal component of the magnetic field is in panel (i), and the light-curves of LOS-component ($\Delta B_{LOS}(45s)$) and intensity with a cadence of 45 seconds are shown in panels (m-n) respectively. We subtracted the average of each single profile to shift all light-curves around zero.

The average inclination along the PIL® during the X1.1 flare showed permanent negative changes of $\sim 4^\circ$ (blue profiles in figure 6.11). In the case of the M2.2 flare, the inclination increased linearly on the yellow regions (figure 6.13d). During the X1.1 and M2.2 flares the field strength inside the area around the PIL® increased permanently. We observed irreversible changes in inclination and field strength along the PIL® during these three events. The average azimuth of the field did not show any trend, while the strength, the horizontal and vertical components of the field, as well as the Lorentz components, showed abrupt and permanent changes co-spatial with ΔB_{LOS} . The WL emission showed an enhancement in the 3 events (panels n in figures 6.11, 6.12, 6.13).

The M9.3 event shows positive and negative permanent changes along the PIL® (figure 6.12). Green regions were related to the ΔB_{LOS} kernel (panel b). Panel c shows negative stepwise changes in inclination in green and positive in purple. Green light-curves of the field strength component showed positive changes, while the purple light-curves decreased after the flare (panel e). Both green and purple regions in the LOS component were associated with permanent positive changes (panel m).

Did all the 72 PIL®'s change permanently? 52 above 72 area around flaring PIL®'s showed permanent changes in at least one of the vector components. We observed ΔB_{LOS} and irreversible vector changes during 44 above 72 flares. The horizontal component changed in 38 above 72 flares, while the vertical component permanently changed during 29 above 72 flares. In 45 above 72 events, the horizontal **or** vertical components changed, but just in 22 events both horizontal **and** vertical components permanently changed. Changes in field strength and inclination were seen more often than changes in azimuth. Table 6.2 shows the number of flares that showed unsigned positive, negative, or both changes in \vec{B} . We found

a preference for positive changes in the field strength. During 20 flares the inclination of the magnetic field increased, and the variation in the horizontal field is larger than the radial, i.e., during 20 events we observed that the field tilted after the flare (see figure 6.11). However, the opposite scenario was also seen in 13 events. Those flares showed the radial field strength increasing more than the horizontal component (see figure 6.12).

	$\Delta \vec{B} $	$\Delta\gamma$	$\Delta\psi$	$\Delta B_X $	$\Delta B_Y $	$\Delta B_Z $	$\Delta B_h $	$\Delta F_X $	$\Delta F_Y $	$\Delta F_Z $
Positive	29	22	9	29	20	20	31	28	23	29
Negative	3	13	17	4	8	5	2	2	4	4
Pos. and Neg.	6	2	4	4	4	4	5	3	4	3

Table 6.2: Number of flares that show positive, negative or positive and negative permanent changes in the vector components around the PIL[®].

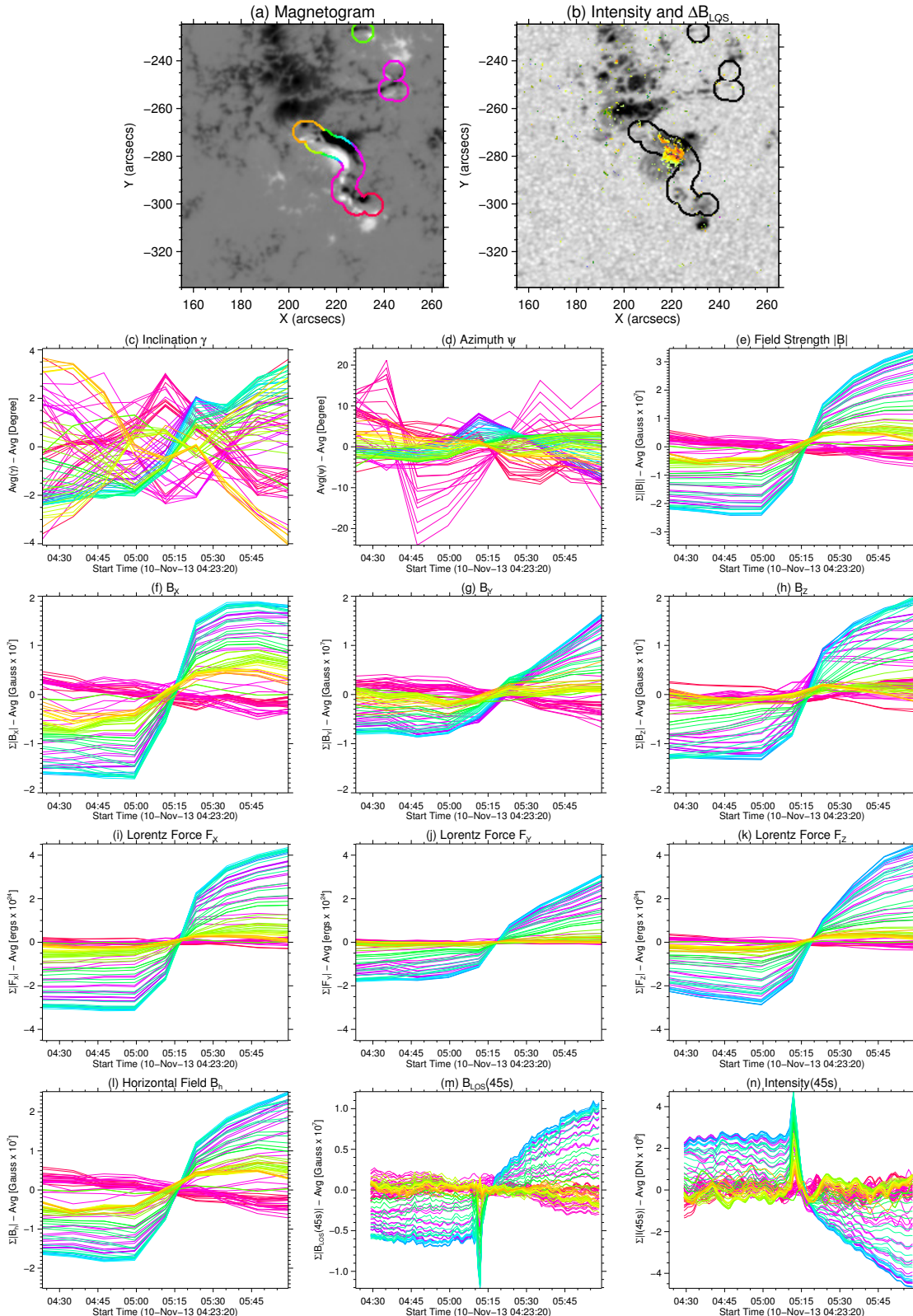


Figure 6.11: Temporal evolution of the vector components around the PIL[®] during an X1.1 flare (SOL2013-11-10T05:14). The top panels show an area around the location of the PIL[®] over the magnetogram (a), and the intensity image plus ΔB_{LOS} (b). The temporal variations of the field follow the colors drawn along the PIL[®] on panel (a). Panels (c-n) show: (c) inclination, (d) azimuth, (e) field strength. The magnetic field coordinates is shown in (f) B_x , (g) B_y , and (h) B_z . The X, Y, Z components of the Lorentz force are shown in panels (i-k). The horizontal component of the field is shown in panel (l), and $B_{\text{LOS}}(t)$ from magnetograms and intensity lightcurves with a cadence of 45 seconds are shown in panels (m-n) respectively. Permanent changes in the vector magnetic field components were observed during this event.

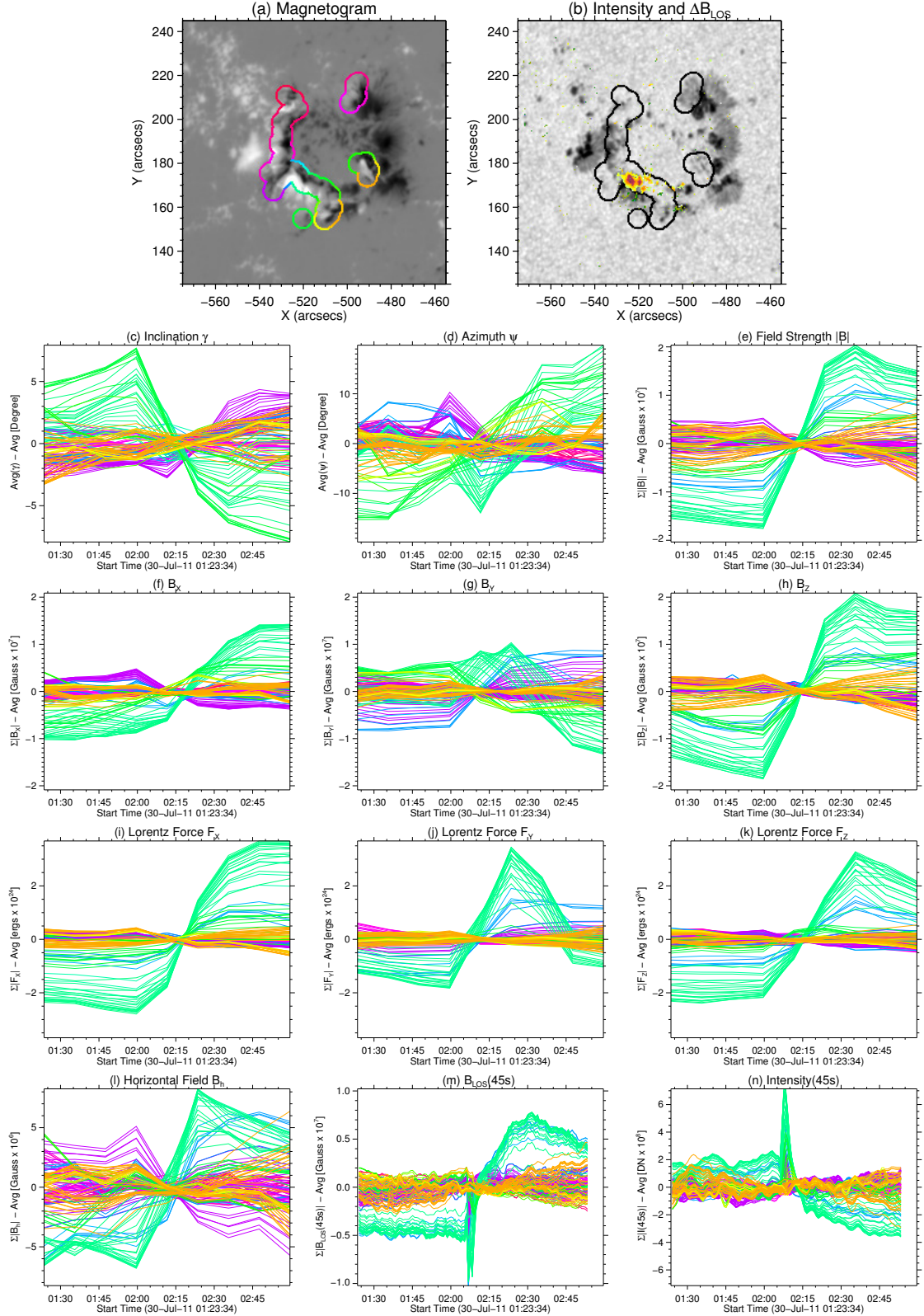


Figure 6.12: Temporal evolution of the vector components around the PIL[®] during an M9.3 flare (SOL2011-07-30T02:09). Panels similar to figure 6.11. Permanent changes in the vector magnetic field components were observed during this event.

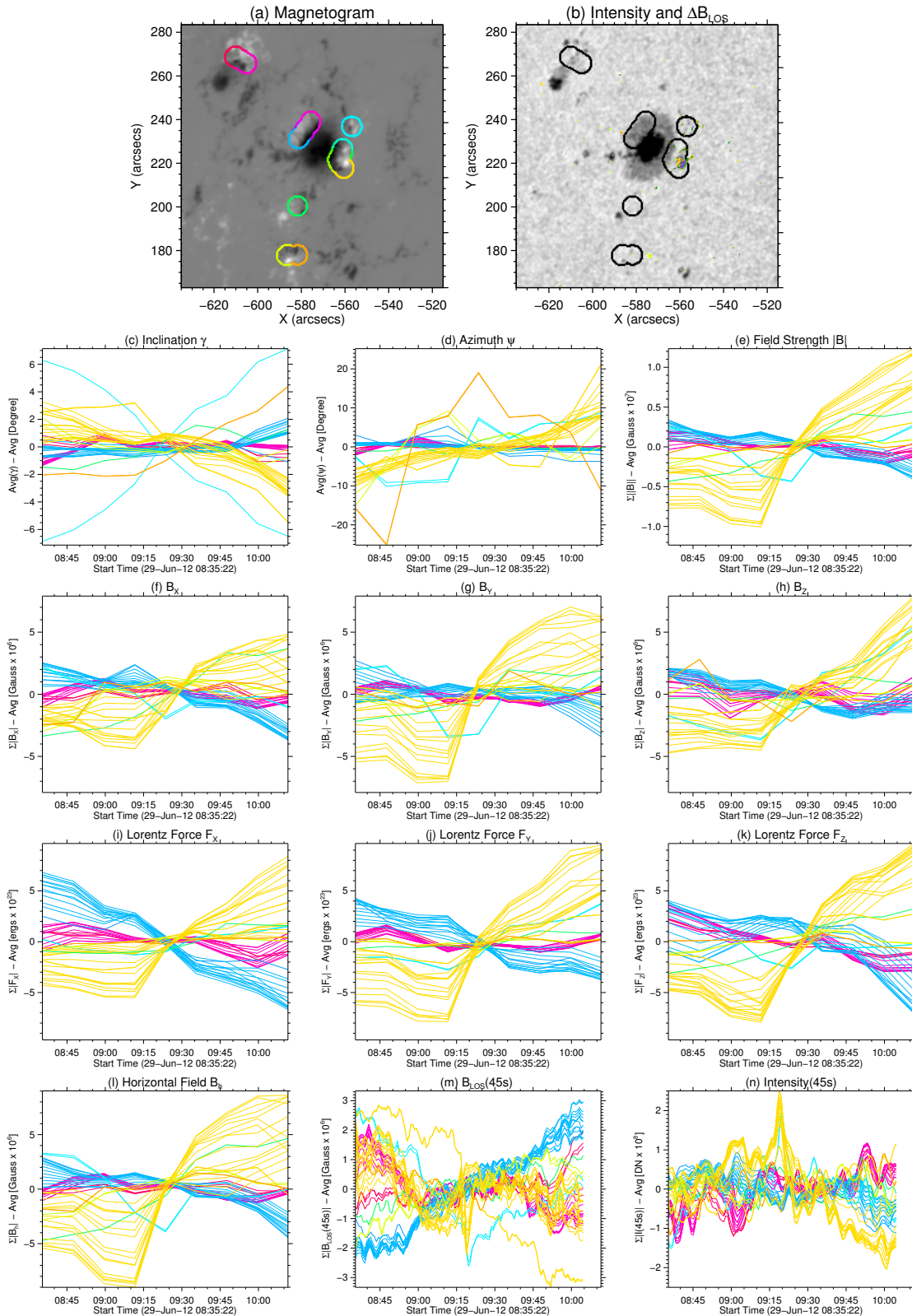


Figure 6.13: Temporal evolution of the vector components along the PIL[®] during an M2.2 flare (SOL2012-06-29T09:20). Panels similar to figure 6.11. Permanent changes in the vector magnetic field components were observed during this event.

Chapter 7

Summary, Conclusions and Outlook

Significant amount of energy is released when magnetic field lines reconnect in the corona during solar flares. Observations have found both transient and irreversible changes in the photospheric magnetic fields during flares, but their origins and mechanisms are yet unclear. To investigate the properties of permanent changes of the magnetic field during flares, e.g. their size, area, and timing, we performed the first statistical analysis of LOS and vector magnetic field changes during solar flares using data from SDO/HMI. We studied a total of 75 solar flares which had the following as their main characteristics: (1) a broad energy range from extreme to small flares (18 X-class, 37 M-class, 19 C-class and 1 B-class flares), and (2) a wide range of heliographic longitudes (from disk center to limb).

We summarize the main results of our study:

- We wrote a pipeline in IDL/IDLSSW to reduce and analyze the SDO/HMI data. The data we analyzed had a total size of ~ 2 TB. The pipeline requires the information of the flare as an input (location and times of the flare), and then, it downloads the data and organizes them, cuts and aligns the images, fits the stepwise function to all pixels in the FoV, determines the size of the stepwise changes, and co-aligns the 12-minutes vector data to the 45-seconds data. The pipeline can be applied to any flare observed by SDO. For a future work, for example, we might be able to study the permanent changes of the magnetic field during all flares of the 24th solar cycle observed by SDO.
- We found permanent changes ranging from 80 Gauss up to ~ 750 Gauss, in contrast with previous studies that found photospheric changes up to 450 Gauss (Petrie & Sudol 2010, Johnstone et al. 2012, Cliver et al. 2012, Burtseva et al. 2015, Kleint 2016). The rate of the magnetic field change in our study ranged between 0.2 and 307 G min^{-1} , with an average around 22.1 G min^{-1} . 91% of the changes ranged between 0.2 and 50 G min^{-1} , which is consistent with previous studies (Sudol & Harvey 2005).

- We introduced a morphological classification of all permanent changes with 12 classes. These classes were proposed because the stepwise SH-model (Sudol & Harvey 2005) does not describe all irreversible changes in this study well. Previous studies considered a profile to have changed permanently if the magnetic field jumps stepwise (e.g. Sudol & Harvey 2005, Burtseva et al. 2015). It is known that the flare changes local conditions of the magnetic field. For example, the flare process can trigger or inhibit flux emergence or cancellation, or change the topology of the magnetic field. In those cases, the temporal evolution of the magnetic field changes drastically from before and after the flare. Therefore, the first morphological classification of the permanent changes presented in this work attempts to describe the observational alternatives in the temporal evolution of the magnetic field. In addition, this classification will help to test models of ΔB_{LOS} of the magnetic field in lower atmosphere during flares. Models should contain the different types of permanent changes of the magnetic field.
- 18 X-class flares, 35 M-class events, and 6 C-class flares showed kernels of permanent changes in the LOS magnetic field larger than 80 Gauss, but no changes were found in 3 M-class and 11 C-class flares. The irreversible changes were located in compact kernels on or near the PIL. The areas of the kernels range from 4 - 586 Mm². The kernels of changes tend to be located in the penumbra, close to the PIL, and near the transition between umbra and penumbra. Changes were also observed in the umbra and quiet sun. During flares large structures of the magnetic field in the corona change, but our result showed that not all the magnetic structure in the photosphere changes.
- We define a positive change when the absolute value of the magnetic field jumps from a lower value of the field strength before the change to a higher one. A negative change occurs in the opposite case. 36 events showed more positive changes, while during 23 flares more negative irreversible changes were observed. All limb flares with heliocentric longitude greater than 74° showed more negative changes, and the total flux change of the negative polarity was also larger than the positive polarity. 12 flares with heliocentric longitude less than 30° showed a higher positive changes. We found for small flares that the amount of positive and negative changes of the unsigned magnetic flux tends to be equal, though this equilibrium was broken towards one of the polarities for larger flares. The total signed change ranged between $-67.3 \times 10^3 \text{ Mx cm}^{-2}$ to $247.3 \times 10^3 \text{ Mx cm}^{-2}$. These results are consistent with previous observations, which found both positive and negative changes (Cameron & Sammis 1999, Kosovichev & Zharkova 2001, Spirock et al. 2002, Wang et al. 2002b, Petrie & Sudol 2010, Cliver et al. 2012). In addition, we observed changes in the shape of the active regions in 25 events. During 15 flares, parts of the penumbra near the location of the flare disappeared, and during 8 flares new patches of the penumbra appeared. In 2 events, we observed movements of the PIL. These results are consistent with previous reports that found the three cases: parts of the sunspots appearing (Wang et al. 2002a), disappearing (Wang et al. 2002b), or the PIL moving (Kosovichev & Zharkova 2001).
- We observed a decreasing exponential relation for the number of irreversible changes (N) as a function of the unsigned step-size of the change ($|\Delta B_{\text{LOS}}|$). All flares in the sample that showed ΔB_{LOS} had the same behavior. In addition, we compared the same quantities from three independent studies (Sudol & Harvey 2005, Petrie & Sudol 2010, Burtseva et al. 2015). For these studies, the same exponential trend was observed. The observational relation for the entire sample of permanent changes is

$$N(|\Delta B_{\text{LOS}}|) = 10509 \exp\left(-\frac{|\Delta B_{\text{LOS}}|}{95.9}\right), \quad r^2 = 0.985. \quad (7.1)$$

The mean size of the change is equal to 95.9 G, which is comparable with a 80 Gauss mean change reported by Petrie & Sudol (2010). Petrie & Sudol (2010) suggested a power-law behaviour with a strong power index for the distribution of permanent changes in their sample. However, we found that the distribution of the ΔB_{LOS} is better described by a decreasing exponential law.

- In the present work, we observed that larger flares show more permanent changes in larger areas, and produced larger permanent changes. The energy emitted during each flare in the SXR band correlates with the total photospheric area where permanent changes are found, following a power-law:

$$A(F_{\text{SXR}}) = 10^{4.78} F_{\text{SXR}}^{0.67}, \quad r^2 = 0.601. \quad (7.2)$$

That the amplitude and number of permanent changes are larger for more energetic flares was suggested previously for strong flares or for individual events (e.g. Wang & Liu 2010 Burtseva & Petrie 2013.). In our study, we present a statistical correlation for 55 flares that showed ΔB_{LOS} ranging from C- to X- class.

- We found fewer irreversible changes for limb flares than near-center flares. The perturbed area did not show that flares near the limb tend to disturb more area than the events located near the solar center, even when taking into account de-projected areas. Therefore, there was no center-to-limb relation with the observed LOS-permanent changes in our analysis, and this result contradicts Petrie & Sudol (2010).
- Previous studies found strong variations of the magnetic shear near the PIL associated with permanent changes (e.g. Wang 1992, Wang et al. 1994). The magnetic shear is defined as the angle between the potential field and the magnetic field. Just non-potential fields can store energy, and the magnetic shear is related with the *potentiality* of the field. This scenario of a changing magnetic shear above the PIL may be connected to the distance of the irreversible changes measured from the PIL and the amplitude change. We found permanent changes on or near the PIL. 95% of the changes were found no farther than 15 arcsecs from the PIL. 95% of the ΔB_{LOS} greater than 300 G were no farther than 10 arcsecs from the PIL. A decreasing exponential relation with the number of the permanent changes found (N) was found with respect to the distance measured from the PIL (d). The observational relation is given by

$$N(d) = 5093 \exp\left(-\frac{d}{4.95}\right), \quad r^2 = 0.987. \quad (7.3)$$

In our sample, the average distance of the permanent changes to the PIL was 4.95 arcsecs. 4.95 arcsecs can be understood as the distance from the PIL at which the population of the ΔB_{LOS} is reduced to $1/e$.

- We observed an enhancement in WL emission in 55 (74%) of the events. 53 events showed both ΔB_{LOS} and WL emission. We observed a WL enhancement without ΔB_{LOS} during 2 C-class flares. The WL emission and the permanent changes do not have a one-to-one spatial relationship, but they are near each other and often overlap. WL emission have areas comparable to the kernels of permanent changes and are located in the middle or right next to the ΔB_{LOS} kernels.
- We measured lower limits of the total unsigned change of the Lorentz force regarding the LOS components. Single changes in ΔF_{LOS} ranged from 3.6×10^{14} dyne to 2.0×10^{20} dyne. The mean unsigned changes for X-, M- and C-class events were 5.7×10^{21} dyne, 2.0×10^{21} dyne, and 6.4×10^{20} dyne, respectively. Limb flares showed stronger permanent changes in the LOS component

of the Lorentz force. Observation of the Doppler velocities of the photosphere will allow us to estimate the work done by the Lorentz force due to a back reaction of the magnetic field after the field is tilted (Hudson et al. 2008, Fisher et al. 2012). This type of observations may be helpful to understand the origin of sunquakes. However, the study of these phenomena is out of the scope of this thesis.

- We studied the evolution of the three components of the magnetic field in the same places where permanent changes in the LOS component were found, as well as in regions of a few arcsecs width measured from the PIL[®]. We concluded that the flares that show irreversible changes in azimuth and inclination do not vary with the location of the flare, although the correlation of the field strength decreases for flares that were located near the limb. Permanent changes in the field strength and inclination were found more often than changes in azimuth difference of 19%. The magnetic field strength irreversibly increased near the PIL[®] in 29 flares. During 20 flares, we observed that the inclination of the magnetic field decreased, as well as the change in the horizontal field was larger than the radial the magnetic field. This means that the magnetic field becomes tilted after the 20 flares. This agrees with the implosion model (Hudson 2000) that predicts the field becoming more horizontal after the flare, and with previous observational studies (e.g. Wang & Liu 2010, Petrie & Sudol 2010, Wang et al. 2012, Gosain 2012, Petrie 2013, Liu et al. 2014). However, during other 13 flares, the radial field showed positive and larger changes than the horizontal field. This implies the another scenario, i.e., the flare-loop is untwisted after flare (Kleint 2016). Therefore, we may conclude that there are three types of flares. The first type is explained by the implosion model. The second type of flare the untwist after the flare. The third type are flares without permanent changes.

Our results expand statistically the results of previous studies using state-of-the-art observations from the SDO satellite. We derived significant trends in the areas, sizes, and distributions of irreversible changes of the magnetic field that are related to variations in the topology of the field. We showed that photospheric magnetic field changes behave coherently and appear in patches. These irreversible changes are related to the energy emitted by the flare, and the location of the PIL as well, thus evidencing the importance of the PIL and the area around it during flares.

7.1 Outlook

In the future, the origin of the permanent changes should be investigated by completing a combined analysis with other instruments such as RHESSI, AIA, and IRIS. Possible future studies are:

- Study the permanent changes of the magnetic field during all flares that occurred during the 24th solar cycle. This can be carried out as the pipeline can be applied to any flare observed by SDO.
- An analysis of the high energy data from RHESSI will help us to clarify if the permanent changes of the field are related to accelerated particles.
- Joint observations of vector magnetic fields with images at higher altitudes can be used to track the behavior of the magnetic lines from the photosphere to the corona.

- If the permanent changes are produced by thermal variations in the low atmosphere, AIA chromospheric images will give us information about the location of the flare and the relation with radiation processes. With the 304 Å channel observing the transition region or by using IRIS, we would be able to track filament structures. With the coronal channels, we will analyze the topologic structure of the magnetic field.
- One can use inversions of SDO spectropolarimetric data to retrieve vector data with the maximum cadence possible of about 135 seconds. It will give us better information about the evolution of photospheric field during flares.

These studies can shed light on the origins of flares by understanding the behavior of the photospheric vector magnetic field, and its correlation with the X-ray emission and the UV images of the upper layers of the solar atmosphere.

Bibliography

- Alvarado-Gómez, J. D., Buitrago-Casas, J. C., Martínez-Oliveros, J. C., et al. 2012, Sol. Phys., 280, p335
- Aschwanden, M. J. 2005, Physics of the Solar Corona. An Introduction with Problems and Solutions (2nd edition)
- Ayres, T., Uitenbroek, H., Cauzzi, G., et al. 2009, in ArXiv Astrophysics e-prints, Vol. 2010, astro2010: The Astronomy and Astrophysics Decadal Survey, p9
- Benz, A. O. 2008, Living Reviews in Solar Physics, 5
- Bobra, M., Sun, X., Hoeksema, J., et al. 2014, Sol. Phys., 289, p3549
- Borrero, J. M. & Ichimoto, K. 2011, Living Reviews in Solar Physics, 8
- Borrero, J. M., Tomczyk, S., Kubo, M., et al. 2011, Sol. Phys., 273, p267
- Burtseva, O., Martínez-Oliveros, J. C., Petrie, G. J. D., & Pevtsov, A. A. 2015, ApJ, 806, p173
- Burtseva, O. & Petrie, G. 2013, Sol. Phys., 283, p429
- Cameron, R. & Sammis, I. 1999, ApJL, 525, L61
- Carmichael, H. 1964, NASA Special Publication, 50, p451
- Carrington, R. C. 1859, MNRAS, 20, p13
- Castellanos-Durán, J. S. & Calvo-Mozo, B. 2015, FACIEN, 6
- Centeno, R., Schou, J., Hayashi, K., et al. 2014, Sol. Phys., 289, p3531
- Chen, P. F. 2011, Living Reviews in Solar Physics, 8
- Chen, W.-Z., Liu, C., Song, H., et al. 2007, Chinese J. Astron. Astrophys., 7, p733
- Cheung, M. C. M. & Isobe, H. 2014, Living Reviews in Solar Physics, 11

- Cliver, E. W., Petrie, G. J. D., & Ling, A. G. 2012, ApJ, 756, p144
- Couvidat, S., Rajaguru, S. P., Wachter, R., et al. 2012a, Sol. Phys., 278, p217
- Couvidat, S., Schou, J., Shine, R. A., et al. 2012b, Sol. Phys., 275, p285
- Couvidat, S. & the HMI team. 2011, Calculation of Observables from HMI Data, Tech. rep., W.W. Hansen Experimental Physics Laboratory, Stanford University
- de Pontieu, B., McIntosh, S., Hansteen, V. H., et al. 2007, PASJ, 59, p655
- De Pontieu, B., Rouppe van der Voort, L., McIntosh, S. W., et al. 2014, Science, 346
- Degl'Innocenti, L. 2006, Polarization in Spectral Lines, Astrophysics and Space Science Library (Springer Netherlands)
- del Toro Iniesta, J. C. 2003, Introduction to Spectropolarimetry (Cambridge University Press)
- Ding, M. D., Qiu, J., & Wang, H. 2002, ApJL, 576, L83
- Falconer, D. A. 1997, Sol. Phys., 176, p123
- Fisher, G. H., Bercik, D. J., Welsch, B. T., & Hudson, H. S. 2012, Sol. Phys., 277, p59
- Fletcher, L., Hannah, I. G., Hudson, H. S., & Metcalf, T. R. 2007, ApJ, 656, p1187
- Fletcher, L. & Hudson, H. S. 2008, ApJ, 675, p1645
- Gary, G. A. & Hagyard, M. J. 1990, Sol. Phys., 126, p21
- Giovanelli, R. G. 1939, ApJ, 89, p555
- Gosain, S. 2012, ApJ, 749, p85
- Greenwood, P. & Nikulin, M. 1996, A Guide to Chi-Squared Testing (Wiley)
- Hale, G. E. 1908, ApJ, 28, p315
- Hall, J. C. 2008, Living Reviews in Solar Physics, 5
- Hathaway, D. H. 2015, Living Reviews in Solar Physics, 12
- Hirayama, T. 1974, Sol. Phys., 34, p323
- Hodgson, R. 1859, MNRAS, 20, p15
- Hoeksema, J., Liu, Y., Hayashi, K., et al. 2014, Sol. Phys., 289, p3483
- Howard, R. 1963, ApJ, 138, p1312
- Howard, R. & Severny, A. 1963, ApJ, 137, p1242
- Hudson, H. S. 1972, Sol. Phys., 24, p414
- Hudson, H. S. 2000, ApJL, 531, L75

- Hudson, H. S. 2011, *Space Sci. Rev.*, 158, p5
- Hudson, H. S., Acton, L. W., Hirayama, T., & Uchida, Y. 1992, *PASJ*, 44, L77
- Hudson, H. S., Fisher, G. H., & Welsch, B. T. 2008, in *Astronomical Society of the Pacific Conference Series*, Vol. 383, Subsurface and Atmospheric Influences on Solar Activity, ed. R. Howe, R. W. Komm, K. S. Balasubramaniam, & G. J. D. Petrie, p221
- Jeffrey, N., Kontar, E., Emslie, G., & Bian, N. 2015, ArXiv e-prints
- Jess, D. B., Mathioudakis, M., Crockett, P. J., & Keenan, F. P. 2008, *ApJL*, 688, L119
- Johnstone, B. M., Petrie, G. J. D., & Sudol, J. J. 2012, *ApJ*, 760, p29
- Judge, P. G. & Carlsson, M. 2010, *The Astrophysical Journal*, 719, p469
- Kleint, L. 2006, Master's thesis, Eidgenössische Technische Hochschule Zürich. ETH
- Kleint, L. 2016, In press *ApJ*
- Kleint, L., Battaglia, M., Reardon, K., et al. 2015, *ApJ*, 806, p9
- Kleint, L., Heinzel, P., Judge, P., & Krucker, S. 2016, *ApJ*, 816, p88
- Kopp, R. A. & Pneuman, G. W. 1976, *Sol. Phys.*, 50, p85
- Kosovichev, A. G. & Zharkova, V. V. 1998, *Nature*, 393, p317
- Kosovichev, A. G. & Zharkova, V. V. 2001, *ApJL*, 550, L105
- Krucker, S., Hudson, H. S., Jeffrey, N. L. S., et al. 2011, *ApJ*, 739, p96
- Kuhar, M., Krucker, S., Martínez Oliveros, J. C., et al. 2016, *ApJ*, 816, p6
- Leka, K., Barnes, G., Crouch, A., et al. 2009, *Sol. Phys.*, 260, p83
- Lemen, J. R., Title, A. M., Akin, D. J., et al. 2012, *Sol. Phys.*, 275, p17
- Lin, R. P., Dennis, B. R., Hurford, G. J., et al. 2002, *Sol. Phys.*, 210, p3
- Linsky, J. L. & Avrett, E. H. 1970, *PASP*, 82, p169
- Liu, C., Deng, N., Lee, J., et al. 2014, *ApJ*, 795, p128
- Liu, C., Deng, N., Liu, Y., et al. 2005, *ApJ*, 622, p722
- Liu, Y., Norton, A. A., & Scherrer, P. H. 2007, *Sol. Phys.*, 241, p185
- Mann, G., Warmuth, A., & Aurass, H. 2009, *A&A*, 494, p669
- Mariska, J. T. 1992, *The Solar Transition Region* (Cambridge University Press)
- Markwardt, C. B. 2009, in *Astronomical Society of the Pacific Conference Series*, Vol. 411, *Astronomical Data Analysis Software and Systems XVIII*, ed. D. A. Bohlender, D. Durand, & P. Dowler, p251

- Matthews, S. A., van Driel-Gesztelyi, L., Hudson, H. S., & Nitta, N. V. 2003, *A&A*, 409, p1107
- McIntosh, S. W., de Pontieu, B., Carlsson, M., et al. 2011, *Nature*, 475, p477
- Metcalf, T. R. 1994, *Sol. Phys.*, 155, p235
- Metcalf, T. R., Alexander, D., Hudson, H. S., & Longcope, D. W. 2003, *ApJ*, 595, p483
- Meunier, N. & Kosovichev, A. 2003, *A&A*, 412, p541
- Parenti, S. 2014, *Living Reviews in Solar Physics*, 11
- Patterson, A. 1984, *ApJ*, 280, p884
- Patterson, A. & Zirin, H. 1981, *ApJL*, 243, L99
- Pesnell, W. D., Thompson, B. J., & Chamberlin, P. C. 2012, *Sol. Phys.*, 275, p3
- Petrie, G. J. D. 2012, *ApJ*, 759, p50
- Petrie, G. J. D. 2013, *Sol. Phys.*, 287, p415
- Petrie, G. J. D. & Sudol, J. J. 2010, *ApJ*, 724, p1218
- Poletto, G. 2015, *Living Reviews in Solar Physics*, 12
- Qiu, J. & Gary, D. E. 2003, *ApJ*, 599, p615
- Rieutord, M. & Rincon, F. 2010, *Living Reviews in Solar Physics*, 7
- Schou, J., Scherrer, P. H., Bush, R. I., et al. 2012, *Sol. Phys.*, 275, p229
- Schrijver, C. J. 2007, *ApJL*, 655, L117
- Solanki, S. K. 2003, *A&A Rev.*, 11, p153
- Solanki, S. K., Livingston, W., & Ayres, T. 1994, *Science*, 263, p64
- Spirock, T. J., Yurchyshyn, V. B., & Wang, H. 2002, *ApJ*, 572, p1072
- Stenflo, J. 1994, *Solar Magnetic Fields: Polarized Radiation Diagnostics, Astrophysics and Space Science Library* (Springer)
- Sturrock, P. A. 1966, *Nature*, 211, p695
- Sudol, J. J. & Harvey, J. W. 2005, *ApJ*, 635, p647
- Sun, X. 2013, ArXiv e-prints
- Sun, X., Hoeksema, J. T., Liu, Y., et al. 2012, *ApJ*, 748, p77
- Tanaka, K. 1978, *Sol. Phys.*, 58, p149
- Testa, P., De Pontieu, B., Allred, J., et al. 2014, *Science*, 346
- Tian, H., DeLuca, E. E., Cranmer, S. R., et al. 2014, *Science*, 346

- van Driel-Gesztelyi, L. & Green, L. M. 2015, Living Reviews in Solar Physics, 12
- Vernazza, J. E., Avrett, E. H., & Loeser, R. 1981, ApJS, 45, p635
- Wang, H. 1992, Sol. Phys., 140, p85
- Wang, H. 2006, ApJ, 649, p490
- Wang, H., Ewell, Jr., M. W., Zirin, H., & Ai, G. 1994, ApJ, 424, p436
- Wang, H., Ji, H., Schmahl, E. J., et al. 2002a, ApJL, 580, L177
- Wang, H. & Liu, C. 2010, ApJL, 716, L195
- Wang, H., Spirock, T. J., Qiu, J., et al. 2002b, ApJ, 576, p497
- Wang, J., Shi, Z., Wang, H., & Lue, Y. 1996, ApJ, 456, p861
- Wang, S., Liu, C., Liu, R., et al. 2012, ApJL, 745, L17
- Wang, Y. & Zhang, J. 2007, ApJ, 665, p1428
- Webb, D. F. & Howard, T. A. 2012, Living Reviews in Solar Physics, 9
- Woods, T. N., Eparvier, F. G., Hock, R., et al. 2012, Sol. Phys., 275, p115
- Yashiro, S., Gopalswamy, N., Akiyama, S., Michalek, G., & Howard, R. A. 2005, Journal of Geophysical Research (Space Physics), 110, p12
- Yurchyshyn, V., Wang, H., Abramenko, V., Spirock, T. J., & Krucker, S. 2004, ApJ, 605, p546
- Zirin, H. & Tanaka, K. 1981, ApJ, 250, p791